BRILLOUIN SCATTERING INDUCED TRANSPARENCY: COHERENT OPTOMECHANICAL INTERACTION LEADING TO SLOW LIGHT AND NON-RECIPROCAL LIGHT TRANSMISSION

BY

JUNHWAN KIM

DISSERTATION

Submitted in partial fulfillment of the requirements
for the degree of Doctor of Philosophy in Mechanical Engineering
in the Graduate College of the
University of Illinois at Urbana-Champaign, 2019

Urbana, Illinois

Doctoral Committee:

Associate Professor Gaurav Bahl, Chair and Director of Research
Associate Professor Kimani Toussaint
Associate Professor Sanjiv Sinha
Assistant Professor Peter Dragic
Assistant Professor Kejie Fang

ABSTRACT

An optical isolator is a device that allows only one-way light transmission. It is an essential optical component used for protection of laser sources found in many applications such as undersea optical communication networks, spectroscopy, fluorescence microscopy, and laser cutting. Today, all optical isolators that are commercially available are constructed from magneto-optic materials that non-reciprocally rotate the polarization of counter-propagating light. In free-space and fiber optics, Faraday isolators perform extremely well with the difference in forward and backward transmission (isolation contrast) exceeding 40 dB over a wide range of laser wavelengths. In integrated photonic circuits, however, Faraday isolators are difficult to implement due to the lack of an established fabrication process for permanent magnets on-chip, and due to material limitations such as high absorption coefficient and low magneto-optic coefficient.

In this thesis, I investigate a new optical isolation technique that does not rely on the magneto-optic effect and can be implemented using any dielectric material. The technique exploits a common light-sound coupling process called Brillouin scattering to enable one-way light transmission within a simple system composed of a waveguide and a whispering-gallery resonator (WGR). I demonstrate that it is possible to induce a mode split within optical resonances of the WGR through Brillouin coupling with a mechanical mode of the WGR acting as a coherent state. This process is called Brillouin scattering induced transparency (BSIT), and similar effects have previously been observed in both atomic vapors (using electronic coherent states) and optomechanical devices (using standing-wave mechanical resonances). Distinct from past efforts, the BSIT effect is sensitive to propagation direction due to momentum conservation requirements intrinsic to Brillouin scattering, and therefore permits unidirectional optical transparency while optical absorption occurs in the opposite direction. As a result, BSIT can be used

to produce an ideal optical isolator.

My theoretical analysis of the BSIT system shows that increasing Brillouin coupling leads to a wider transparency window. Using this, I am able to experimentally demonstrate that the light transmits through the system with nearly zero loss in the transparency direction. Such an optical isolator having extremely low forward insertion loss, and which can be implemented in any dielectric, is extremely attractive for integrated applications where magnetic fields are undesirable and the material availability is limited.

Lastly, I characterize the BSIT system as a slow light system, an effect that is associated with a rapidly changing optical phase response. I estimate the achievable time-delay and bandwidth of BSIT system and show that they are comparable to that of other slow light systems. Surprisingly, BSIT is shown to surpass other slow light systems in terms of size and power consumption by at least 5 orders of magnitude. Therefore, BSIT may also be used to efficiently generate optical delays in extremely compact photonic integrated circuits.

ACKNOWLEDGMENTS

First, I must thank my advisor professor Gaurav Bahl for his continuous support. He has given me countless opportunities both in and outside the lab to explore my fullest potential. I appreciate his guidance, ideas and time he spent throughout my graduate research. I am truly honored to be part of his research group.

I am thankful for my thesis committee members professor Kimani Toussaint, professor Sanjiv Sinha, professor Peter Dragic, and professor Kejie Fang for their helpful comments and suggestions. Professor Sanjiv Sinha was also my undergraduate academic advisor and undergraduate research advisor who allowed me to work in his research group and inspired me to continue my study at graduate school. Also, I would like to thank professor Hailin Wang from University of Oregon for his support and contribution to my research.

I also thank all members of Bahl research group Donggyu, Kitt, Jeeweon, Soonwook, Rhinithaa, Jianing, Jeff, Inbar, Yin-Chung, Seunghwi, Kewen, Shiyi and also many undergraduate research assistants who helped me out with experiments. I had fun memories with all of you.

Lastly, I am grateful to my family. My loving wife always cheered for me and pulled me through the tough times. My two sons, Ian and Ethan, are my joy and strength for they always give me smiles. My parents and in-laws always gave me support even when I am away from home. I would not be here today without all of your support and encouragement.

TABLE OF CONTENTS

CHAPTER 1

INTRODUCTION

1.1 Thesis outline

The laser emits light from the stimulated emission process which grants a narrow optical linewidth defined by the energy level transition. In various applications, such narrow linewidth is manipulated to improve the system performance compared to those using the broadband optical source. In optical communication networks, the data transfer rate is greatly improved without increasing the signal bandwidth by frequency division multiplexing aided by the narrow laser linewidth. In fluorescence microscopy, illuminating the dyed specimen with a narrow linewidth laser allows the observation of cells and molecules with increased spatial resolution because the light source and fluorescence are spectrally resolved. And in spectroscopy, a narrow linewidth laser can excite a specific energy transition allowing the identification of materials with different energy level structures. In all of these applications, the laser linewidth directly affects the system performance. Unfortunately, the laser is a sensitive optical instrument easily disturbed from reflections and feedback fed into the laser diode or cavity. Thus, we invest a lot of effort protecting and stabilizing the laser source to upkeep and sustain the narrow linewidth.

One way to protect the laser source is to minimize reflections. The idea of applying a thin film to reduce reflection dates back to 1817 when Joseph Fraunhofer first explored chemically treating glass surface and observed the difference in reflections [1]. Then in 1886, Lord Rayleigh proposed how index matching could reduce the reflection on glass surfaces [2]. Lord Rayleigh found that a glass with a thin film of tarnish transmits better than a glass surface that is free of any deposits. As oppose to the glass-air interface, an interface with intermediate layer made with index matched film (having a

refractive index lower than glass but larger than air, $n_{glass} \rangle n_{film} \rangle n_{air}$) transmits more light. Today, hundreds of intricate layers of thin films with refractive index matching or even a graded-index anti-reflective coatings are commonly used to achieve highly-transparent glass surfaces for eyeglasses, camera lenses, and optical components used in research. However, as the name "anti-reflective coating" suggests, this method only protects the laser source from reflections that occur on the glass surfaces.

In reality, surface reflection is only one of many causes for instabilities and disturbances to the laser source. Therefore, we must block all optical signals sent towards the laser source which includes reflection, scattering, misguided optical signal and even input from other light sources. For that reason, the Faraday effect based optical isolator technology has been studied since the development of masers and lasers. In 1953, the Faraday effect was used for the first time to build the nonreciprocal element, microwave gyrator [3]. The first demonstration of micrwave gyrator was an important accomplishment because the gyrator is a fundamental building block for constructing many other nonreciprocal elements including the isolator. Simply, a passive filter can be implemented in series with the gyrator (Fig. 1.1, 1.3) to create an isolator (Fig. 1.2). Shortly afterwards, a microwave isolator was demonstrated [4, 5] and many other nonreciprocal elements in optical domain were also developed in the early 1960s [6, 7, 8].

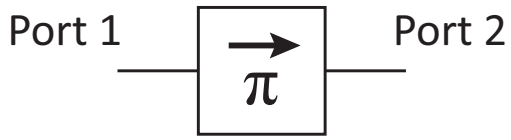

Figure 1.1: A gyrator is a two port nonreciprocal device that induces a π phase shift in the forward direction relative to the backward direction.

For understanding how such nonreciprocal devices behave, we use scattering matrix for convenience. With the sign conventions of Fig. 1.2, a gyrator (Fig. 1.1) inducing a directional phase shift is described using a scattering matrix as

$$\begin{pmatrix} b_1 \\ b_2 \end{pmatrix} = \begin{bmatrix} 0 & 1 \\ -1 & 0 \end{bmatrix} \begin{pmatrix} a_1 \\ a_2 \end{pmatrix} \tag{1.1}$$

In the matrix equation above, a is an input to the device, b is an output from

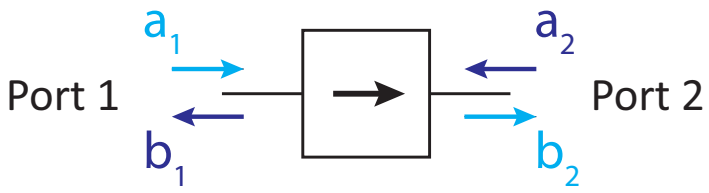

Figure 1.2: An isolator is another two port nonreciprocal device that transmits light one way while blocking transmission the other way.

the device, subscript 1 is for port 1 and subscript 2 is for port 2. In essence, a signal entering port 1 will exit from port 2 with no phase shift while another signal entering (such as reflection or scattering) port 2 will exit from port 1 with π phase shift. Similarly, an isolator (Fig. 1.2) which only allows a unidirectional transmission will have the following scattering matrix

$$\begin{pmatrix} b_1 \\ b_2 \end{pmatrix} = \begin{bmatrix} 0 & 0 \\ 1 & 0 \end{bmatrix} \begin{pmatrix} a_1 \\ a_2 \end{pmatrix} \tag{1.2}$$

This scattering matrix also represents an ideal isolator device response which behaves in the following way. First, all of port 1 input must exit at port 2 (zero insertion loss). Second, all of port 2 input must be absorbed (complete isolation). And last, no reflection should occur at the device although it should naturally follow when zero insertion loss and complete isolation is achieved due to conservation of energy. Placing such optical isolator in front of a laser source would allow all of laser power to be utilized while protecting the source from disturbances.

Today, an optical isolator is constructed using the Faraday effect exclusively in commercial applications. An optical isolator is composed of a magneto-optic material which rotates the polarization non-reciprocally (Fig. 1.3) and a birefringent film acting as a filter for the back-propagating optical signal. A bulk optical isolator[1] without space and magnetic field constraints works extremely well outperforming all other experimental approaches. However, we must examine how the Faraday optical isolator operates to examine its feasibility in other applications.

The Faraday effect is governed by the equation $\theta = VBL$ where θ is the

[1]It is referring to optical isolator that uses a bulk magneto-optic material prepared using crystal growth process.

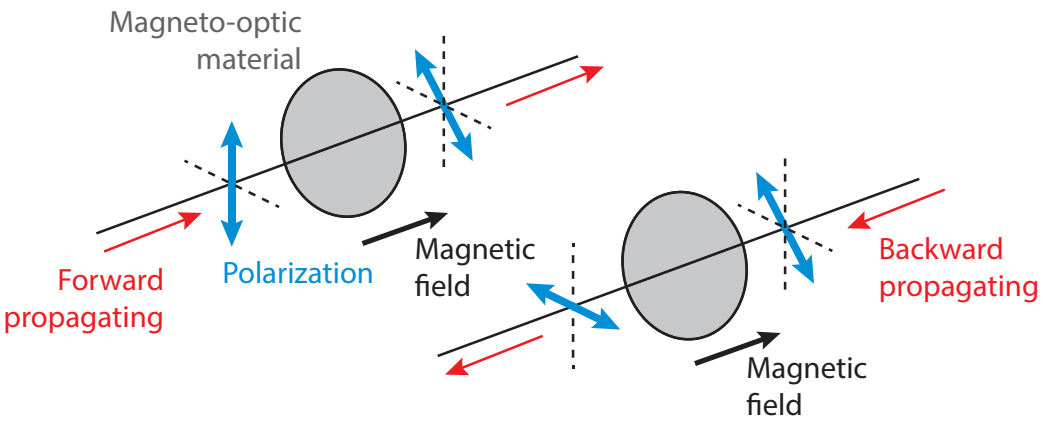

Figure 1.3: Faraday rotation using magneto-optic material. Light passing through the magneto-optic material experiences a non-reciprocal change in polarization angle because the magnetic field applying the bias is a vector quantity. Subsequently, birefringent filter is used to allow or prevent light transmission based on polarization (not shown here).

polarization rotation angle, V is the Verdet (magneto-optic) constant, B is the magnetic field, and L is the device length. Ideally, $\pi/4$ radian polarization rotation is required to completely isolate reflections. Many optical materials, however, do not have a significant Verdet constant. Therefore, Faraday isolator requires a large magnetic field or a long device length even when constructed with rare-earth iron garnets that does have practical Verdet constants. This makes the chip-scale implementation of Faraday isolator difficult where the device size is one of the most important engineering metric.

Furthermore, Faraday isolator is not suitable in applications requiring magnetic-field-sensitive components such as atomic vapor-based sensors. One example is a Rb atomic clock. An atomic clock outputs pulses at a defined frequency which can then be used to measure time. Needless to say, the stability of atomic clock oscillator is the key performance metric defining the long-term accuracy of time measurements. Although the atomic clock requires an optical isolator, the Faraday-effect based optical isolators are not suitable because the magnetic field necessary for the Faraday rotation disrupts the hyperfine transition through Zeeman shift. This leads to the splitting of Rb hyperfine energy level transition and degrades the accuracy of atomic clocks.

Many alternative optical isolation methods that does not rely on mag-

netic field bias have been proposed and demonstrated to avoid such problems [9, 10, 11, 12, 13, 14, 15], but Faraday optical isolators still outperform in terms of bandwidth, insertion loss and isolation contrast [6,16,17,18]. Therefore, my graduate study was dedicated to exploring a different approach that can compete against Faraday optical isolator without using magnetic fields and is compatible with chip-scale process ideal for integration to system-on-chip applications. The proposed optical isolator design relies on Brillouin scattering optomechanical interaction to realize non-reciprocal light transmission. As Brillouin scattering is a process found in all optical materials, it can be implemented in any existing optical devices including integrated photonic circuits.

In this thesis, two coupled optical modes required for Brillouin scattering in a cavity is used to draw an analogy to electron energy level transitions of an atom and to demonstrate induced transparency. Electromagnetically induced transparency (EIT) [19, 20] arises from destructive interference of electronic energy transitions induced by a long-lived non-radiative coherence of atomic states. This destructive interference suppresses and prevents the optical excitation of the medium [21]. Similarly, Brillouin scattering induced transparency (BSIT) emerges from destructive interference of light scattering pathways induced by a long-lived acoustic phonon mode of the resonator.

It is shown both theoretically and experimentally that the induced transparency having the acoustic mode linewidth appears with an optomechanical coupling. As the coupling rate is increased, the induced transparency becomes more apparent with broader and larger transparency window. Interestingly, when the coupling rate exceeds the optical loss rate, the size of the transparency window can no longer increase as the transmission is already completely inhibited i.e. lossless transmission. However, the theoretical analysis predicts that the transparency width will continue to widen with the increasing optomechanical coupling rate.

At this point, the counter-propagating degenerate optical mode is still unperturbed without the excitation of the acoustic mode in the backward direction. Comparing the forward and backward transmissions, the difference in absorption spectra reveals the BSIT system's isolation contrast. The extremely small loss in the forward transmission translates to nearly zero insertion loss. Thus, the isolation contrast per insertion loss of BSIT optical

isolator rivals with the performance of commercial Faraday optical isolators. For this reason, BSIT system strongly appeals to optical devices fabricated on-chip and applications where a stray magnetic field is undesirable such as an atomic clock.

1.2 Chapter overview

Chapter 2 provides the basic understanding of reciprocity theorem for electromagnetic waves and how we can design a device to circumvent this restriction. We will review both traditional approach using the Faraday effect and more recent development of reciprocity breaking methods.

Chapter 3 provides the necessary background on optical and acoustic whispering gallery modes. We show how optical and mechanical modes are categorized and characterized. The optical quality factor and its measurement technique is discussed as we utilize the resonantly enhanced optical and acoustic modes to allow observation of optomechanical effects with low optical power. Also, we introduce waveguide-resonator coupling techniques and explain the fabrication process for optical couplers and resonators including but not limited to tapered optical fiber coupler and microsphere resonators that we use for the experimental results appearing in this thesis.

Chapter 4 reviews fundamental background information for understanding Brillouin scattering with emphasis on the necessary conditions such as energy and momentum conservation requirement and acousto-optic interaction.

Chapter 5 presents the first experimental demonstration of Brillouin scattering induced transparency [22]. A complete analytical description as well as experimental methods and experimental result are presented here.

Chapter 6 describes how slow and fast light can be achieved using Brillouin scattering induced transparency [22]. The amplitude and phase response of Brillouin scattering induced transparency can be used to directly estimate slow and fast light time. We also show that Brillouin scattering induced transparency system outperforms all previous state-of-the-art slow and fast light systems in terms of an engineering metric, delay-bandwidth per size and power consumption.

Chapter 7 presents Faraday optical isolator theory and an alternative approach to achieve optical isolation without relying on magneto-optic ef-

fects [23]. Brillouin scattering induced transparency based optical isolator is built and tested for comparison against previous magnet-free optical isolators' performances.

Chapter 8 describes methods for demonstrating Brillouin scattering induced transparency and implementing optical isolator on-chip. This chapter discusses both material and design considerations for chip-scale processes. Also, a method for actuating acoustic wave on active optical devices using piezo-electric interdigital transducer is presented. We are yet to show Brillouin scattering induced transparency on-chip, but promising preliminary data showing optical and mechanical modes on chip are presented.

CHAPTER 2

NONRECIPROCITY AND TIME-REVERSAL SYMMETRY BREAKING

2.1 Introduction

The idea of reciprocity came about when George Green wrote an essay on the reciprocity relation of static electric charges in 1828 [24]. However, the importance of Green's findings was overlooked until people realized the existence of equivalent reciprocity theorems across all branches of physics. Helmholtz came up with a theorem for light using ray optics and point source treatment in 1859 [25]. And the reciprocity theorem in mechanical systems came about in the 1860s and 1870s [26, 27] although the most noted example is Rayleigh's reciprocity theorem appeared in the famous publication "The Theory of Sound" from 1894 [28]. Finally, the Lorentz reciprocity theorem was published with mathematical proof relating electric and magnetic fields of the system in 1896 [29] followed by the antenna theory examples [30, 31]. With the groundwork established for the reciprocities found in many different physical systems, the study of nonreciprocity showing the opposite phenomenon started to take off. The first discovery of nonreciprocity was of polarization rotation of electromagnetic wave as it passes through lead borate glass under magnetic field by Faraday in 1845 [32]. This discovery lead directly to the development of optical isolator and circulator with the aid of birefringent filters utilizing the phase difference in transmission and reflection (Fig. 1.3).

In this thesis, we will focus on the Lorentz reciprocity theorem that dictates the relationship between electromagnetic transmitter and receiver and their interchangeability. Specifically, the theorem states that the measured electric field at one location (where the detector is placed) created by a source certain distance away is unchanged even if the detector and source locations were interchanged (See Appendix A) [29]. Although the theorem itself is helpful

in calculating the radiation pattern of antenna and receiver, the physics is adding a contraint to the electromagnetic system design. Thus, we seek for ways to achieve nonreciprocity in the naturally reciprocal systems.

2.2 Methods of breaking time-reversal symmetry

2.2.1 Nonlinear system

Before discussing the methods of breaking time-reversal symmetry, we shall briefly mention that there exist systems that are inherently nonreciprocal. These systems typically utilize material nonlinearity along with a geometric asymmetry to demonstrate the nonreciprocal response [33, 34, 35, 36, 37]. Such system creates a relatively weak nonreciprocity with small difference in forward and backward transmission ratios. Furthermore, nonlinear systems have more constraints requiring careful consideration in designing the structure. Failure to provide the necessary conditions such as operating at out-of-resonance frequency can create a reciprocal wave propagation even in nonlinear asymmetric structures [38, 39]. As the nonlinearity of the system is inherent, the nonreciprocity is not reconfigurable. The potential benefit of nonlinear systems, however, is that they are passive devices and may offer long term stability.

2.2.2 Linear system

The most pronounced method for breaking the time-reversal symmetry is using an external bias in a linear time-invariant system. The Faraday effect falls under this category as well as the external magnetic field provides the bias necessary for breaking the time-reversal symmetry. There are countless examples of nonreciprocal systems that uses external bias to generate a very strong nonreciprocity [9, 10, 11, 13, 14, 15, 40] including the nonreciprocal optical transmission and optical isolation technique utilizing the traveling acoustic wave which will be discussed later in this thesis [22, 23].

To give an example of a nonreciprocal system using an external bias other than the magnetic field, Fig. 2.1 shows a linear time-invariant system using an angular momentum biasing [41]. In the axisymmetric circular system with

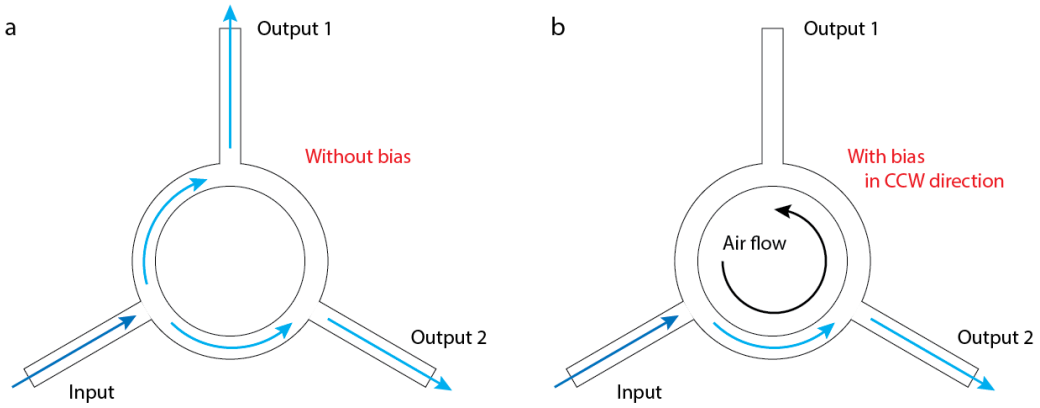

Figure 2.1: **a.** An acoustic circulator with axisymmetric structure. The acoustic wave entering from input port exits at both output 1 and output 2 ports with equal magnitude when the bias is not provided. **b.** However, when the external bias (air flow) is applied in the CCW direction, the acoustic wave exits at output 2 with isolation contrast of up to 40 dB. The system is reconfigurable as the air flow can be controlled.

three ports, an acoustic wave is put in from one of the port (Fig. 2.1). Without a bias, the acoustic wave will split and exit at the two ports equally given a symmetric geometry (Fig. 2.1a). However, the bias is applied with air fans generating an air-flow in a single direction to force the acoustic wave to give an additional angular momentum in the direction of the air flow (Fig. 2.1b). Considering the two output ports as a mode that acoustic wave can take, the bias creates a lifting of degeneracy for the two modes. Depending on the speed of fans, the degree of acoustic circulation and extinction ratio can be adjusted and further, the directionality of can be switched and reconfigured unlike the nonlinearity based nonreciprocal systems. At optimal operating speed, this device achieves 40 dB isolation ratio. And again, this type of system is not bound by many restrictions of nonlinear systems [39].

2.2.3 A note on linear asymmetric system

Before concluding this section, we shall clarify that linear passive devices cannot be used for breaking the nonreciprocity although many asymmetric structure is misunderstood as a diode [42]. A wave or a signal propagating from left to right, perpendicular to the wall of proposed asymmetric acoustic diode structure (Fig. 2.2a) will see a flat side and be reflected. On the other

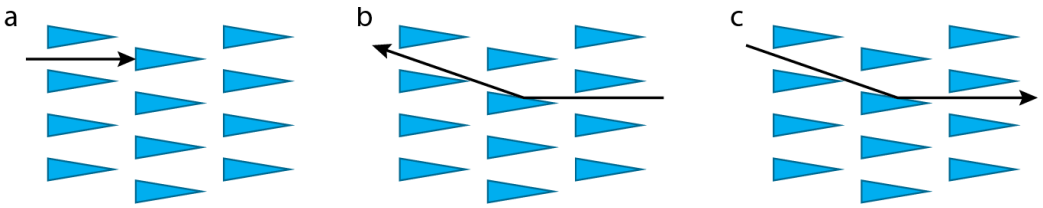

Figure 2.2: An example of asymmetric reciprocal system. **a.** The wave transmission is blocked. **b.** The wave transmits in the reverse direction. **c.** This structure, however, is reciprocal in a traditional sense as the time-reversal symmetry is not broken. Tracing back the wave trajectory from b, the sound wave can transmit from left to right.

hand, a wave propagating from right to left will deflect or scatter off at an angle defined by the geometry but seemingly transmit through (Fig. 2.2b). However, such passive asymmetric structure constructed of linear medium does not break the reciprocity theorem as the wave propagating from left to right at an angle will transmit reciprocally (Fig. 2.2c). There are several other examples of passive asymmetric structures that are misunderstood as nonreciprocal [42], but the reciprocity can usually be identified by tracing the wave propagation back to the origin.

2.3 Faraday-effect based nonreciprocity

In this section, we will review the Faraday effect and how nonreciprocity arises with the magnetic field bias. As discussed earlier, the Faraday effect rotates polarization of light passing through the magneto-optic material when the magnetic field bias is applied (Fig. 1.3). To understand this phenomenon, let's start from Maxwell's equations.

$$\nabla \times \mathbf{E} = -\mu_o \frac{\partial \mathbf{H}}{\partial t} \tag{2.1}$$

$$\nabla \times \mathbf{H} = \epsilon \frac{\partial \mathbf{E}}{\partial t} \tag{2.2}$$

For our convenience, let's assume we have a plane wave propagating in the z-direction expressed as

$$\mathbf{E} = \mathbf{E}_o \exp^{j(\omega t - \mathbf{kr})} \qquad \mathbf{H} = \mathbf{H}_o \exp^{j(\omega t - \mathbf{kr})} \tag{2.3}$$

And Maxwell's equations reduces to

$$\mathbf{k} \times \mathbf{E} = \mu_o \omega \mathbf{H} \tag{2.4}$$

$$\mathbf{k} \times \mathbf{H} = -\epsilon \omega \mathbf{E} \tag{2.5}$$

From the Drude model of magnetized plasma, the external magnetic field bias modifies the permittivity tensor as [43]

$$\epsilon_r = \begin{pmatrix} \epsilon_1 & -j\epsilon_g & 0 \\ j\epsilon_g & \epsilon_1 & 0 \\ 0 & 0 & \epsilon_2 \end{pmatrix} \tag{2.6}$$

Combining Eqs. 2.4, 2.5 and expressing in the tensor form

$$\begin{pmatrix} 0 & -k_z & 0 \\ k_z & 0 & -k_x \\ 0 & k_x & 0 \end{pmatrix}^2 \begin{pmatrix} E_x \\ E_y \\ E_z \end{pmatrix} = \frac{\omega^2}{c^2} \begin{pmatrix} \epsilon_1 & j\epsilon_g & 0 \\ -j\epsilon_g & \epsilon_1 & 0 \\ 0 & 0 & \epsilon_2 \end{pmatrix} \begin{pmatrix} E_x \\ E_y \\ E_z \end{pmatrix} \tag{2.7}$$

For the purpose of studying nonreciprocity, we consider the case where the magnetic field is perfectly aligned with the propagation direction of the electromagnetic wave ($k = k_z$ or $k_x = 0$).

$$\begin{pmatrix} -k_z^2 + \frac{\omega^2}{c^2}\epsilon_1 & j\frac{\omega^2}{c^2}\epsilon_g & 0 \\ -j\frac{\omega^2}{c^2}\epsilon_g & -k_z^2 + \frac{\omega^2}{c^2}\epsilon_1 & 0 \\ 0 & 0 & \frac{\omega^2}{c^2}\epsilon_2 \end{pmatrix} \begin{pmatrix} E_x \\ E_y \\ E_z \end{pmatrix} = 0 \tag{2.8}$$

Finding determinants of the given matrix and solving for the propagation vector

$$k^4 - 2k^2 \frac{\omega^2}{c^2}\epsilon_1 + \left(\frac{\omega^4}{c^4}\epsilon_1^2 - \frac{\omega^4}{c^4}\epsilon_g^2 \right) = 0 \tag{2.9}$$

$$k^2 = \frac{\omega^2}{c^2} \left(\epsilon_1 \pm \epsilon_g \right) \tag{2.10}$$

Reorganizing the terms, we can expressed the phase velocity as

$$v_p = \frac{1}{\sqrt{\mu \epsilon_o \left(\epsilon_1 \pm \epsilon_g \right)}} \tag{2.11}$$

Thus, the electromagnetic wave propagating through the magneto-optic material will experience a phase shift that depends on the magnitude of the applied magnetic field bias, the length of magneto-optic material and the Verdet constant[1]. The two values of phase velocity obtained due to $\pm\epsilon_g$ corresponds to left-hand circularly polarized ($+\epsilon_g$) and right-hand circularly polarized ($-\epsilon_g$) light.

Now, let's revisit Fig. 1.3 and assume that the forward propagating light is right-hand circularly polarized (RCP). According to Eq. 2.11, RCP light will experience a slight delay in phase ϕ. When a time-reversal operation $T : t \mapsto t' = -t$ takes place or when the light reflects from a mirror, the backward propagating light becomes left-hand circularly polarized (LCP). As the magnetic field is now pointing opposite of the backward propagating direction, it will experience an additional delay in phase ϕ. Thus, the reflected light measured at the source will have a phase delay of 2ϕ. In other words, we observe the nonreciprocal phase shift and the time-reversal symmetry is broken when the magnetic field parallel to the light propagation direction is applied across the magneto-optic material.

2.4 Challenges with Farday effect based devices

2.4.1 Verdet constants of magneto-optic materials

As mentioned in the Introduction, the Faraday effect based nonreciprocal devices such as optical isolator and circulator operate extremely well, but they are not without shortcomings. Bulk optical isolators are constructed from ferrites such as ytterbium iron garnet (YIG) or terbium gallium garnet (TGG) having a relatively large Verdet constants. For example, TGG has a Verdet constant of 300 to 40 rad/Tm from visible to near infrared at room temperature 2.3. An optical isolator using TGG as magneto-optic material would require mm to cm device length when a rare-earth magnet of a practical size is used to provide the requisite magnetic field bias (approximately a few mT). More specifically, the Faraday optical isolator made from TGG operating at 532 nm wavelength requires 10 cm device length when 2.5 mT

[1]Verdet constant, or magneto-optic constant, is a material property that determines the gyrotropic constant ϵ_g from the permittivity matrix.

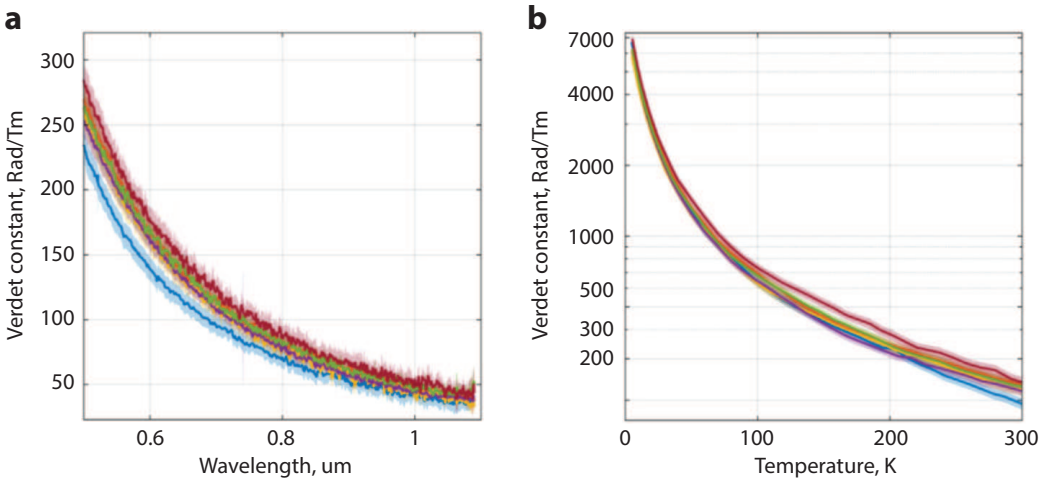

Figure 2.3: Verdet constant of terbium gallium garnet. Figures show data from 6 different samples. **a.** Wavelength dependence. **b.** Temperature dependence. Figures are from [44].

magnetic field bias is provided. Such device size is not a problem for bulk optical isolators, but is not feasible anymore for miniaturization and integration on-chip.

2.4.2 Growth and deposition of magneto-optic material on-chip

In addition to the device size, another problem originating from the magneto-optic materials is its crystal structure and compatibility with microfabrication process. Bulk optical isolators are constructed from aforementioned magneto-optic materials commonly grown using Czochralski process to obtain highly crystalline material without defects [2]. The deposition or growth of magneto-optic material directly on silicon or silicon dioxide substrates have been attempted [47]. However, such deposition processes involving simultaneous evaporation of many elements are complex and often require a special chambers and instruments. Even then, the acquired magneto-optic materials' performances typically fall short from the bulk material prepared using the crystal growth because of a large crystal lattice mismatch and thermal expansion coefficient mistmatch between silicon (5.4307 Å, 2.6×10^{-6} K^{-1}) and TGG (12.355 Å, 7.6×10^{-6} K^{-1}) or YIG (12.376 Å, 10.4×10^{-6} K^{-1}). Others

[2]Despite the high cost of growing crystalline material, magneto-optic materials prepared by polishing a single crystal are known to have better magneto-optic coefficients [45, 46]

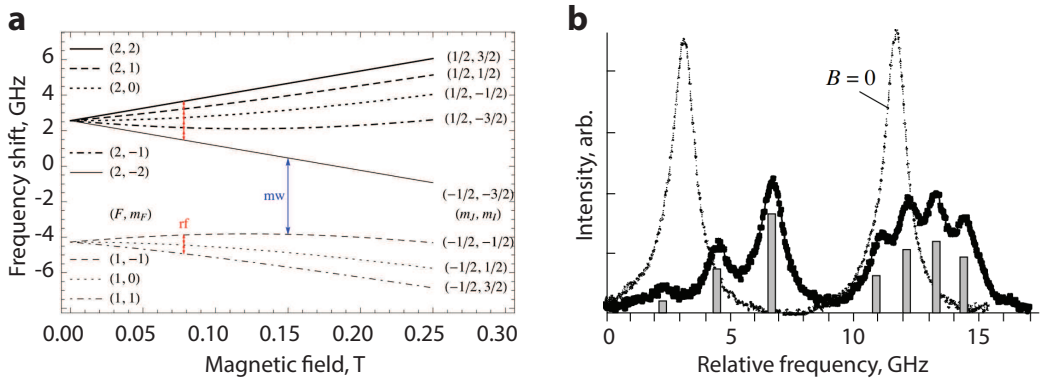

Figure 2.4: Zeeman shift of ^{87}Rb hyperfine transition. **a.** Hyperfine transition is split in frequency as magnetic field is applied. Figure is from [50]. **b.** The measured flourescence spectrum reveals decoherence of hyperfine transition as well as reduced signal amplitude which makes measurement and tracking of a single transition difficult. The applied magnetic field is 0.0225 T. Figure is from [51].

have attempted crystal growth of magneto-optic material on other substrates with suitable crystal structures such as gadolinium gallium garnet [48]. And some even attempted wafer bonding of bulk magneto-optic materials with post polishing process which is very time-consuming and inevitably leads to a low yield rate [16, 49].

2.4.3 Disturbance to energy level transitions

Lastly, the requisite magnetic field bias can interfere and degrade performances of other nearby devices. One application where the optical isolator is used is within an atomic clock, a device for accurate timekeeping necessary for global positioning system, communication system, and even space exploration. Atomic clocks count the passage of time via counting the ticks of a reference oscillator that is extremely stable. The most stable and consistent oscillation is obtained from the energy transitions of an atom typically cesium-133 or rubidium-87. However, when the magnetic field is applied, the energy level transition used for the atomic clock can be disturbed from the Zeeman effect. Essentially, the energy level splits due to the energy of magnetic moment in the field and the energy difference ΔE of the split states

is given by

$$\Delta E = -\mu \cdot \mathbf{B} \tag{2.12}$$

$$= m_l \frac{e\hbar}{2m_e}\mathbf{B} \tag{2.13}$$

$$= m_l \mu_B B \tag{2.14}$$

where μ is the magnetic dipole moment, m_l is the magnetic quantum number, $\hbar$ is the planck constant, and μ_B is the Bohr magneton [50]. Therefore, ^{87}Rb energy levels are expected to split in frequency with increasing magnetic field strength as shown in Fig. 2.4a. Experimentally, such splitting can be observed in the fluorescence spectrum when the ^{87}Rb vapor is excited using an external laser as shown in Fig. 2.4b [51].

CHAPTER 3

ACOUSTIC AND OPTICAL WHISPERING GALLERY RESONATORS

3.1 Introduction

Figure 3.1: St. Paul's Cathedral where whispering gallery wave was first discovered. Located in London, UK.[1]

A whispering gallery is a circular structure with an internal path where sound can travel around with small attenuation. Thus, as the sound travels around near the circumference of a whispering gallery, even a small sound, or a whisper, can be heard loudly when an observer is near the inside edge of the structure. A great example of such structure is St. Paul's Cathedral in London where Lord Rayleigh first discovered and hypothesized how whispering gallery wave travels great distances [28]. In 1878, Lord Rayleigh

[1]Image from https://www.flickr.com/photos/mbiddulph/3730158004

discovered that the sound clings to the wall and travels within a thin layer inside the wall as opposed to the previous belief that the sound bounces off of the dome and focuses onto the other side of the whispering gallery [52].

In this thesis, we show that the light propagation direction can be controlled and thereby break the time-reversal symmetry using a technique that relies on both the acoustic and optical whispering gallery modes. Thus, we must review resonator systems that support the optomechanical interaction. Also, we will discuss how cavity-enhancement (resonance) allows us to explore the optical nonreciprocity in a compact optomechanical system along with their fabrication methods and waveguide-to-resonator light coupling techniques.

3.2 Acoustic whispering gallery mode

The study of acoustic wave and phonons have recently attracted attention for its relevance in phononic crystal [53, 54, 55], acoustic meta-materials (especially for the study of complex and negative refractive index material) [56, 57, 58, 59], mode conversion systems [60, 61], acoustic cloaking [62, 63, 64], acoustic nonreciprocity [41, 65], (photo-) acoustic imaging [66, 67, 68, 69], and so on. Also, the acoustic wave especially in a circular structure, a whispering gallery resonator, is of great importance in RF filter [70], nondestructive testing [71], and bio-sensing [72, 73, 74] owing to its high quality factor, ease of fabrication and potential for on-chip implementation [75]. Thus, we will briefly review the general acoustic wave theory and discuss its role in optomechanical interaction that eventually leads to the optical nonreciprocity.

The sound wave travels around the circumference of WGM resonators as the wave undergoes the total internal reflection continuously. When the resonator circumference L is an integer multiple m of acoustic wavelength λ, the acoustic wave traveling around the resonator constructively interfere (i.e. wave is on resonance) and the effective intracavity acoustic field amplitude is enhanced. In terms of the acoustic resonance frequency ω_m, this resonance condition is expressed as

$$\omega_m = m\pi \frac{v_s}{L} \tag{3.1}$$

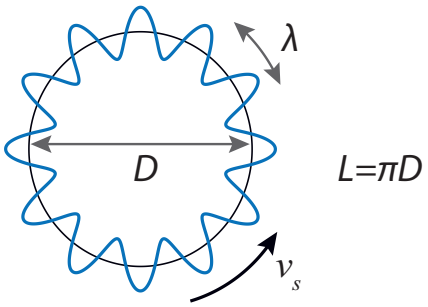

Figure 3.2: Under the resonance condition, the intracavity acoustic field amplitude is enhanced due to constructive interference.

where v_s is the speed of sound.

The deformation of a mechanical resonator at the resonance frequency can be visualized by solving the acoustic wave Helmholtz equation[2] using the finite element method in COMSOL. Using the geometric parameters of the actual resonator device used throughout this thesis, the simulation result reveals the available eigenmodes (Fig. 3.3), corresponding eigenfrequencies, and spatial locations of the modes. This information is used during the experiment as they provide a rough frequency range to look for the desired acoustic mode. Also, we will later use the acoustic mode simulation to compare against the optical mode simulation and verify the modal overlap which is one of the requirement for the observation of optomechanical effects [76]. This is critical for the demonstration of nonreciprocal light transmission.

Upon observation of the eigenmodes from Fig. 3.3, we notice a few key differences between the eigenmodes. First of all, the radial vibration (breathing) acoustic mode is a standing acoustic wave with zero propagation constant (Fig. 3.3a). This particular eigenmode supports optomechanical interaction that was used for many sensing applications [77, 78], but it does not support Brillouin scattering which require energy and momentum exchange between optical and acoustic modes which will be explained in the next chapter. The rest of the eigenmodes shown (Fig. 3.3b-f) are traveling acoustic wave with non-zero propagation vector that we can use for mediating Brillouin scattering process. Further, the modes can be categorized as longitudinal (Fig. 3.3b) and transverse (Fig. 3.3c) based on the oscillation direction (Fig. 3.4). The longitudinal wave (such as a sound wave in air) is a wave that propagates

[2]Helmholtz equation is a generic differential equation applicable to both acoustic and optical waves and is given by $\left(\nabla^2 + k^2\right)\psi = 0$. For the acoustic wave, $k = \frac{\omega}{c}$ and ψ is the acoustic pressure. An expression for the external source may be added on the RHS.

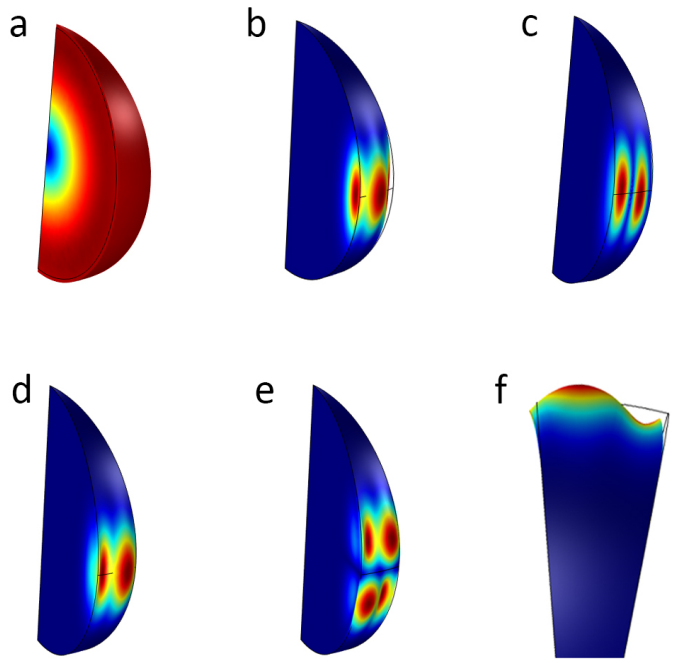

Figure 3.3: Various acoustic mode shapes are simulated using COMSOL Multiphysics. Silica microsphere of size 160 μm in diameter is used. M-number (azimuthal order) is 20. **a.** Radial vibration (breathing) acoustic mode. This acoustic mode is stationary as the entire microsphere expands and contracts without propagating. **b.** Longitudinal acoustic mode. The periodic density oscillation occurs only in the direction of the wave propagation. **c.** Transverse acoustic mode. The center of two antinodes are located at a different polar coordinates. **d.** Rayleigh acoustic mode. **e.** Second order (polar) Rayleigh acoustic mode. **f.** Top-down view of Rayleigh acoustic mode. The Rayleigh acoustic mode is composed of both longitudinal and transverese components.

through a medium with density changes parallel to the propagation direction. As sound travels in air, the air experiences rarefraction and compression as it transfers the density fluctuation. Within a solid resonator, the acoustic speed is estimated as [79]

$$c_L = \sqrt{\frac{E\,(1-\sigma)}{\rho\,(1+\sigma)\,(1-2\sigma)}} \tag{3.2}$$

where E is Young's modulus, σ is Poisson's ratio, and ρ is material density.

On the other hand, the transverse wave propagates through a medium with density changes perpendicular to the propagation direction. One example of a

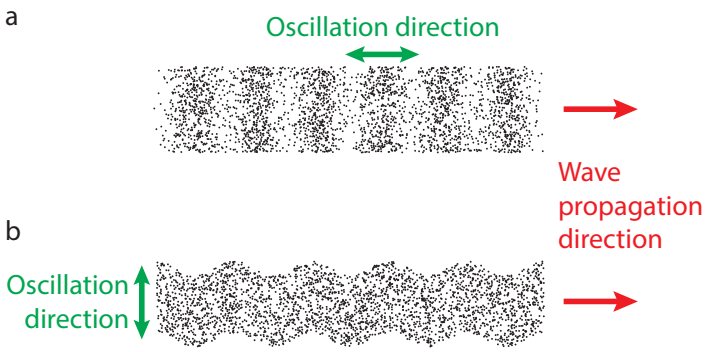

Figure 3.4: **a.** Longitudinal and **b.** transverse waves are represented with particles. Longitudinal wave propagates with particles oscillating in the same direction (parallel). On the other hand, transverse wave propagates with particles oscillating in the transverse direction (perpendicular).

transverse wave is electromagnetic wave which propagates as the electric and magnetic fields oscillate perpendicular to the propagation direction in free-space. Fig. 3.4b is an illustration of a transverse wave propagating through a medium. The Within a solid resonator, the acoustic speed is estimated as [79]

$$c_S = \sqrt{\frac{E}{2\rho\,(1+\sigma)}} \tag{3.3}$$

Lastly, the Rayleigh wave is a hybrid acoustic wave that is combination of longitudinal and transverse waves and is localized within the surface of a medium (Fig. 3.3d - f). As oppose to longitudinal and transverse wave which can exist as a bulk acoustic wave traveling deep within the medium, Rayleigh wave is strictly confined within the surface. If Rayleigh wave is carefully observed, the longitudinal and transverse components of the wave has a phase difference associated resulting in an elliptical motion of a point on the surface. The simulation of spherical resonator also reveals a distinct pattern where the displacement takes place in both longitudinal and transverse direction as shown in Fig. 3.3e, f. Within a material with small and positive Poisson's ratio ($0 < \sigma < 0.5$), the acoustic speed is estimated as [79]

$$c_R = \frac{0.87 + 1.12\sigma}{1+\sigma} \tag{3.4}$$

3.3 Optical whispering gallery mode

Shortly after Rayleigh's discovery of whispering gallery acoustic wave [2, 28], Raman and Sutherland proposed an optical analogue of the whispering gallery effect [80]. Conventional Fabry-Perot resonators composed of two highly reflective mirrors are prominently used for interferometric measurement techniques [81], increasing interaction length [82, 83], and optical filters [84, 85, 86]. However, the Fabry-Perot resonator was quickly replaced with the optical whispering gallery resonator in many places due to its small size[3], stability, ease of fabrication and high quality factor. Also, the whispering gallery resonator is appealing as a platform for the study of quantum optics [87,88] and quantum electrodynamics [89,90,91] as it provides a system where the acoustic and optical modes co-exist.

We also use the whispering gallery resonator as we manipulate the optomechanical effects for the demonstration of nonreciprocity. Thus, we must verify the modal overlap of acoustic and optical modes. Here, we will present simulations of optical whispering gallery modes for comparison against the acoustic whispering gallery mode simulation from the previous section.

Again, we rely on COMSOL and finite element method for solving the electromagnetic wave equation[4]

$$\left(\nabla^2 - n^2\frac{\omega^2}{c^2}\right)\psi = 0 \tag{3.5}$$

where ψ is either electric or magnetic field amplitude. As we deal with a microsphere, we perform a coordinate transformation (cartesian to spherical) and separation of variable[5] to obtain a solution

$$\psi_{lm}(r,\theta,\phi) = a_{lm} j_l(n_1 kr)\, Y_{lm}(\theta,\phi) \qquad r \le R \tag{3.6}$$

$$\psi_{lm}(r,\theta,\phi) = b_{lm} h_l(n_2 kr)\, Y_{lm}(\theta,\phi) \qquad r > R \tag{3.7}$$

where j_l and h_l are the spherical Bessel function and spherical Hankel function of order l respectively, n_1 and n_2 are the refractive indices of resonator

[3] Typically, the size of optical whispering gallery resonator is only restricted by the optical wavelength.

[4] Electromagnetic wave equation is a type of Helmholtz wave equation which was used for describing the acoustic wave also in the previous section. Also note that we use a scalar quantity ψ to denote the electric or magnetic field as we deal with a symmetric system.

[5] $\psi(r,\theta,\phi) = X(nkr)\, Y(\theta,\phi)$

and surrounding materials respectively, and R is the microsphere radius. Y_{lm} is a spherical harmonic given by the Legendre polynomial P_{lm}

$$Y_{lm}(\theta,\phi) = \sqrt{\frac{2l+1}{4\pi}\frac{(l-m)!}{(l+m)!}} P_{lm}(\cos\theta)\exp^{im\phi} \tag{3.8}$$

Then, we can find the solution by applying the continuity boundary conditions at the interface. From which we obtain a characteristic equation that we use to find q solutions corresponding to the radial mode number. m is the azimuthal mode number and $p = l - |m|$ is the polar mode number. Also, the solution is further separated into transverse electric (TE) and transverse magnetic (TM) based on the orientation of the radial component [52].

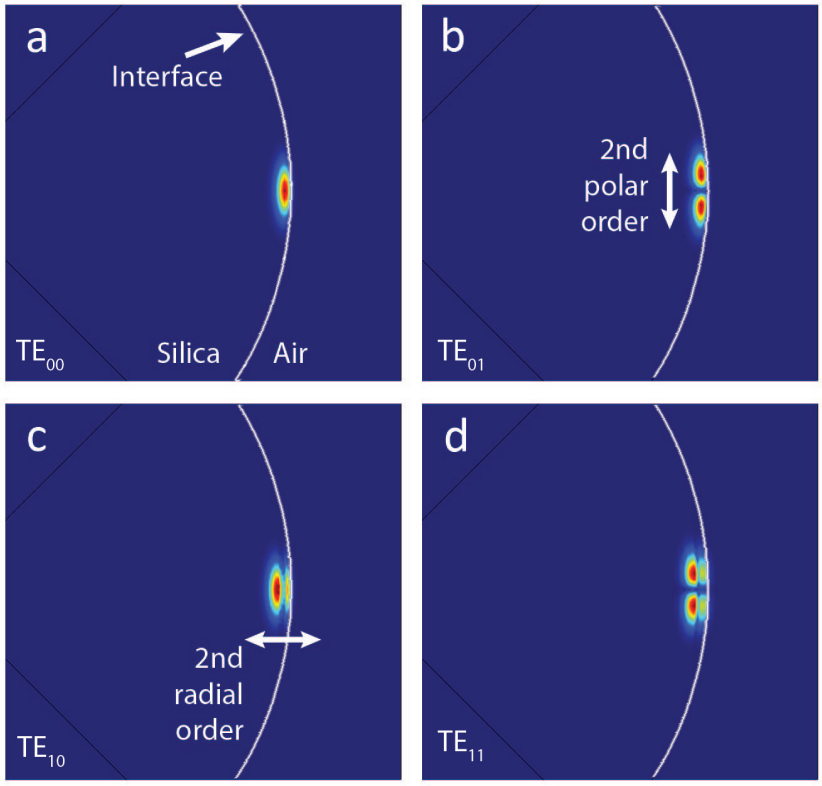

Figure 3.5: Various optical mode shapes are simulated using COMSOL Multiphysics. Optical field having 1550 nm wavelength in Silica microsphere of size 160 μm in diameter is used for simulation. M-number (azimuthal order) is 468. **a.** First order optical mode. **b.** Second polar order optical mode. **c.** Second radial order optical mode. **d.** Second polar and radial order hybrid optical mode.

Using the microsphere resonator geometry from the experiment, we can find the optical whispering gallery modes confined near the edge of the resonator as shown in Fig. 3.5. We chose silica for the resonator material because of its availability[6], ease of fabrication and low absorption at the desired operating wavelength of 1550 nm. Comparing against the acoustic mode simulation, we find that the first radial order modes (Fig. 3.5a, c) have good modal overlap with traveling acoustic waves with first polar order acoustic modes (Fig. 3.3b, c, d) which is necessary for the observation of optomechanical effects [76]. Also, it is important to note that there exists an electric field outside the resonator residing in the air. This is called evanescent field and is exponentially decaying as $\psi \sim \exp^{-kr}$ where k is an effective propagation constant defined as $k = \frac{2\pi}{\lambda}\sqrt{n_e^2 - n_1^2}$. The effective refractive index n_e is extracted from the eigenmode's dispersion relation considering geometric effect (microsphere curvature).

3.4 Characterizing parameters for whispering gallery resonators

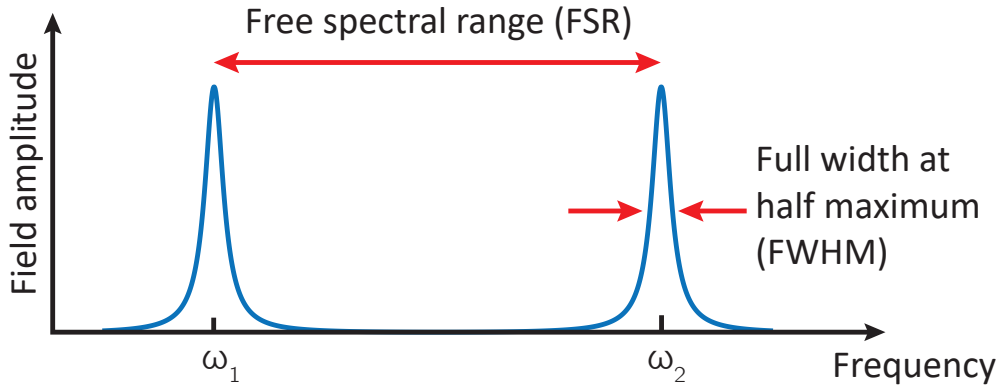

Figure 3.6: Resonator frequency spectrum example. Free spectral range and full width at half maximum are useful parameters characterizing the resonator.

In the previous section, we discussed the acoustic and optical eigenmodes of the whispering gallery resonators to gain perception of the mode shape.

[6]Silica is the most popular material for the fiber optic cable. We re-use such fiber optic cable by melting the tip to form a microsphere resonator. Detailed fabrication process will be explained in the next section.

Here, we further discuss the whispering gallery resonators by characterizing them analytically and describe their performance in regards to the resonant enhancement.

For that purpose, the two most commonly used quantities are the finesse and quality factor (Q-factor). The quality factor is an indication of the resonator's damping strength and is a often measured as a ratio of energy stored in the resonator versus energy loss per cycle. Analytically, the Q-factor is expressed as

$$Q = \frac{\omega_o}{\kappa} \tag{3.9}$$

where ω_o is the resonance frequency. Similarly, the finesse F of the resonator is an indication of how many round trips a single photon can make before decaying and is defined as

$$F = \frac{2\pi}{1-\rho} \tag{3.10}$$

where ρ is a fraction of power left in the resonator after one round trip. In the frequency spectrum (Fig. 3.6), the finesse can also be estimated as a ratio of the free spectral range (FSR) and the full width at half maximum (FWHM). As we approximate the free spectral range as $FSR = \pi c/L$, the finesse is expressed as

$$F = \frac{\pi c}{\kappa L} \tag{3.11}$$

where κ is the loss rate and L is the resonator circumference (optical path length).

3.4.1 Experimental measurement of quality factor

Experimentally, the optical quality factor is be measured from the transmission spectrum of optical resonance. By frequency sweeping a tunable laser, the optical resonance is captured in the frequency domain as shown in Fig. 3.7. As we will discuss in the next section, the quality factor and loss rate are dependent on many factors including the optical coupling coefficient which describes how much optical field enters and exits the resonator.

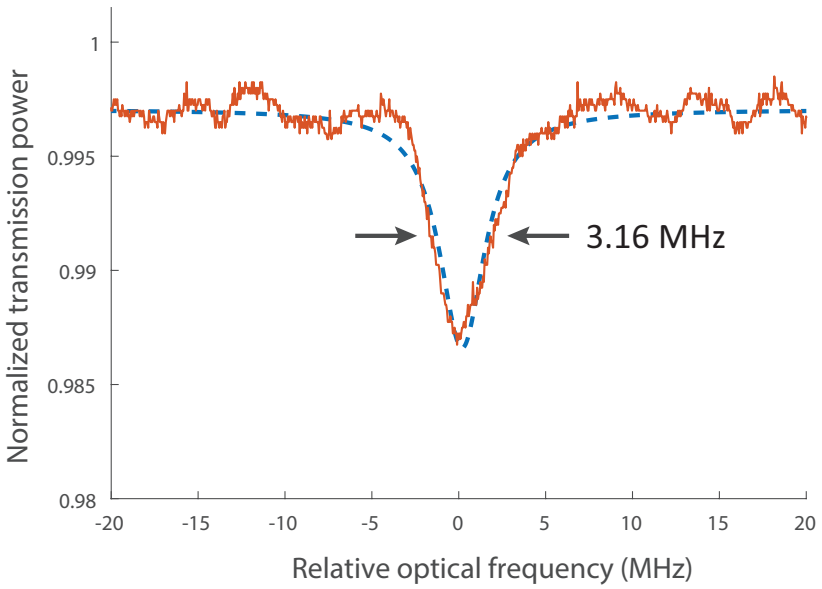

Figure 3.7: Optical transmission spectrum showing optical resonance while under-coupled (∼98.7% of light transmitted without coupling to resonator). Full-width-at-half-maximum is 3.16 MHz. The resonator's intrinsic quality factor is estimated as 61 million. Laser wavelength used is 1.55 μm (193 THz in frequency). Microsphere resonator of size ∼170 μm in diameter is used. (Red-solid) Experimental data. (Blue-dashed) Lorentzian fit.

Thus, we physically place the resonator to achieve a minuscule optical coupling allowing us to measure the intrinsic optical quality factor without the influence of external factors. Using Eq. 3.9, the quality factor is estimated as (193 THz)/(3.16 MHz) = 61 million.

3.5 Resonator loss mechanisms

The resonator loss rate, found in the quality factor and finesse equations, is an important parameter determining the resonant enhancement which directly relates to the device performance when a whispering gallery resonator is used. For example in sensing applications, the quality factor is directly related to the sensitivity [72, 74, 78, 92, 93]. Thus, a tremendous effort is put into minimizing the loss rate [75, 91, 94]. Here, we discuss basic principles of how the loss rate is determined in an attempt to understand ways of improving the resonator design.

The resonator loss consists of several different mechanisms namely material

loss, geometric loss and coupling loss. The total loss rate is simply the sum of individual loss rates arising from the said mechanisms as

$$\kappa = \sum \kappa_i \tag{3.12}$$

where i = material, geometry and coupling losses. And as the resonator loss rate κ and quality factor Q are inversely related (Eq. 3.9), the inverse of quality factor contributions can be added together to find the total quality factor as [95]

$$\frac{1}{Q} = \sum \frac{1}{Q_i} \tag{3.13}$$

3.5.1 Material loss

When conceiving a whispering gallery resonator device, the material choice is often decided first. Regardless of the design, the material used for the fabrication of optical device must have a small absorption coefficient in the operating wavelength range in order to minimize loss and maximize the quality factor. For that matter, the band-gap structure of optical material is used to estimate the absorption coefficient. A vast library of material band-gap data exists with the advancements of semiconductor industry. Once the absorption coefficient is calculated, the loss rate associated with material absorption can be estimated as

$$\kappa_m = \frac{\omega_o \alpha \lambda}{2\pi n} \tag{3.14}$$

where ω_o is eigenfrequency, α is absorption coefficient, λ is wavelength and n is refractive index.

The experimental results presented in this thesis utilize exclusively silicon dioxide (silica). Silica is a widely available material with extremely small absorption coefficient at the test wavelength of 1550 nm (Fig. 3.8). In fact, the transcontinental optical communication network also relies on the silica fiber-optic cable for its excellent optical properties at 1550 nm. Thus, the whispering gallery resonators made with silica can have the quality factor exceeding 44 million in a relatively small device [22] and a quality factor as high as 875 million has been experimentally demonstrated with larger

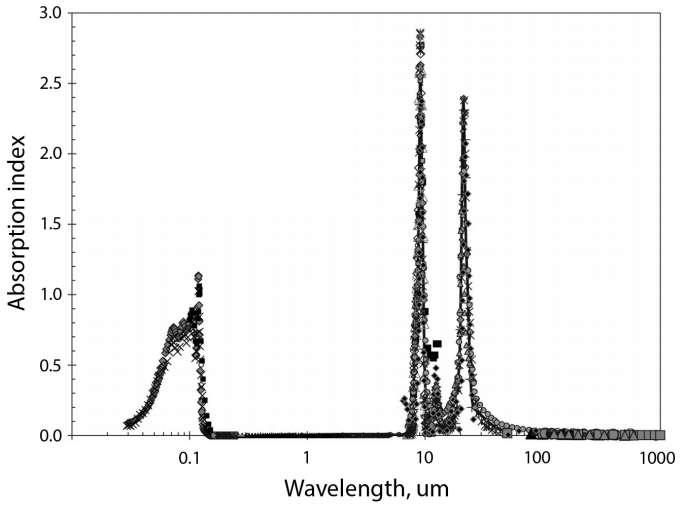

Figure 3.8: Absorption spectrum of silica shows an excellent light transmission from visible to mid-IR wavelength range. Figure is from [96].

diameter devices [75, 97].

3.5.2 Geometric loss

In addition to material loss, the geometry of optical devices plays an important role in the loss rate. In short, the shape of a resonator must retain optical mode in a small region (comparable to optical wavelength) without any inhomogeneity that can create additional loss from the scattering.

Light is extremely sensitive to imperfections in the optical path. Any defects such as surface roughness and micro-sized dust particles introduced during the fabrication process or during storage will lead to the scattering loss. Based on the Rayleigh scattering theory, it is estimated that a particle with rms size σ leads to the scattering associated loss rate

$$\kappa_s = \frac{2\pi^2 \omega_o \sigma^2 B}{\lambda^2 D} \tag{3.15}$$

where ω_o=eigenfrequency, B=dust particle correlation length, λ=wavelength, and D=resonator diameter [97]. In order to minimize such scattering loss, it is advised to fabricate the whispering gallery resonator in a particulate-free cleanroom environment and to perform tests as soon as the device is prepared. For a prolonged storage, placing the resonator in either vacuum or dry-gas (such as N_2) chamber is recommended.

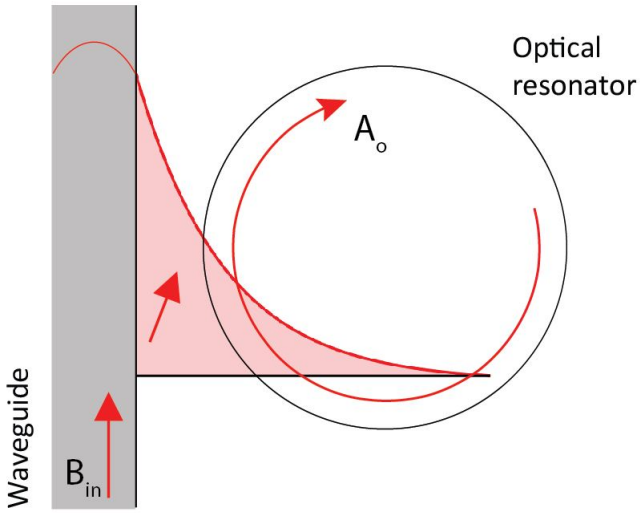

Figure 3.9: Evanescent coupling of light. Light propagating in waveguide can couple to optical resonator when placed in proximity. Also, intracavity light can couple out and exit at the far end of waveguide.

Another aspect of the resonator geometry that affects loss rate is the resonator size. Even though light is confined within the whispering gallery resonator by the total internal reflection, every curvature causes a small fraction of light to be lost radiatively. This problem is easily prevented in the design stage by increasing the resonator diameter. For instance, a resonator with diameter D that is fifteen times or larger than the optical wavelength ($D \geq 15\lambda$) has an associated quality factor contribution of $Q_{rad} > 10^{11}$ [97].

3.5.3 Coupling loss

The last loss mechanism to be discussed here is an extrinsic loss κ_{ex} due to coupling. Even though the loss rate increases, we introduce an optical coupler to the resonator system which opens a channel for the light input and output in order to make a useful device. The coupling loss requires a special treatment as it is directly related to the light coupling into the whispering gallery resonator and it is the only loss rate that can be controlled even after the fabrication process.

In case of a Fabry-Perot resonator, the coupling rate is determined from the reflectivity of mirrors. However, whispering gallery resonator relies on the evanescent coupling (see Ch. 3.6) in which the coupling rate is a function of the resonator and coupler distance. Using a linear stage with nanometer

resolution[7], we can control the coupling rate as well as the intracavity optical field.

The other loss rates discussed previously constitute the intrinsic loss rate κ_o which only acts as decay channel. On the other hand, the coupling loss rate also governs the light entering the system. Thus, the intracavity optical field a is expressed as

$$\dot{a} = -\frac{\kappa}{2}a + i\Delta a + \sqrt{\kappa_{ex}}a_{in} \tag{3.16}$$

where the total loss rate κ is the sum of extrinsic (coupling) and intrinsic loss rates ($\kappa = \kappa_{ex} + \kappa_o$), the laser detuning Δ is a difference between the laser frequency ω_L and the resonance frequency ($\Delta = \omega_L - \omega_o$), and a_{in} is the optical field input to the system. The optical field input to the system a_{in} is defined as

$$a_{in} = a_{out} + \sqrt{\kappa_{ex}}a \tag{3.17}$$

where a_{out} is the reflected optical field that did not couple into the resonator. This description of resonator system is called input-output formalism [98,99]. This is useful in understanding how coupling rate affects the intracavity optical field build up. A special case worth noting is when the coupling loss rate is equal to the intrinsic loss rate ($\kappa_{ex} = \kappa_o$). When we combine Eq. 3.16, 3.17 and assume the laser is on resonance, the reflected optical field disappears ($a_{out} = 0$) which indicates that the optical field input a_{in} is completely coupled into the resonator. This is called the critical coupling condition. Systems incorporating the whispering gallery resonator typically operate at the critical coupling condition for the ideal performance.

3.6 Resonator-waveguide light coupling techniques

As menionted earlier, the optical coupler is an essential device for making use of the whispering gallery resonator. Thus, the optical coupler and resonator pair is found in countless applications including laser cooling [100], induced

[7]Typically, a piezo-electric actuator with a high precision linear stage is used for such motion control. We use Physik Instrumente P611.3 NanoCube for precise control of tapered waveguide coupler with respect to the resonator.

transparency systems [10,22,101,102,103], optical isolators [10,14,23,47,104], particle sensors [78,105], frequency combs [106,107,108,109], optomechanical AFMs [110, 111], and many more. We use the tapered optical fiber coupler which is one of the most widely used light coupling technique, but there exists other methods that may fit better for each individual applications. Here we review a few light coupling techniques and how they are set up.

3.6.1 Evanescent light coupling

The optical coupling techniques discussed in this section achieves the coupling from one waveguide to another based on the evanescent wave coupling. When the optical field is confined via total internal reflection, the propagation vector has an imaginary component outside the waveguide. The electric component of evanescent wave is expressed as

$$E = E_o \exp^{\mp \alpha y} \exp^{i(k_i x - \omega t)} \tag{3.18}$$

where α is the propagation constant expressed as

$$\alpha = k_i \sqrt{\left(\frac{n_1}{n_2} \sin\theta_i\right)^2 - 1} \tag{3.19}$$

When there is no supported optical mode outside the waveguide, the field decays exponentially with a penetration depth defined as [112]

$$d = \frac{\lambda n_2}{4\pi} \sqrt{\left(\frac{n_1}{n_2} \sin\theta_1\right)^2 - 1} \tag{3.20}$$

Now, if we consider placing a second waveguide within the penetration depth, the propagation constant α suddenly becomes real with the correct value of refractive index. In other words, the energy transfer occurs between the two waveguides even if the optical modes are protected by the total internal reflection. This behavior is analogous to quantum tunneling where an electron tunnels through the energy barrier.

Once the waveguide and resonator pair is placed nearby, the energy transfer between the two is governed by the coupled-mode theory [113]. When the coupling is enabled, the field in waveguide E_a enters the resonator and the

field in resonator E_b enters the waveguide as

$$\frac{dE_a}{dz} = -i\beta_a E_a + i\kappa_{ab} E_b \tag{3.21}$$

$$\frac{dE_b}{dz} = -i\beta_b E_b + i\kappa_{ba} E_a \tag{3.22}$$

where β is the propagation constant and κ is the coupling coefficient. The coupling coefficients are not necessarily equal in the coupled mode theory, but we can assume $\kappa \equiv \kappa_{ab} = \kappa_{ba}$ in waveguide-resonator coupled system due to the reciprocity theorem. The coupling coefficient is a function of modal overlap which can be expressed as

$$\kappa = \frac{\omega \epsilon_o}{4} \left(n_s^2 - n_o^2\right) \iint\limits_S \left(\mathbf{E}_a^t \cdot \mathbf{E}_b^{t*} + E_a^\phi E_b^{\phi *}\right) r dr d\theta \tag{3.23}$$

The general solution to the above coupled mode theory equations is

$$E_a(z) = \left(A_1 \exp^{i\psi z} + A_2 \exp^{-i\psi z}\right) \exp^{-i\delta z} \tag{3.24}$$

$$E_b(z) = \left(B_1 \exp^{i\psi z} + B_2 \exp^{-i\psi z}\right) \exp^{i\delta z} \tag{3.25}$$

which can be treated as a typical initial-valued problem to find the final solution

$$E_a(z) = \left[\left(\cos(\psi z) + \frac{i\delta}{\psi} \sin(\psi z)\right) E_{a,o} - \frac{i\kappa}{\psi} \sin(\psi z) E_{b,o}\right] \exp^{-i\delta z} \tag{3.26}$$

$$E_b(z) = \left[-\frac{i\kappa}{\psi} \sin(\psi z) E_{a,o} + \left(\cos(\psi z) + \frac{i\delta}{\psi} \sin(\psi z)\right) E_{b,o}\right] \exp^{i\delta z} \tag{3.27}$$

where $\delta = \frac{1}{2}(\beta_a - \beta_b)$ and $\psi = \sqrt{\kappa^2 + \delta^2}$. In case the two modes are phase-matched $\beta_a = \beta_b$, a complete power transfer can be observed with the critical coupling condition as discussed in Ch. 3.5.3.

3.6.2 Tapered optical fiber coupler

First, we review the tapered optical fiber coupling technique that uses a thinned down optical fiber for injecting light into the whispering gallery resonator. First demonstrated by J. C. Knight, the tapered fiber coupler is a technique based on the principles of evanescent light coupling [114]. Com-

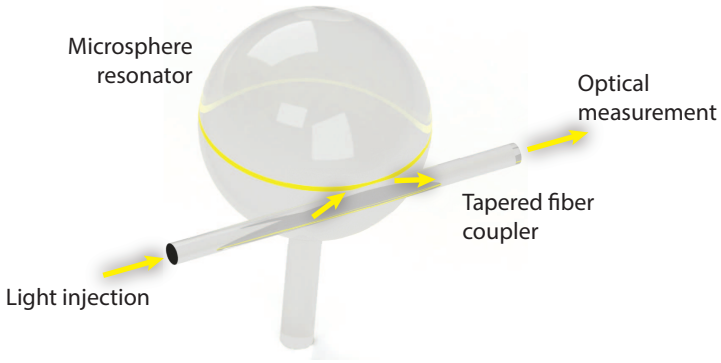

Figure 3.10: 3D rendering of microsphere resonator with tapered optical fiber coupler. When the resonator-waveguide gap is reduced below the laser wavelength, optical field evanescently couple. Yellow line in the microsphere resonator indicates the region where the optical mode is confined.

pared to other light coupling techniques such as freespace coupling [115] or prism coupling [116], tapered fiber coupler is more easily fabricated and maneuvered while still allowing high coupling efficiency.

The optical fiber used in communication systems has a thick cladding layer that surrounds the core to prevent light leakage[8]. According to Eq. 3.20, the evanescent field resides inside the cladding layer and coupling to the resonator is physically prohibited. Thus, we reduce the fiber diameter down to the size comparable to the laser wavelength. This allows us to have enough evanescent wave penetration depth and space for the resonator placement nearby.

3.6.3 Fabrication of tapered optical fiber coupler

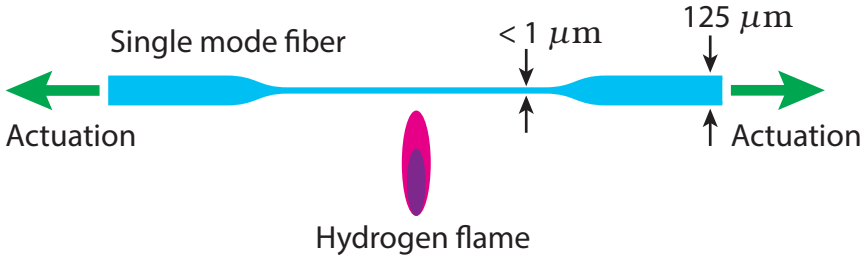

Figure 3.11: Tapered coupler fabrication. A single mode fiber is pulled in opposite direction while heat from hydrogen flame is applied.

[8]Single mode optical fiber such as Corning SMF-28e+ has a diameter of 9 μm core and 125 μm cladding.

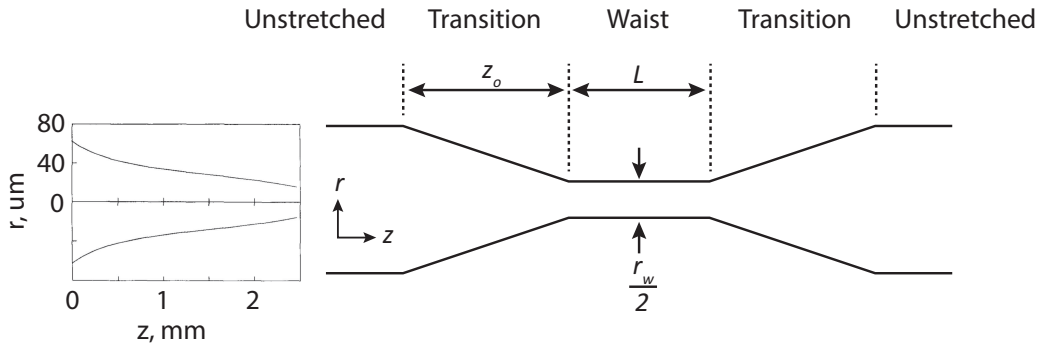

Figure 3.12: Schematic of tapered fiber coupler. An optical fiber is stretched to form a waist region where the diameter is smaller than the laser wavelength to allow evanescent coupling. The transition region must follow adiabatic profile to minimize insertion loss. (left) Example of adiabatic tapered fiber coupler profile. Figure is from [117]

We fabricate the tapered optical fiber coupler from Corning SMF-28e+ fiber preform by applying high heat (hydrogen flame) and simultaneously applying tension as shown in Fig. 3.11. Using this technique, a single mode fiber with outside diameter of 125 μm is scaled down to sub-μm in diameter.

The key to successful tapered fiber coupler fabrication lies in achieving the diameter below laser wavelength with adiabatic profile. In short, the final diameter must be comparable or smaller than laser wavelength to allow large evanescent coupling and the transition between the un-pulled fiber to the tapered down region must be slow and smooth (Fig. 3.12). Specifically, the adiabatic tapered fiber profile is expressed as

$$\frac{dr}{dz} = -\frac{r}{2\pi}\left(\beta_1 - \beta_2\right) \tag{3.28}$$

where β_1 and β_2 are the numerically calculated propagation constants of fundamental and second order optical modes within fiber. After solving for z as a function of r, the inverse $r(z)$ can be calculated numerically.

In order to achieve the desired adiabatic profile (Fig. 3.12), the flame brushing technique is often used [66,118]. In addition to tapered fiber pulling technique shown in Fig. 3.11, the flame torch is attached to a fast-moving motorized stage to apply heat to specific regions of tapered fiber. The tapered fiber coupler produced using the flame brushing technique is often used for quantum optics experiments requiring extremely high transmission (>99.95% transmission) [14, 119, 120].

3.6.4 Other light coupling methods

In addition to evanescent coupling using tapered optical fiber coupler, there are many other light coupling techniques. Of those, prism coupling and free-space coupling techniques are briefly discussed to offer a few alternatives.

More traditional light coupling method is the prism coupling. A prism typically made of high index material is used to focus light into a local region where the resonator is placed nearby. Similar to tapered fiber coupler, the light can couple from the prism to the resonator with evanescent wave coupling. The prism coupler is more robust to the environment (such as humidity) and is easier to handle. However, the maximum coupling efficiency achieved is rather low at only ~80% [95].

Compared to the tapered fiber method, the prism coupling setup is more complex with the specific requirements for the angle of incidence expressed as

$$\theta_p > \sin^{-1}\left(\frac{n_o}{n_p}\right) \tag{3.29}$$

where n_o and n_p are the refractive indices of the surrounding medium and prism respectively. Also, the phase matching condition

$$k_o n_p \sin\theta_p = \beta_m \tag{3.30}$$

is required for the efficient light coupling. k_o is the propagation vector in the surrounding medium and β_m is the propagation constant.

The last light coupling method discussed here is the free-space coupling.

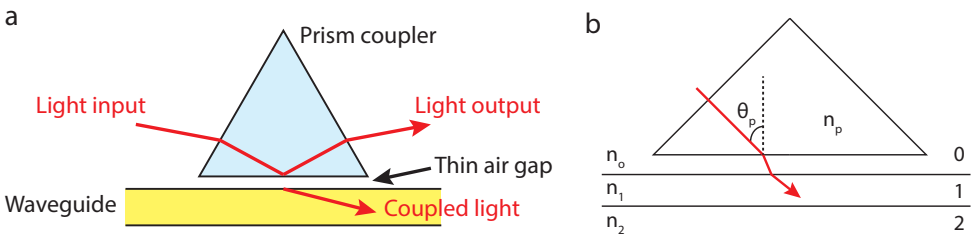

Figure 3.13: **a.** Prism coupler can be used to evanescently couple light into resonator or waveguide. The air gap thickness controls the coupling efficiency. **b.** Illustration showing definition of refractive indices n_i $(i = 0, 1, 2, p)$ and incident angle θ_p.

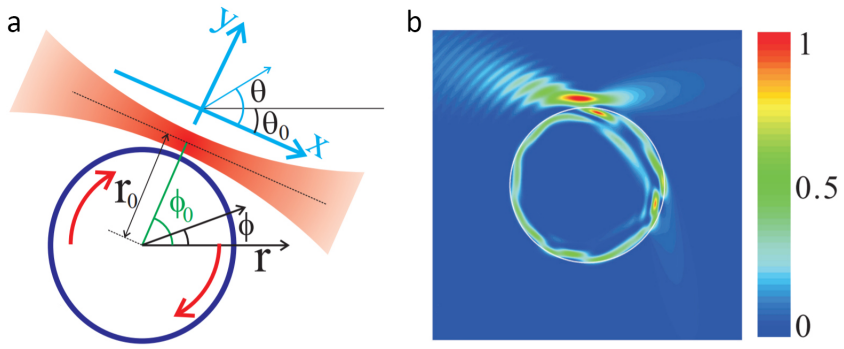

Figure 3.14: **a.** Incident Gaussian beam enters the resonator when the beam waist crosses the resonator edge. **b.** Simulation of light coupling into the resonator. Figure is from [121].

The free-space coupling is very unique in that the coupler is not placed in proximity of the resonator. Instead, the incident Gaussian beam propagating on top of the resonator is allowed to couple to the resonator as shown in Fig. 3.14a. As oppose to resonator-to-coupler distance controlling the coupling efficiency, the free-space coupling efficiency is determined by matching or mismatching of radiative to non-radiative loss of resonator. However even at the optimal point, the coupling efficiency is only ∼20% [121] and thus, this technique is used only when the placement of a physical coupler is hindered [122, 123].

3.7 Fabrication of optomechanical resonators

Select optomechanical resonator types and their fabrication methods are discussed in this section. Various optomechanical resonators are developed for different applications depending on the requisite quality factor, chip-scale process compatibility, resonator's working environment, and etc. Here we review the microsphere resonator that we use for the demonstration of nonreciprocity as well as other resonators that are commonly found in optomechanical experiments.

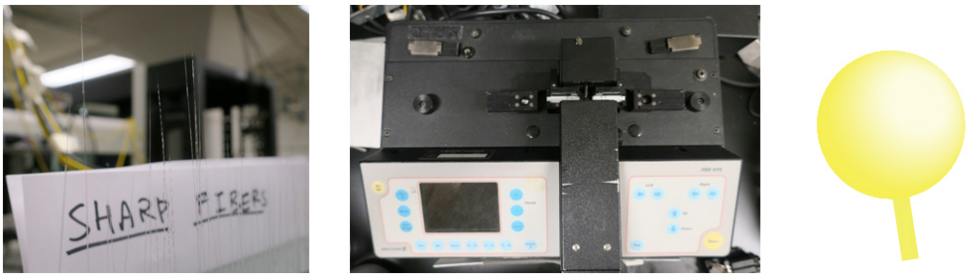

Figure 3.15: Broken tapered fiber (left) is metled in fusion splicer (middle) to form a microsphere resonator with a thin stem (right).

3.7.1 Microsphere resonator

The first type of resonator discussed here is the microsphere resonator derived from the optical fiber. It is fabricated from the tapered optical fiber coupler that was collected when it is broken or retired due to low transmission. As the coupler and resonator are fabricated with the same material, an excellent refractive index matching leads to an efficient light coupling. However, the resonators can be made from nearly any dielectric materials given the optical transmission spectrum with low absorption at the laser wavelength in use. The use of different resonator material is discussed in Ch. 8.1.

For the fabrication, the tip of broken fiber is melted to naturally form a sphere from surface tension. The heat can be supplied by CO_2 laser, hydrogen flame or electric arc discharge from a fusion splicer (Ericsson FSU 975). Using fusion splicer is recommended to ensure high Q-factor as other method may require additional processing such as annealing. The microsphere may be fabricated from the optical fiber preform for creating a very large resonator. However, we strictly use the broken tapered fiber as a thinner stem is less likely to interfere with the optical mode and it allows the fabrication of smaller microsphere resonators less than the size of the cladding (sub-125 μm).

3.7.2 Microcapillary microfluidic resonator

The capillary resonator is another type of widely used resonator that incorporates a hollow core allowing fluids to flow inside (Fig. 3.16). With such a distinct feature, the capillary resonator makes an ideal candidate for optofluidic applications such as sensing of particles suspended in liquids [78, 93].

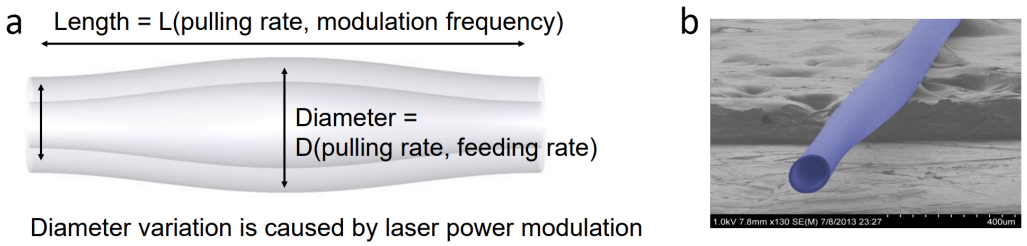

Figure 3.16: **a.** Capillary resonator has a hollow core where fluids can flow through. The ratio of core diameter to capillary thickness is determined by the capillary preform goemetry. **b.** False-color SEM image of capillary.

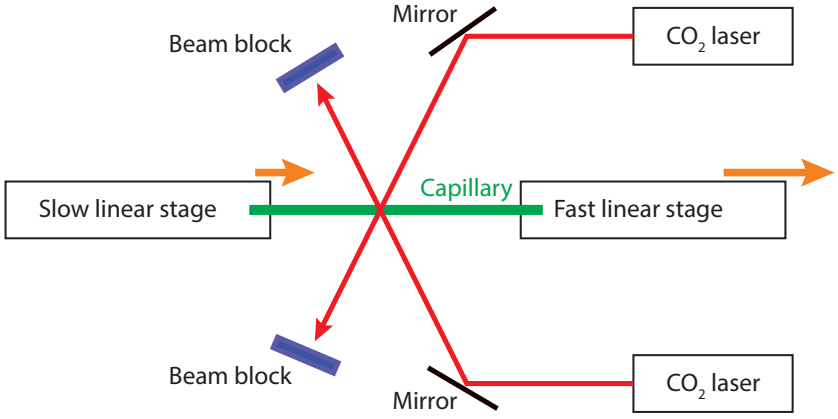

Figure 3.17: Capillary resonator fabrication setup. Two CO_2 lasers melt capillary preform while linear stages stretch to form periodic variation in diameter and make bulges where acoustic and optical modes are confined.

The capillary resonator fabrication starts from a silica capillary preform. Even though the capillary is already a circular structure, the preform has no variation in diameter and is unable to confine acoustic and optical modes within a small region. Similar to tapered optical fiber fabrication, the capillary is thinned down to create bulges where the acoustic and optical modes will be confined. The pulling process is described in Fig. 3.17. The CO_2 laser melts the capillary preform[9] while the linear stages stretch and feed the material. Using two CO_2 laser directed towards opposite sides of the capillary preform ensures uniform heating which creates more circular resonator having higher Q-factor. In addition, the two lasers' powers are carefully controlled to achieve uniform heating. While the heat is applied, the feed-

[9]The CO_2 laser with 10.5 μm wavelength is used to melt the silica capillary because of the high absorption coefficient according to the silica absorption spectrum as shown in Fig. 3.8.

ing (slow linear stage) and pulling (fast linear stage) rates are controlled to create a periodic variation in diameter as shown in Fig. 3.16.

3.7.3 Microdisk resonator on-chip

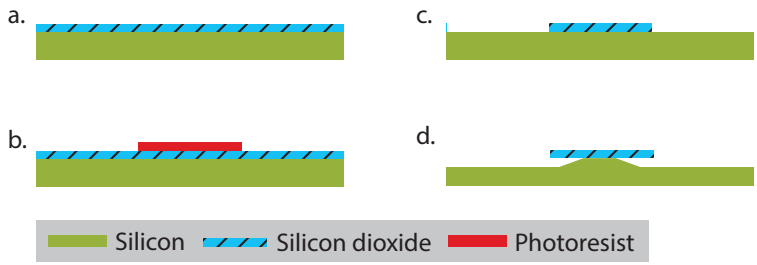

Figure 3.18: **Outline of on-chip resonator fabrication procedure. a.** Silicon wafer with SiO_2 film is purchased. Oxide can also be thermally grown on silicon wafer. **b.** Photoresist is spun on, patterned and developed. **c.** SiO_2 is etched using RIE or HF. **d.** Undercut is made by etching silicon using XeF_2 etcher.

The microdisk resonator was developed in an effort to fabricate an optomechanical resonator on-chip. Due to the nature of photolithography and microfabrication process, it is also an excellent choice for fabricating many resonators in a single fabrication run. The quality factor of these resonators are generally also very high when wet-etching is used for defining the resonator edges. The light coupling, however, adds a complexity to the experimental setup as the placement of tapered fiber coupler (or any other couplers) is difficult. Alternate method is to use a grating coupler which requires the dry-etching technique lowering the quality factor.

The microdisk resonator fabrication procedure is outlined in Fig. 3.18. A silicon wafer with up to 10 μm of silicon dioxide (SiO_2) grown on top is readily available commercially[10]. Other resonator materials such as silicon nitride [125, 126, 127], gallium nitride [128], lithium niobate [129, 130], and even silicon [131, 132] can be used in place of SiO_2. These materials in combination with SiO_2 is also useful for defining on-chip waveguide due to silicon's high refractive index[11]. For the fabrication of resonators on-chip

[10]We purchase silicon wafers with thermal oxides from WRS materials. Thicker oxides can be grown by wet oxidation technique but is economically not feasible with slowing of growth rate according to the Deal-Grove model [124].

[11]Silicon refractive index (3.48 at 1.55 μm) is much higher than many dielectrics.

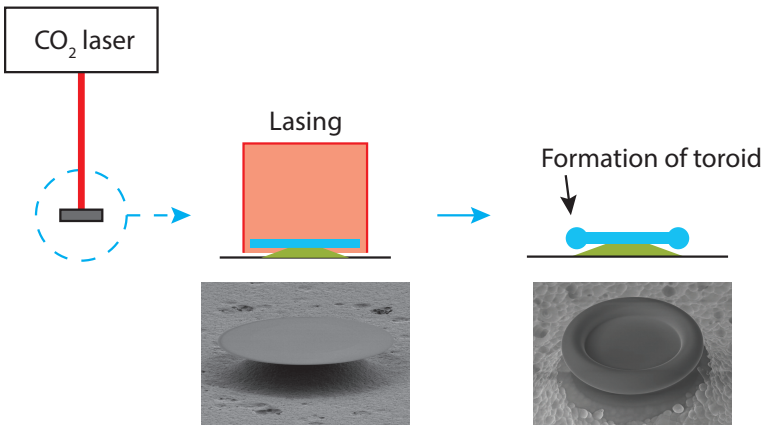

Figure 3.19: Fabrication of toroid resonator. The CO_2 laser provides the heat from the top side of the disc resonator. The laser is focused such that the beam diameter is slightly larger than the diameter of the resonator. As the suspended region of the disc resonator melts, the material reflows and forms a toroid. Thus, undercut depth determines the torus geometry. In the process, the silicon substrate acts as a heat sink to prevent damage to the resonator.

(Fig. 8.1), we used a silicon wafer with 2.5 μm of thermally grown SiO_2. With the substrate prepared, the resonator design is patterned on the photoresist using either photolithography or electron-beam lithography for smaller, sub micron features. The SiO_2 layer is etched using reactive ion etching (RIE) or chemically using hydrogen fluoride (HF). SiN_x can be etched using RIE or chemically using hot phosphoric acid (H_3PO_4). RIE-etched device typically has a vertical but rough sidewall. On the other hand, HF-etched device has a slanted but smooth sidewall. The dry-etched device may be further processed to remove roughness in sidewall [133, 134, 135]. To release the resonator from the silicon substrate, xenon difluoride (XeF_2) etching is used. XeF_2 aggressively etches the silicon but stays relatively inert to dielectrics such as SiO_2 and SiN_x (selectivity to silicon of 1:1000 or higher) [136]. This releasing or undercut prevents the light from escaping the resonator as the air acts as a low index cladding. The detailed fabrication procedure is given in Appendix C.

After the disc resonator is fabricated, it can be further heated by a CO_2 laser to form a toroid resonator (Fig. 3.19). The toroid resonator can have higher quality factor as the surface roughness is removed by lasing and the optical field is better confined within the resonator [75, 137]. However, the

melting process is typically not compatible with on-chip waveguides[12].

3.7.4 Other optomechanical resonators

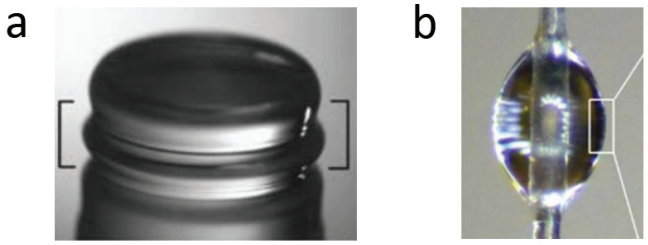

Figure 3.20: **a.** CaF_2 optical resonator. Image from [139]. **b.** Liquid droplet resonator. Image from [140].

The list of resonators presented in this chapter is only a small fraction of many resonator types. There are simply too many resonators to cover a complete list of them in this thesis. There are two more optomechanical resonators that I believe are worth mentioning though.

The first is the CaF_2 resonator fabricated by diamond turning a few-millimeter-sized CaF_2 monocrystal workpiece (Fig. 3.20a.). Although the image shown displays a little resemblance of a resonator, the optical field is well-confined within the region with slightly larger diameter indicated by the bracket. As the resonator starts from a nearly defect-free monocrystal, the scattering loss is extremely small. The experimentally measured optical Qaulity factor exceeding 50 billion has been reported previously [107, 139, 141].

The second optical resonator shown on the right (Fig. 3.20b.) is also very unique as it is in the liquid state. The so-called liquid droplet resonator is formed by creating a small fluid channel connected to a liquid reservoir and the resonator shape is formed by itself through surface tension of liquid used [122, 123, 140, 142]. Although the optical and acoustic properties of liquid resonators are poor compared to the solid-state devices, they provide a truly unique platform for the study of liquid-gas interface and how droplet resonators interact with the surrounding environment.

[12]Zhang and Armani have demonstrated an on-chip waveguide compatible with CO_2 melted toroid resonator, but is economically not feasible [138].

CHAPTER 4

BRILLOUIN SCATTERING

4.1 Introduction

The light scattering occurs due to fluctuations in properties of the light propagating medium. From this process, we can often extract useful information about the medium. Rayleigh scattering and Mie scattering are examples of elastic light scattering caused from inhomogeneities such as defects in material or density fluctuations [28]. As many physical properties are relatable to the material density, Rayleigh and Mie scattering are used in various sensing applications such as gas concentration [143], temperature [144] and gas velocity [145] measurements. Raman scattering is an example of inelastic scattering caused from the molecular vibrational modes (optical phonon modes[1]) [146,147]. After the first discovery of Raman scattering [148], it was quickly realized that the Raman spectra contains a unique signature from the molecular vibration that can be used to identify the unknown molecules [149]. It also found its use in the supercontinuum generation [150] which is another field of research with numerous applications associated with it.

The focus of this chapter is another inelastic scattering process called Brillouin scattering [147, 151]. First discovered by Leon Brillouin in 1922 [152] and independently by Leonid Mandelstam in 1926 [153], Brillouin scattering is a process originating from the propagating pressure wave (acoustic phonon[2]). In optical communication systems, the light scattering in the low-loss optical fiber is detrimental impeding the transfer of optical signals over long distances [154, 155, 156]. However, there are many applications that use Brillouin scattering to an advantage. As oppose to Raman scattering,

[1]Raman scattering is governed by THz frequency vibration mode which correlates with the optical frequency giving the name optical phonon mode.

[2]Brillouin scattering is mediated by relatively low frequency phonon mode with MHz to GHz frequency.

Brillouin scattering is governed by the bulk modulus and carries information about the material strain which are often used to create a strain or temperature map along the optical fiber [157, 158, 159]. Also, Brillouin scattering based bio-sensors are breaking the limits of conventional sensors as the acoustic wave interacting with the surrounding medium detects changes in their physical properties while an optical output provides an increased sensitivity [77, 78, 93, 160]. In this case, Brillouin scattering is used as means to transform a mechanical domain problem to an optical domain for ease of detection and measurements. Recently, Brillouin scattering optomechanical interaction has found many new applications where the acoustic wave is exploited to manipulate the system's optical response. For example, Brillouin scattering with extremely high and narrowband Brillouin gain was used to make optical filters with high suppression ratio that is also both tunable and reconfigurable [161, 162, 163, 164]. Other applications of Brillouin scattering include amplifiers [165], generation of slow and fast light [166, 167], Brillouin cooling [100], and Brillouin laser [75, 168, 169, 170] just to name a few. And we shall add Brillouin scattering induced transparency [22], breaking reciprocity, and optical isolator [23] to the above list. First, to understand the physics of underlying optomechanical interaction and how Brillouin scattering is able to break the reciprocity in an optical system, we will review and derive equations that lead to the density changes necessary for any scattering process to occur.

4.2 Spontaneous Brillouin scattering

Spontaneous Brillouin scattering is a scattering of light from refractive index or dielectric permittivity perturbations that are caused by the thermal fluctuations of density and anisotropy [171, 172]. At any finite temperature, a lattice vibration is present in the system as described by the Bose-Einstein statistics which predict the phonon energy

$$E_{phonon} = \frac{\hbar\omega}{e^{\hbar\omega/kT} - 1} \tag{4.1}$$

where $\hbar$ is planck's constant, ω is the phonon frequency, k is the Boltzmann constant, and T is the absolute temperature. The low frequency lattice

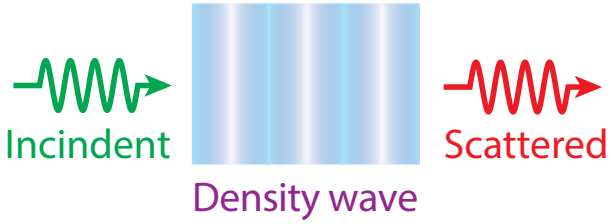

Figure 4.1: Spontaneous Brillouin scattering occurs due to the density wave that creates a refractive index perturbations within the medium. Such electrostriction effect is described by the eq. 4.4. The incident optical field can scatter The density wave originates from a thermal fluctuation as described by Bose-Einstein distribution (Eq. 4.1). When the incident optical field is small, the material property is not modified.

vibration, or the acoustic phonon, is also understood as a density wave which leads to the change in dielectric constant as

$$\Delta\epsilon = \left(\frac{\partial\epsilon}{\partial\rho}\right)_T \Delta\rho + \left(\frac{\partial\epsilon}{\partial T}\right)_\rho \Delta T \tag{4.2}$$

where ρ is the material density. Assuming dielectric constant is dominantly dependent on the material density, the above expression can be modified as

$$\langle\Delta\epsilon^2\rangle = \gamma_e^2 \frac{\langle\Delta\rho^2\rangle}{\rho_o^2} \tag{4.3}$$

where γ_e is the electrostriction coefficient defining the change in dielectric constant for a given change in density as

$$\gamma_e = \left(\rho\frac{\partial\epsilon}{\partial\rho}\right)_{\rho=\rho_o} \tag{4.4}$$

Using the Helmholtz free energy expression

$$A = U - TS \tag{4.5}$$

where U is the internal energy of the system, and S is the entropy, we can find [172]

$$\langle\Delta\rho^2\rangle = \frac{1}{V} CkT\rho^2 \tag{4.6}$$

where V is the scattering volume and C is the material compressibility defined as

$$C = -\frac{1}{V}\left(\frac{\partial V}{\partial p}\right)_T \tag{4.7}$$

where p is the pressure. Then, we can further express the density change as a function of the material compressibility as

$$\frac{\langle \Delta\rho^2 \rangle}{\rho_o^2} = \frac{kTC}{\Delta V} \tag{4.8}$$

This expression shows that the material with a given compressibility C will experience a density fluctuation, or an excitation of an acoustic wave $\langle \Delta\rho^2 \rangle / \rho_o^2$, from the thermal energy that is proportional to the ambient temperature T. And the refractive index and material density has a linear relationship for a wide range of wavelength which can be found experimentally [173].

This density fluctuation, however, is quite small at any practical temperatures and the spontaneous light scattering process originating from the thermal fluctuations is also quite weak. In this case, the light scattering creates a negligible change in the property of optical medium.

4.3 Stimulated Brillouin scattering

On the other hand when sufficient optical power is provided at the medium, the spatio-temporal beat of the incident (input) and scattered optical fields can create a periodic variation in refractive index through a process called electrostriction. The electrostriction is a property available in dielectric materials that changes its material density when the electric field is applied. In turn, the incident light experiences more density fluctuations amplifying the light scattering process i.e. stimulated Brillouin scattering.

4.3.1 Electrostriction

As described in Ch. 4.2, the Brillouin scattering is mediated by electrostriction. Electrostriction is a property of a dielectric material to become more

dense under electromagnetic field. Such phenomenon rises from the material movement in a molecular level to minimize the potential energy of the system. The molecules are drawn into the region of higher electromagnetic field intensity. The electrostrictive strain $\mathbf{S}_{ij}$ is related to the electric field $\mathbf{E}_k$ and $\mathbf{E}_l$ with electrostriction coefficient $\boldsymbol{\gamma}_{ijkl}$ as

$$\mathbf{S}_{ij} = \boldsymbol{\gamma}_{ijkl}\mathbf{E}_k\mathbf{E}_l \tag{4.9}$$

where γ_{ijkl} is the electrostriction coefficient of fourth rank tensor. And the change in potential energy Δu from the polarization of molecules is given by [171]

$$\Delta u = \frac{1}{2}\epsilon\Delta\epsilon\left|\mathbf{E}\right|^2 \tag{4.10}$$

where ϵ is dielectric constant. Since the material density ρ is related to the dielectric constant ϵ as

$$\Delta\epsilon = \frac{\partial\epsilon}{\partial\rho}\Delta\rho \tag{4.11}$$

we can solve for the change in material density $\Delta\rho$ for a given applied electric field $\mathbf{E}$ as

$$\Delta\rho = \frac{1}{2}\epsilon_o\rho C\gamma_e\mathbf{E}^2 \tag{4.12}$$

where ϵ_o is vacuum permittivity and C is material compressibility defining material density change for a given pressure change and is expressed as

$$C = \frac{1}{\rho}\frac{\partial\rho}{\partial p} \tag{4.13}$$

Note, that compressibility can be defined using either the material density ρ or volume V by the relationship

$$-\rho\frac{\partial\epsilon}{\partial\rho} = V\frac{\partial\epsilon}{\partial V} \tag{4.14}$$

Thus, the applied electric field E induces elastic strain within the material causing deformation and change in density.

Due to the rate associated with molecular movement, the electromagnetic

fields of THz frequency only creates a static change in bulk density. In Brillouin scattering, however, the beating of Stokes and anti-Stokes electromagnetic fields induces a local change in material density which we understand as a propagating acoustic wave.

4.4 Phase matching requirement

The conservation of mass, energy and momentum are three most fundamental conservation laws found in physics. Although photon is massless, the conservation of energy and momentum still applies to the Brillouin light scattering process. Brillouin light scattering induces a frequency shift due to the associated acoustic phonon mode and energy conservation requirement. From the Planck-Einstein relation, the photon energy is simply $E = \hbar\omega$ where ω is the optical frequency. Thus, phonon energy is destroyed and photon energy is created in the form of Stokes frequency shift conserving the net energy in the system. Similarly, the momentum conservation requirement is also satisfied via momentum exchange between phonon and photon modes within the system. Therefore, both energy conservation (Eq. 4.16) and momentum conservation (Eq. 4.15) requirements must be satisfied for Brillouin scattering processes to take place (i.e. phase matching). This relationship is expressed as

$$\vec{k}_2 - \vec{k}_1 = \vec{q}_B \tag{4.15}$$

$$\omega_2 - \omega_1 = \Omega_B \tag{4.16}$$

where k_i represents momentum vector associated with optical modes, q_B represents the associated phonon mode mediating Brillouin coupling between the two optical modes, ω_i represents optical frequency and Ω_B represents acoustic frequency (phonon mode frequency).

This phase matching relationship is often represented graphically using a dispersion diagram. In Figure. 4.2, we show two special cases of Brillouin scattering. In a back-scattering SBS system, the optical fields propagate in opposite directions. Since the frequencies, ω_1 and ω_2, are nearly identical, the optical momentum vectors, $\vec{k}_1$ and $\vec{k}_2$, are also nearly identical, but have opposite signs (propagating in the opposite direction). Thus, acoustic mo-

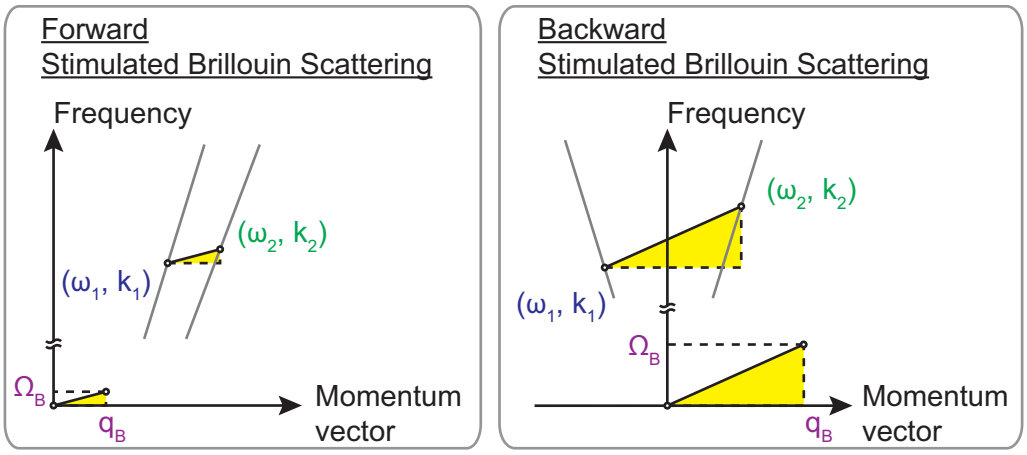

Figure 4.2: Dispersion diagrams. When the control laser is parked at high frequency optical mode, (ω_2, k_2), Stokes scattered light is generated at low frequency optical mode, (ω_1, k_1). For Stokes scattering, the frequencies and wave vectors of the two optical modes and an intermediate acoustic mode must satisfy the condition, $k_2 - k_1 = q_B$ and $\omega_2 - \omega_1 = \Omega_B$. (left) Forward-SBS system. (right) Backward-SBS system.

mentum vector, $\vec{q}_B$, is about double the length of the optical momentum vector to satisfy Eq. 4.15 and 4.16 as shown in 4.2b. This implies the generation of acoustic waves in the tens of GHz frequency regime, depending on the laser frequency, ω, refractive index, n, and speed of sound in the material, v (Eq. 4.17) [171]. In case of silicon dioxide excited with a 193 THz (1550 nm) laser, the Brillouin frequency is 11 GHz ($v = 5700$ m/s, $n = 1.5$).

$$\Omega_B = \frac{2v}{c/n}\omega \tag{4.17}$$

In a forward-SBS system, the momentum vectors of the incident and scattered light are nearly identical with the same sign (propagating in the same direction) as shown in Fig. 4.2a. Hence, the acoustic momentum vector is very small and the frequency is typically in a sub-GHz (Eq. 4.18).

$$\vec{q}_B = \frac{\Omega_B}{\vec{v}} \tag{4.18}$$

At such low frequency, the phonon lifetimes are significantly longer than that of the acoustic mode from back-scattering.

4.5 Acousto-optic interaction

As mentioned earlier, Brillouin scattering is a scattering process involving acousto-optic interaction. Thus, we derive the system of coupled equation that describes acoustic field $\mathbf{u}$ and optical fields $\mathbf{E}$ from acoustic wave equation and electromagnetic wave equation.

The electromagnetic wave equation is written as

$$\nabla^2\mathbf{E} - \frac{\epsilon}{c^2}\frac{\partial^2\mathbf{E}}{\partial t^2} = \frac{4\pi}{c^2}\frac{\partial^2\Delta\mathbf{P}}{\partial t^2} \tag{4.19}$$

where ϵ is dielectric permittivity, c is speed of light, and $\Delta\mathbf{P}$ is change in polarization given by

$$\Delta\mathbf{P} = -\frac{\gamma_e}{4\pi}\left(\nabla\cdot\mathbf{u}\right)\mathbf{E} \tag{4.20}$$

Here, γ_e is the electrostrictive constant defined as

$$\gamma_e = \rho\frac{\partial\epsilon}{\partial\rho} \tag{4.21}$$

In Brillouin scattering, electrostrictive constant is an essential source term that gives rise to the excitation of electromagnetic wave in electromagnetic wave equation. In other words, electrostriction creates dielectric permittivity fluctuation from the sound wave.

Similar to the electromagnetic wave equation, the wave equation describing acoustic wave can be written as

$$\nabla^2\mathbf{u} - \frac{1}{c_s^2}\frac{\partial^2\mathbf{u}}{\partial t^2} = \mathbf{f} \tag{4.22}$$

with complex field amplitude $\mathbf{u}$, external source $\mathbf{f}$, and sound speed c_s. Substituting the external source with electrostrictive force $\frac{1}{2}\Delta\mathbf{P}\cdot\mathbf{E}$ using eq. 4.20,

$$\nabla^2\mathbf{u} - \frac{1}{c_s^2}\frac{\partial^2\mathbf{u}}{\partial t^2} = -\frac{\gamma_e}{8\pi}\left(\nabla\cdot\mathbf{u}\right)\mathbf{E}^2 \tag{4.23}$$

Applying the electromagnetic field equation $\mathbf{E}_i = \boldsymbol{\phi}_i a_i e^{-i\omega_i t}$ (i=1, 2 corresponds to the two optical modes) and acoustic field equation $\mathbf{u} = \boldsymbol{\psi} u e^{-i\omega_B t}$ with spatial mode functions $\boldsymbol{\phi}_i$ and $\boldsymbol{\psi}$ respectively,

Solving for the electromagnetic and acoustic field with spatial mode func-

tions $\boldsymbol{\phi}_i$ and $\boldsymbol{\psi}$ respectively, the system of rate equations describing the coupled electromagnetic and acoustic waves can be found as shown below.

$$\frac{\partial a_1}{\partial t} = -\frac{\kappa_1}{2}a_1 - i\Delta_1 a_1 - i\beta^* u^* a_2 e^{-i\delta t} \tag{4.24}$$

$$\frac{\partial a_2}{\partial t} = -\frac{\kappa_2}{2}a_2 - i\Delta_2 a_2 - i\beta u a_1 e^{i\delta t} \tag{4.25}$$

$$\frac{\partial u}{\partial t} = -\frac{\Gamma_B}{2}u - i\Delta_B u - i\beta^* a_1^* a_2 e^{-i\delta t} \tag{4.26}$$

where a_1 and a_2 are Stokes and anti-Stokes electromagnetic fields respectively, and u is acoustic field with the associated optical and acoustic loss rates κ_1, κ_2, and Γ_B respectively. Δ_i is the frequency detuning from the resonance frequency (i=1, 2, B corresponds to Stokes optical mode, anti-Stokes optical mode, and acoustic mode respectively) and β is the optomechanical coupling term.

$$\beta = \frac{\gamma_e \sqrt{\omega_1 \omega_2}}{2\epsilon} \int (\boldsymbol{\phi_1} \cdot \boldsymbol{\phi_2}) (\nabla \cdot \boldsymbol{\psi}) \, d^3\boldsymbol{r} \tag{4.27}$$

When Brillouin phase matching requirement discussed in the previous section is satisfied, an optomechanical interaction and intermodal energy exchange take place. The strength of this interaction is defined by the optomechanical coupling coefficient which is proportional to the optical or acoustic source field amplitude and the spatial overlap of optical and acoustic waves.

4.6 Nonreciprocity using Brillouin scattering

The main focus of this thesis is to explore nonreciprocity via Brillouin scattering induced transparency. However before we present our contribution, we shall discuss how others have used Brillouin scattering to show nonreciprocity in different systems as such notion has been suggested previously.

The first experimental demonstration of nonreciprocal light transmission using Brillouin scattering was shown by Kang et. al. in 2011 [15]. Their photonic crystal fiber system has proved that Brillouin scattering is unidirectional when the acoustic wave is available in a single direction due to the phase matching condition or lack thereof. The principle of operation is most

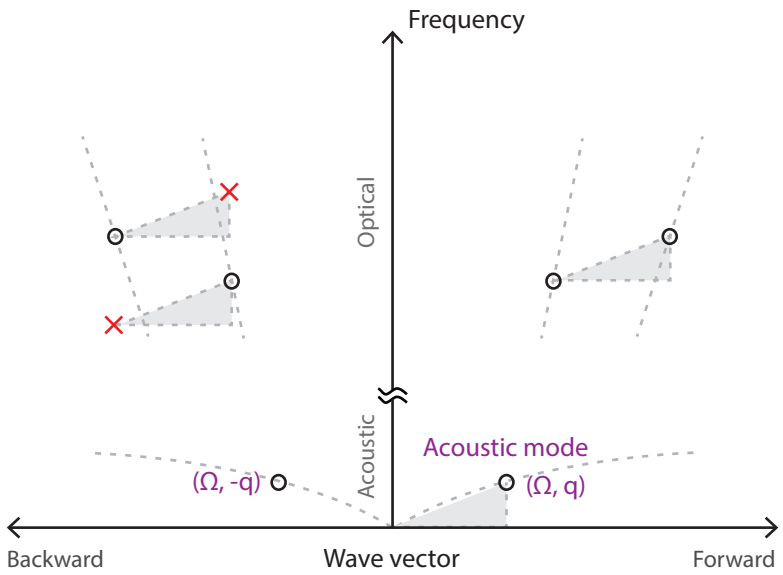

Figure 4.3: Dispersion diagram revealing nonreciprocal interband transitions. The scattering is allowed in the forward direction whereas the scattering between backward propagating optical modes are forbidden due to the lack of phase matching.

clearly illustrated using an omega-K diagram that shows backward propagation direction (Fig. 4.3). The phase matching is satisfied in the forward direction with the forward propagating acoustic mode. However, Brillouin scattering is forbidden between the two backward propagating optical modes because the necessary acoustic mode is not available. Others have suggested and designed more efficient mode of operation to improve upon the fiber system [174, 175, 176, 177], but the nonreciprocity in Brillouin scattering system always originates from the phase matching condition. As we will discuss in Ch. 7, we also rely on the phase matching condition to demonstrate nonreciprocal Brillouin scattering induced transparency.

4.7 Difference between radiation pressure driven optomechanics and Brillouin scattering

Optomechanics is a multi-physics field of study that explores the interaction between electromagnetic radiation (opto-) and mechanical vibration (mechanics). In a broad sense, Brillouin scattering, a photo-elastic scattering of light mediated by an acoustic wave, falls under the category of optomechan-

ics. However, we must distinguish Brillouin scattering from optomechanical effects driven by radiation pressure breathing modes. Thus, we present several key distinctions that must be pointed out for understanding Brillouin scattering induced transparency.

The breathing mode in a microsphere resonator (Fig. 3.3a.) can be considered as a balloon expanding and contracting in size periodically. In other words, the mechanical displacement takes place ubiquitously in the microsphere. As the optomechanical coupling is a function of the optical and mechanical modal overlap (Eq. 4.27), one may think this guarantees the observation of optomechanical effects. However, the surface acoustic wave modes used in Brillouin scattering reside near the outer edge of the resonator and are able to achieve much better coupling rate because any useful optical modes that is accessible via evanescent coupling and has a good quality factor occupies the same spatial location as shown in Fig. 3.5. In fact, a lot of effort is spent on engineering the optical and mechanical confinement within a small region to enhance Brillouin gain [76] and to achieve better cooperativity[3] [99].

Furthermore, the geometry of breathing mode also contributes to the phase matching requirement. The breathing mode is a standing wave with zero momentum and thus, does not participate in momentum exchange in the scattering process. On the other hand, Brillouin scattering is mediated by acoustic phonon with coherent movement of lattices and a non-zero momentum vector. Thus, the phase matching condition (discussed in Ch. 4.4) requires both energy and momentum conservation to be satisfied in the scattering process which imposes an additional constraint for the observation of Brillouin scattering induced transparency. We will show that we can exploit this constraint to our advantage in demonstrating nonreciprocal light transmission (Ch. 7).

4.7.1 Comment on optomechanically induced transparency

Optomechanically induced transparency (OMIT) is an EIT analogue demonstrated using radiation pressure breathing mode microsphere [101] and pho-

[3]Cooperativity is expressed as $C = 4g_o^2/\kappa\Gamma$ where g_o is the optomechanical coupling, κ is optical loss rate, and Γ is the mechanical loss rate. It is a characteristic parameter determining the relative optomechanical coupling in a system. $C >> 1$ is necessary for achieving the strong coupling regime which is relevant in many quantum mechanics and electrodynamics experiments.

tonic crystal [103]. As alluded to in this section, the key difference between OMIT and Brillouin scattering induced transparency (BSIT) is the use of standing wave breathing mode as oppose to the traveling surface acoustic wave mode. At the time of first experimental demonstration of BSIT, it was believed only BSIT was capable of showing the nonreciprocity due to the specific phase matching condition. However, it was later experimentally shown that OMIT can also break the reciprocity because the optical modes only couple to the copropagating modes within the resonator [11]. This can also be seen from the Hamiltonian description of the two systems. Essentially, the device responses are identical because the Hamiltonians for OMIT [11, 101, 103, 178] and BSIT are identical (See Appendix B).

CHAPTER 5

INDUCED TRANSPARENCY USING BRILLOUIN SCATTERING

5.1 Introduction

Electromagnetically induced transparency (EIT) provides a powerful mechanism for controlling light propagation in a dielectric medium, and for producing slow and fast light. EIT traditionally arises from destructive interference induced by a non-radiative coherence in an atomic system. Stimulated Brillouin scattering (SBS) of light from propagating hypersonic acoustic waves has also been used successfully for the generation of slow and fast light. However, EIT-type processes based on SBS were considered infeasible because of the short coherence lifetime of hypersonic phonons. In this chapter, we report a new Brillouin scattering induced transparency (BSIT) phenomenon generated by acousto-optic interaction of light with long-lived propagating phonons in a silica resonator. We demonstrate that BSIT is uniquely non-reciprocal due to the propagating acoustic wave and accompanying momentum conservation requirement. We also show that BSIT enables ultralow-power ultralow-footprint slow light generation with delay-bandwidth comparable to state-of-the-art SBS systems.

5.2 Review of electromagnetically induced transparency

Electromagnetically induced transparency (EIT) was theorized in 1989 by Imamoğlu and Harris while exploring ways to enhance higher order non-linear

Work presented in this chapter has been published in: "Non-reciprocal Brillouin scattering induced transparency", Nature Physics, vol. 11, p. 275, 2015.

susceptibility without a large resonant absorption [179, 180]. And in 1991, the experimental demonstration of EIT was shown as soon as the suitable energy level structure was found from strontium [19]. Since then, the study of electromagnetically induced transparency [21,181,182,183] and analogous effects in other physics [10, 22, 101, 102, 103, 184, 185, 186, 187] quickly took off while exploring their applications as well. Induced transparency is extensively used for the generation of slow and fast light which will be discussed in the next chapter [10, 22, 181, 182, 188, 189]. Not only that, there are many other applications of EIT that use angular dependence of probe and control laser creating EIT effect to measure atomic velocity [190,191], and energy and momentum conservation to show efficient frequency conversion [192,193,194].

Electromagnetically induced transparency (EIT) is a process that inhibits the absorption of electromagnetic field within an atomic transition through an interference effect. Typically, an electromagnetic field tuned to an absorption line will be absorbed to the material and excite an electron to the higher state. In EIT, a strong electromagnetic field (control laser) is set to a frequency matching the transition from an intermediate state to the excited state (|2>-|3> transition from Fig. 5.2a). In effect, the control laser enables an indirect transition pathway for a weak electromagnetic field (probe laser). Then, the destructive interference of the direct and indirect transition pathways takes place and is observed as an induced transparency (Fig. 5.1b). Here, it is important to note that the two energy levels must be coherently

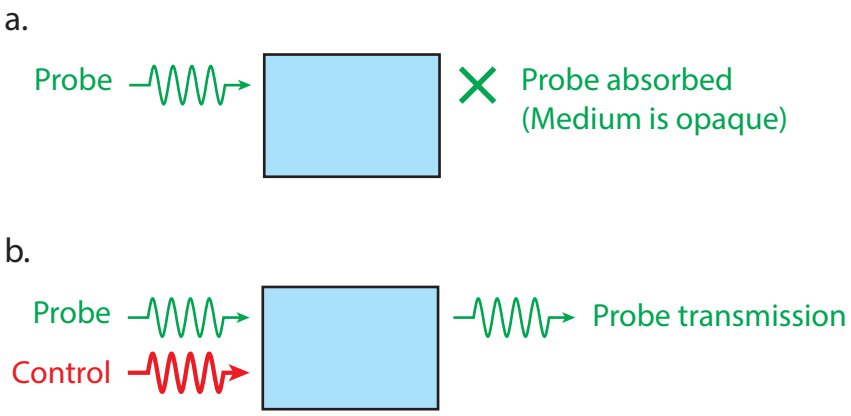

Figure 5.1: **a.** Probe signal is absorbed without the control laser. In other words, the medium is opaque at the probe frequency. **b.** Probe at the absorption frequency is allowed to transmit through the medium when the control laser creates two transition pathways for the probe.

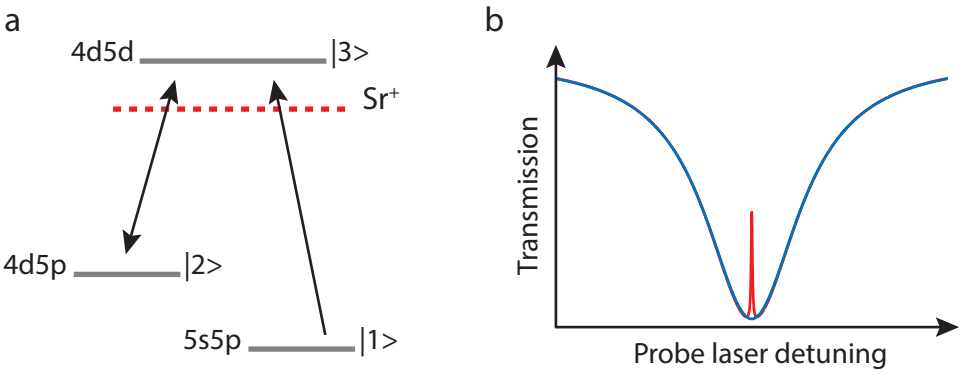

Figure 5.2: **a.** Lambda type energy level diagram of strontium. **b.** (Blue) Probe transmission showing an absorption line without EIT. (Red) In the presence of the control laser, induced transparency is observed within the absorption line.

coupled with sufficient coupling rate (Rabi frequency) for the noticeable effect in the absorption line.

The first experimental demonstration of EIT was shown by Boller et. al. in an absorption line of strontium [19]. In the energy level diagram of strontium (Fig. 5.2a), a lambda type system with energy levels and transition pathways suitable for interference is shown. In the presence of the strong control laser tuned to |2>-|3> transition, the direct probe transition |1>-|3> and the indirect probe transition |1>-|3>-|2>-|3> have opposite signs of probability amplitude and thus destructively interfere. An illustration of probe transmission signal is shown in Fig. 5.2b.

Also, an alternate description of EIT can be drawn by introducing the dressed state. As oppose to the control laser enabling an interference pathway for the probe beam, we can consider the control laser as splitting the energy level directly with the associated dipole moment μ i.e. dressing the state (Fig. 5.3a). The energy level splitting is governed by AC Stark effect and is expressed as

$$\Omega_R = \frac{\mu \mathbf{E}}{\hbar} \tag{5.1}$$

In a way, the electric field supplied by the control laser is dressing the energy level $|3>$ effectively creating two resonances. Now, probing around the energy level transition |2>-|3>, we observe two new dressed states appear (Fig. 5.3b). The dressed states are shifted in frequency with an opposite sign

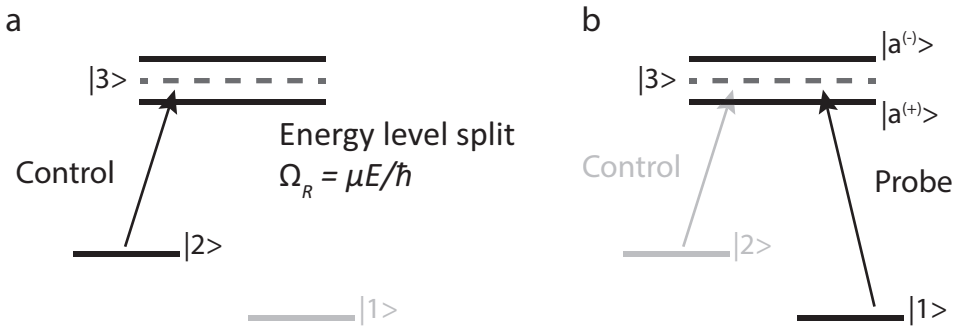

Figure 5.3: **a.** Lambda type energy level diagram of strontium. **b.** (Blue) Probe transmission showing an absorption line without EIT. (Red) In the presence of the control laser, induced transparency is observed within the absorption line.

of detuning ($\omega \pm \mu E/2\hbar$) which leads to the cancellation of susceptibility. Ultimately, the probe is inhibited from absorption which we observe as the induced transparency.

5.2.1 Induced transparency in other systems

Since the first demonstration of induced transparency in 1991 [19], there have been several successful attempts to emulate analogous phenomenon in other systems. Zhang et. al. theoretically suggested induced transparency in plasmonic system [186] and Liu et. al. carried out the experiment [187]. In this plasmonic system, two non-radiative modes coupled with a superradiant mode form an EIT-like resonance with a narrow region of destructive interference. Smith et. al. demonstrated induced transparency using two coupled resonators [185]. In the coupled resonator system, the light traveling within only one resonator and the light that traveled through the second resonator are allowed to destructively interfere as the phase shift is introduced from the light coupling to another resonator. Weis et. al. demonstrated optomechanically induced transparency using an optical microcavity [101] and Safavi-Naeini et. al. using optomechanical crystal nanocavity [103]. In both optomechanical analogue of EIT, the two optical fields are coupled through an acoustic excitation and annihilation. This acoustic excitation and annihilation process creates a second transition pathway similar to the indirect transition pathway of EIT.

5.3 Theoretical description of Brillouin scattering induced transparency

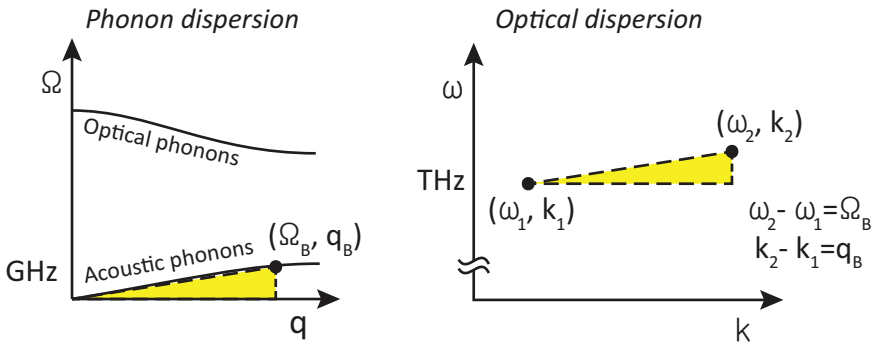

Figure 5.4: Brillouin phase matching requires two optical modes of a system that are separated by the acoustic parameters in ω-k space.

With a necessary background on Brillouin scattering and EIT, the theoretical description and experimental result of Brillouin scattering induced transparency (BSIT) is presented in this section. Just like EIT, BSIT is observed as a small window of inhibited absorption within an optical resonance. The key difference is that the phase matched set of optical and acoustic modes of a resonator is used instead of an atomic excitation.

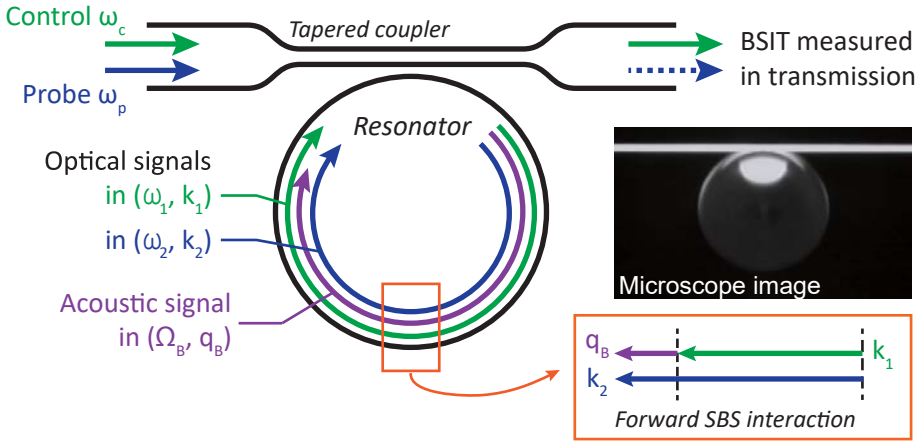

Figure 5.5: In a BSIT experiment, control and probe lasers are coupled to phase matched optical whispering gallery modes of a resonator by means of a tapered optical fiber. A forward-SBS opto-acoustic interaction takes place within the resonator.

Nonlinear optical processes such as EIT need to satisfy the energy-momentum

conservation, leading to the phase-matching requirement. For EIT in an atomic system, the momentum of the spin wave is set by the relevant optical waves, automatically satisfying the phase matching requirement [19,20,183]. In comparison, the traveling acoustic wave in BSIT carries a momentum that is intrinsic to the mechanical medium, is discretized by the resonator, and can far exceed the momentum of an optical wave, which leads to special phase matching requirement as will be discussed in detail below. More importantly, this momentum requirement of Brillouin processes makes BSIT intrinsically non-reciprocal, as known from SBS [15,174,175]. The BSIT that we describe here vanishes when either the probe or the control reverses its propagation direction (see Fig. 7.9). Such non-reciprocity can be exploited for important applications, including on-chip optical isolators, circulators, and gyroscopes.

5.3.1 Analytical description of Brillouin scattering induced transparency

For the analytical description of Brillouin scattering induced transparency (BSIT), the mathematical formalism established by Agarwal and Jha is adopted [195]. The intracavity fields representing the pump/control laser, anti-Stokes shifted probe, and acoustic displacement can be described using the following three coupled rate equations.

$$\begin{aligned} \dot{a_1} &= -\frac{\kappa_1}{2}a_1 - i\Delta_1 a_1 - i\beta^* u^* a_2 e^{-i\delta t} \\ \dot{a_2} &= -\frac{\kappa_2}{2}a_2 - i\Delta_2 a_2 - i\beta u a_1 e^{i\delta t} \\ \dot{u} &= -\frac{\Gamma_B}{2}u - i\Delta_B u - i\beta^* a_1^* a_2 e^{-i\delta t} \end{aligned} \tag{5.2}$$

$$\begin{aligned} \delta &= \omega_2 - \omega_1 - \Omega_B \\ \Delta_1 &= \omega_1 - \omega_c \\ \Delta_2 &= \omega_2 - \omega_p \\ \Delta_B &= \Omega_B - (\omega_p - \omega_c) \end{aligned} \tag{5.3}$$

where a_1, a_2, and u are the slowly varying phasor amplitudes of intracavity control field, scattered light field and mechanical displacement respectively, κ_1 and κ_2 are optical loss rates of pump mode and anti-Stokes mode respectively, Γ_B is acoustic loss rate, and β is the coupling coefficient accounting

for modal overlap and Brillouin gain in the material. The frequencies ω_1, ω_2, and Ω_B represent the pump optical resonance, anti-Stokes optical resonance, Brillouin acoustic resonance, while ω_c, and ω_p represent the control laser field and probe laser field respectively. δ, Δ_1, Δ_2, and Δ_B are the pump mode to anti-Stokes mode detuning from the acoustic mode, pump mode detuning from the control laser, anti-Stokes mode detuning from the probe laser, and the modulation frequency detuning from the acoustic mode respectively.

Details on the evaluation of detuning parameters and the coupling parameter β are provided in [195]. For phase matching, the frequency relationship $\omega_2 = \omega_1 + \Omega_B$ must be satisfied. Momentum matching is implicit in the complex phasors that represent the fields.

For the induced transparency experiment, the system at steady state is analyzed, thus setting all derivatives to zero. Additional intracavity control field f_c and probe field f_p terms are added on the right-hand-side as shown in eqns. 5.4. For further simplification, the optical loss rates κ_1 and κ_2 are assumed nearly identical (new symbol κ). Finally, the non-depleted pump field approximation eliminates the coupling term from the first equation. Then, the following simplified system can be obtained.

$$\begin{aligned} 0 &= -\gamma_1 a_1 + f_c \\ 0 &= -\gamma_2 a_2 - i\beta u a_1 e^{i\delta t} + f_p \\ 0 &= -\gamma_B u - i\beta^* a_1^* a_2 e^{-i\delta t} \end{aligned} \tag{5.4}$$

where

$$\begin{aligned} \gamma_1 &= \kappa/2 + i\Delta_1 \\ \gamma_2 &= \kappa/2 + i\Delta_2 \\ \gamma_B &= \Gamma_B/2 + i\Delta_B \end{aligned} \tag{5.5}$$

The system of equations Eq. 5.4 can then be solved to produce the steady state amplitudes of the fields:

$$a_1 = \frac{f_c}{\gamma_1} \tag{5.6}$$

$$a_2 = \frac{f_p \gamma_B}{\gamma_2 \gamma_B + |\beta|^2 |a_1|^2} \tag{5.7}$$

$$u = \frac{-i\beta^* a_1^* a_2 e^{-i\delta t}}{\gamma_B} \tag{5.8}$$

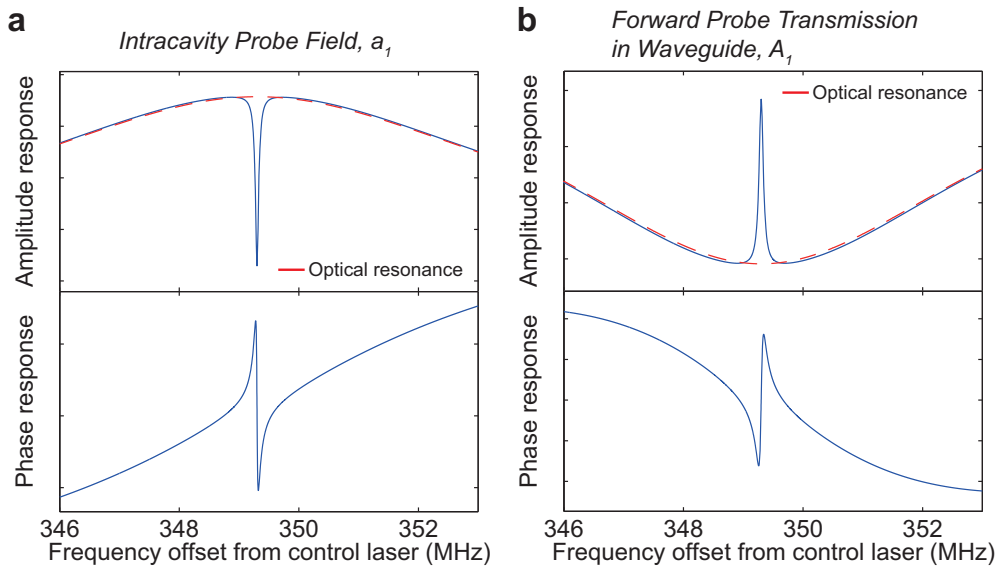

Figure 5.6: **Theoretical prediction of amplitude and phase responses for induced transparency. a.** Probe field when measured inside the cavity. **b.** Probe field transmitted and measured at the photodetector. The phase response of intracavity probe field is inverted as the light evanescently couples back to the waveguide and mix with the part of probe field that was reflected from the cavity.

The control laser (Eq. 5.6) excites the system, while the probe laser, described by Eq. 5.7, sweeps through the anti-Stokes optical mode of interest and experiences the induced transparency. The intracavity probe field transfer function is illustrated in Fig. 5.6a.

Here, it can be seen that the excitation of the ω_2 mode is minimized in the case of large Brillouin coupling β, large control field a_1, and small acoustic loss rate Γ_B. The achievable contrast is $\left(1 + \kappa\Gamma_B \,/\, (|\beta|^2|a_1|^2)\right)^{-1}$, which reaches 1 for very strong coupling. For a chosen acoustic mode having loss rate Γ_B it is important to have a comparable or larger optical loss rate κ for a window of transparency to be seen within the optical absorption. When $\kappa < \Gamma_B$, which is generally the case in back-scattering SBS experiments [147, 151, 171, 196], the effect will be decreased optical absorption with poor contrast. For instance in silica resonators pumped with 1550 nm light, $\kappa \approx 1$ MHz while $\Gamma_B \approx 10$ MHz. In the forward scattering experiments we describe here $\kappa \approx 1$ MHz while $\Gamma_B \approx 10$ kHz.

Note that the phase response of the probe within the cavity is in agreement with the results from previous SBS demonstrations, that is to say an anti-

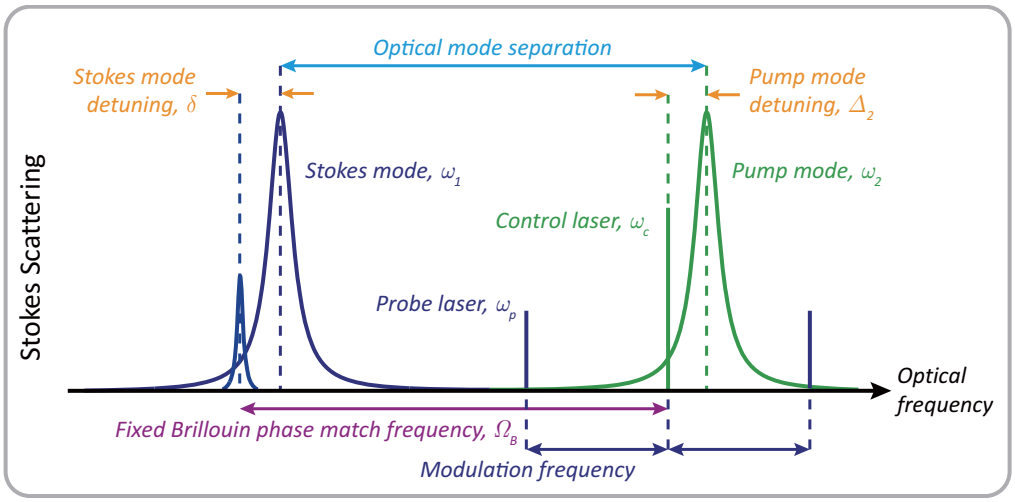

Figure 5.7: Optical frequency relationship of the coupled triplet system for absorption experiment using Stokes scattering. Opposite to anti-Stokes scattering case, the role of the pump and scattered modes is switched. Also, the probe laser sweeps in the opposite direction from higher to lower frequency.

Stokes probe experiences a fast light response. However, the opposite result (slow light) is observed when monitoring the probe field in the waveguide ($A_2 = RF_p + iTa_2$). Here, the input probe laser field is related to input intracavity field as $F_p = -if_p/T$ [95], while R and T are the reflection and transmission coefficients at the coupler. As shown in Fig. 5.6b, a slow light behavior is observed for the probe when measured in the waveguide.

5.3.2 Analytical description of Brillouin scattering induced absorption

To understand Brillouin scattering induced absorption, the process with a Stokes probe must be considered. Here, the same set of equations used for induced transparency is employed (Eq. 5.2), except that the roles of the control and probe lasers are reversed. In other words, subscript 1 refers to the Stokes probe while subscript 2 refers to the control field. Then, the

simplified system equations can be written as:

$$\begin{aligned} 0 &= -\frac{\gamma_1}{2}a_1 - i\beta^* u^* a_2 e^{-i\delta t} + f_p \\ 0 &= -\frac{\gamma_2}{2}a_2 + f_c \\ 0 &= -\frac{\gamma_B}{2}u - i\beta^* a_1^* a_2 e^{-i\delta t} \end{aligned} \tag{5.9}$$

where

$$\begin{aligned} \gamma_1 &= \kappa/2 + i\Delta_1 \\ \gamma_2 &= \kappa/2 + i\Delta_2 \\ \gamma_B &= \Gamma_B/2 + i\Delta_B \end{aligned} \tag{5.10}$$

The frequency matching relationship between the fields is unchanged i.e. $\omega_2 = \omega_1 + \Omega_B$. However, as illustrated in Fig. 5.7, the detuning parameters are modified on account of the interchanged control and probe designations.

$$\begin{aligned} \Delta_1 &= \omega_1 - \omega_p \\ \Delta_2 &= \omega_2 - \omega_c \\ \Delta_B &= \Omega_B - (\omega_c - \omega_p) \end{aligned} \tag{5.11}$$

Upon solving system of equations Eq. 5.9, the intracavity probe field is described as

$$a_1 = \frac{f_p \gamma_B^*}{\gamma_1 \gamma_B^* - |\beta|^2 |a_2|^2} \tag{5.12}$$

As before, the forward probe transmission in the waveguide A_1 is described as

$$A_1 = RF_p + iTa_1 \ . \tag{5.13}$$

Again, an inversion of phase response takes place when the probe field exits the resonator and mixes with the reflected input probe that did not couple to the resonator (Fig. 5.8).

5.3.3 Energy level analogy of Brillouin scattering

A 3-level lambda system analogy to EIT (Fig. 5.2a) can be made in the case of BSIT as shown in Fig. 5.9. Here, the optical mode (ω_1, k_1) is represented as

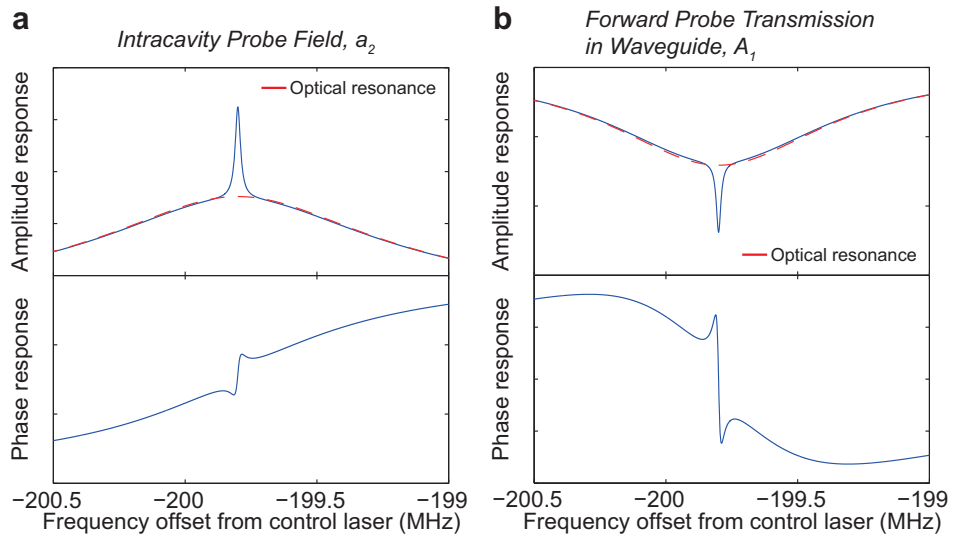

Figure 5.8: **Theoretical prediction of amplitude and phase responses for induced absorption. a.** Probe field when measured inside the cavity. **b.** Probe field transmitted and measured at the photodetector. The phase response of intracavity probe field is inverted as the light evanescently couples back to the waveguide and mix with the part of probe field that was reflected from the cavity.

an absorption transition |1>-|e>. For our BSIT experiment (Fig. 5.9a), the control laser is parked at the low frequency optical mode |2>-|e> while the probe laser is parked at the high frequency optical mode |1>-|e>. The separation of the two optical modes in a frequency space is defined by the acoustic frequency of Brillouin scattering, $\hbar\Omega_B$. Although light cannot directly scatter from |1> to |2> or vice versa, the two levels are coherently coupled via Brillouin scattering. With the coupling established, the probe transition through the direct path |1>-|e> interferes with the indirect transition path |1>-|e>-|2>-|e>. This interference results in the inhibited absorption.

Similarly, Stokes scattering is represented using energy level diagram in Fig. 5.9b. In this case, the constructive interference causes increased absorption into the optical mode as will be shown in Ch. 5.5.3.

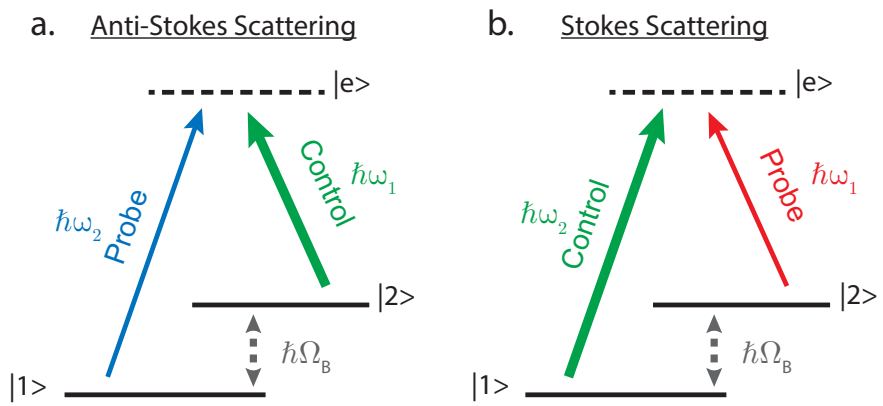

Figure 5.9: **Energy level analogy for Brillouin scattering systema.** Energy level with transition pathways for anti-Stokes scattering. Control laser is parked at the lower frequency transition |2>-|e> where |e> is a virtual level. **b.** Energy level with transition pathways for Stokes scattering. Control laser is now parked at higher frequency transition |1>-|e>.

5.3.4 Requirement for observation of Brillouin scattering induced transparency

The generation of BSIT requires a 3-mode system composed of two optical modes and one long-lived acoustic mode forming an aforementioned energy level analogue of EIT. Here, the long-lived acoustic mode allows sufficient coupling between the two optical modes before decoherence. Phase-matching of these modes in both frequency space and momentum space is essential as illustrated in Fig. 4.2. Notably, the momentum requirement is not needed for other transparency mechanisms [19, 20, 101, 102, 103]. As mentioned previously, in BSIT, the energies and momenta of these three modes must be matched to satisfy $\omega_2 - \omega_1 = \Omega_B$ and $k_2 - k_1 = q_B$ simultaneously. Here, (ω_1, k_1) are the energy and momentum of the lower energy optical mode, (ω_2, k_2) represent the higher energy optical mode, and (Ω_B, q_B) represent the acoustic mode. The coupling between the three modes is mediated by electrostrictive Brillouin scattering. Previous work has shown that such instances of both forward- and backward-SBS phase matching can occur naturally within a microresonator [100, 141, 197, 198].

Consider the situation where a strong laser pumps the lower energy optical mode (ω_1, k_1) while a weaker tunable probe measures the higher energy optical mode (ω_2, k_2) of the coupled system (Fig. 5.9a). When the

anti-Stokes probe signal is tuned to a resonator mode, it couples strongly to the resonator and generates a well understood opacity in the waveguide (Fig. 5.10,bottom) [95]. Further, in the presence of Brillouin phase match of the strong control laser and the anti-Stokes probe with a long lived phonon mode in the same medium, the probe is expected to undergo very strong resonant absorption into the control signal (Fig. 5.10,top) [199]. Intuitively, these two cascaded stages of absorption should lead to near-complete removal of the probe light from the system. As shown in this BSIT system, the intuition breaks down, and instead of strong absorption of the anti-Stokes probe, an interference is generated between the Stokes-directed absorption and anti-Stokes-directed scattering pathways. This results in a previously unforeseen transparency at the probe frequency $\omega_p = \omega_c + \Omega_B$ and the probe no longer couples into the resonator optical mode (Fig. 5.10).

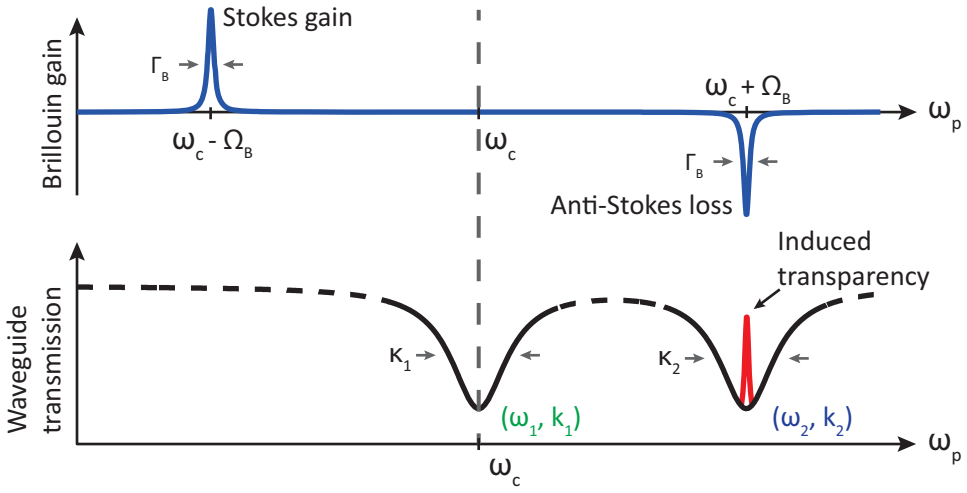

Figure 5.10: The control laser pumps the lower frequency optical mode to allow anti-Stokes scattering while the resonator suppresses Stokes scattering [197]. (Bottom) A probe laser scans through the optical resonances, visible as a drop in waveguide transmission [95]. (Top) From traditional SBS theory [171] anti-Stokes absorption is predicted for a probe signal at $\omega_p = \omega_c + \Omega_B$, which intuitively should increase the probe loss. However, when (Ω_B, q_B) represent a long lived phonon mode, a transparency is observed due to interference between Stokes and anti-Stokes scattering pathways.

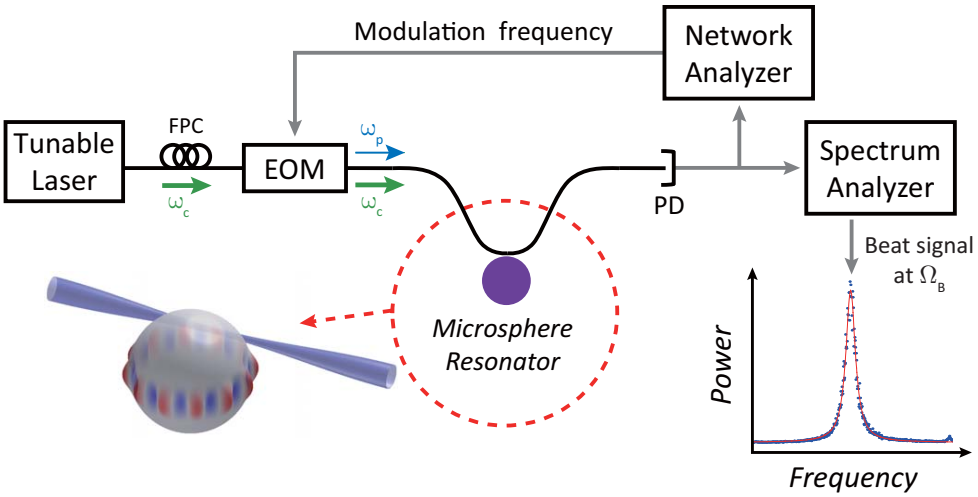

Figure 5.11: Experimental setup. Fiber coupled tunable diode laser sends the control laser signal through a tapered waveguide. Network analyzer provides probe frequency to the electro-optic modulator which creates a probe signal from the control laser. Photodetector (PD) monitors the signal transmission at the waveguide output and the electronic signal is analyzed using both network analyzer and electrical spectrum analyzer. FPC is fiber polarization controller.

5.4 Methodology

Fig. 5.11 shows the experimental setup used in this work. An ultra-high-Q silica microsphere resonator is evanescently coupled to a tapered silica fiber waveguide (Fig. 5.12), that provides coupling mechanism to the intracavity control and probe light fields. A tunable diode laser with a center wavelength of 1550 nm provides the control field to the pump mode, while the probe signal is generated using an electro-optic modulator (EOM). While the EOM creates two probe sidebands relative to the control laser, only one sideband is matched to the anti-Stokes optical mode of the device. The other (Stokes) sideband does not couple to the resonator and passes through the system unhindered at constant amplitude. The probe sideband spacing is determined by a modulation signal input to the EOM that is generated by a network analyzer. The transmitted optical signal at the output of the waveguide is received by a highspeed photodetector (Newport Model 1601), which results in an electronic output beat note between the control and probe optical signals. This electronic output is analyzed by an electrical spectrum analyzer (Tektronix RSA6120A) as well as the network analyzer (Agilent 4395A) for

probe transfer function analysis. When the higher energy optical mode is pumped above threshold (in the absence of a probe), the electronic beat note between the pump and scattered light generated on a photodetector can be used to distinguish the Brillouin scattering [197, 200] from radiation pressure induced optomechanical oscillation [201].

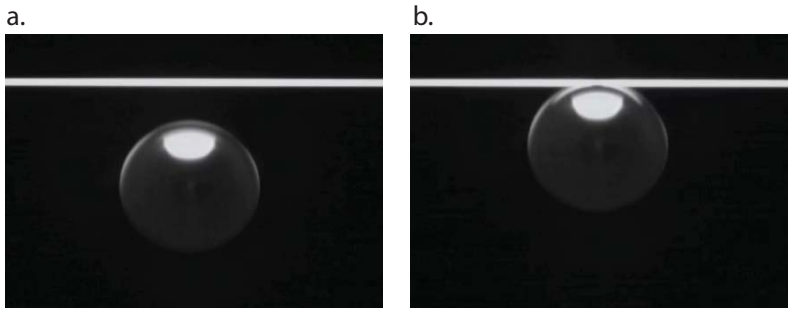

Figure 5.12: **Microscope images of resonator a.** Resonator is uncoupled from tapered fiber coupler. **b.** Resonator is coupled to tapered fiber coupler. The distance between the resonator and tapered fiber coupler can range between in-contact to tens of nm.

5.5 Experimental result

5.5.1 Verification of Brillouin phase matching

First task is to find a set of optical modes and an acoustic mode that fulfills the phase matching (Eq. 4.15 and 4.16) and allows the Brillouin scattering. Following the procedure from Ch. 5.4, the Brillouin phase matching is verified by the lack of harmonics from the beat note between the pump and scattered light. The beat notes generated from the two sets of optical fields used for induced transparency and absorption experiments are shown in Fig. 5.13.

5.5.2 Brillouin scattering induced transparency

When the optical and acoustic modes are identified, the induced transparency experiment is carried out as described in Ch. 5.4. First, the control laser is parked at the lower optical resonance and a probe signal on the higher resonance. Then, it leads to destructive interference for a probe signal and

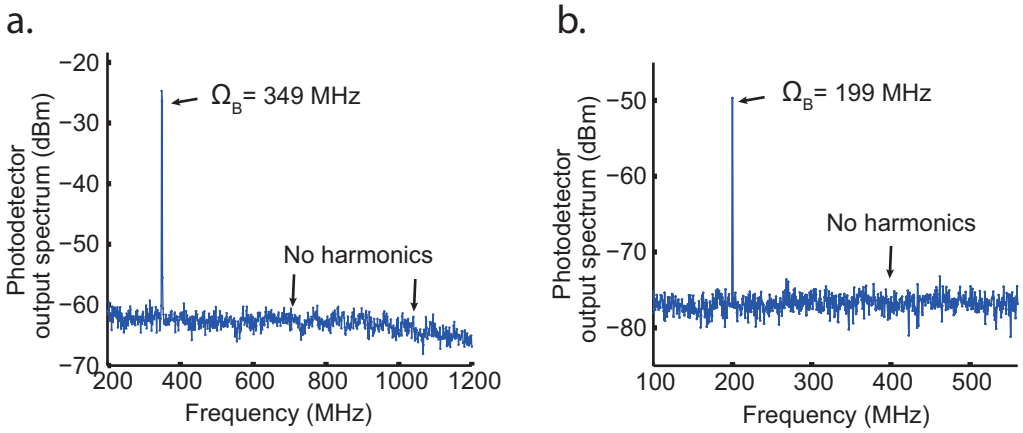

Figure 5.13: **Verification of Brillouin phase matching through Brillouin lasing. a.** When the (ω_2, k_2) mode is pumped with a strong laser source, a Stokes SBS laser is generated [200]. When the Stokes scattered and pump light are interfered on a photodetector, a beat note corresponding to their frequency difference, Ω_B, is measured. The lack of harmonics of Ω_B indicates that this is not a radiation pressure induced optomechanical oscillation. This is from induced transparency data. **b.** Brillouin lasing for induced absorption experiment (Ch. 5.5.3).

generates a transparency window (Fig. 5.14a). The measured amplitude response of the probe laser in Fig. 5.14a shows the relatively broad 4.4 MHz wide anti-Stokes optical mode with optical quality factor of 4.4×10^7. A very sharp transparency feature at 349.3 MHz offset from the control laser is observed in both amplitude and phase responses of the probe (Fig. 5.14). This 349.3 MHz frequency corresponds to a whispering-gallery acoustic wave mode [200] of the resonator with azimuthal mode number of 48 and phonon lifetime of 59.2 μs.

5.5.3 Brillouin scattering induced absorption

If the control optical signal is tuned to the higher energy optical resonance, it creates a region of greater opacity for a probe on the lower energy optical mode (Fig. 5.15a). Due to thermal effects on the optical resonance frequencies, it was technically more convenient to demonstrate opacity with a different forward-SBS triplet on the same resonator where Ω_B= 199.8 MHz (phonon lifetime of 56.2 μs). The amplitude response of the probe laser in Fig. 5.15a shows the 0.4 MHz wide Stokes optical mode with optical quality

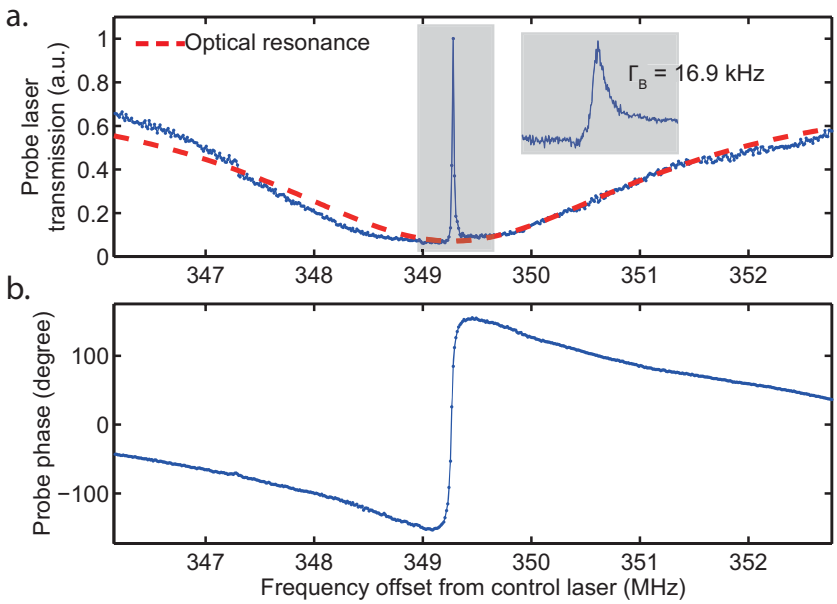

Figure 5.14: **Observation of BSIT a.** Transparency is observed for a probe on (ω_2, k_2) when a strong pump is placed at (ω_1, k_1). (Solid) Probe laser amplitude response. (Red-dashed) Curve fit to the (ω_2, k_2) optical mode. **b.** Probe phase response with distorted dispersion within the transparency.

factor of 4.9×10^8. An opacity with a 17.8 kHz linewidth is induced at 199.8 MHz offset from the pump.

5.5.4 Tuning optical mode

Although phase matching (Eq. 4.15 and 4.16) imposes strict constraints on the optical signal frequencies in the BSIT process, the transparency can be tuned by either slightly modifying the pump frequency within its optical mode, or thermally tuning the optical modes themselves (Fig. 5.16). The tuning of optical mode is also revealed from the Eq. 5.7 by modifying the detuning, $\omega_2 - \omega_1 - \Omega_B$ (Fig. 5.17). Furthermore, the transparency depth and width can be controlled [197, 202] through the control laser power. Such frequency tunability and the ability to switch the transparency on and off are desirable in several applications [174, 175].

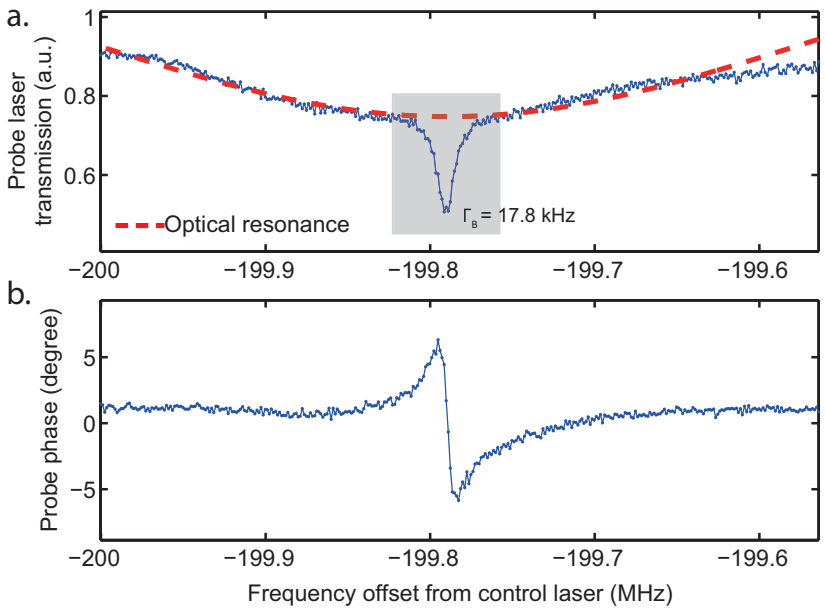

Figure 5.15: **Observation of induced absorption. a.** In the configuration shown in Fig. 5.9b, the probe experiences an opacity at Ω_B offset from the control laser. (Solid) Amplitude response of the probe laser. (Red-dashed) Curve fit to the (ω_1, k_1) optical mode. **e.** Probe phase response with distortion within the transparency. The observed phase data shows a change in slope that is opposite from that of the induced transparency phase data.

5.6 Strong coupling regime

When the coupling rate is comparable to the optical loss rate $|\beta||a_1| \approx \kappa$, the system enters the strong coupling regime [21]. In the strong coupling regime, a mode split is observed such that an optical resonance at the original frequency is completely removed. Instead, two new optical resonances which can be tuned using the coupling rate are observed.

Experimentally, the control field a_1 is used to manipulate the coupling rate. The coupling coefficient β can be held constant as it is defined by the optical modes only. In Fig. 5.18, the progression of the mode split with increasing control laser power is shown. Here, the strong coupling regime could be reached with only 40 μW of dropped input optical power. The optical loss rate κ=4.4 MHz and acoustic loss rate Γ_B=16.9 kHz are extracted from the experimental data.

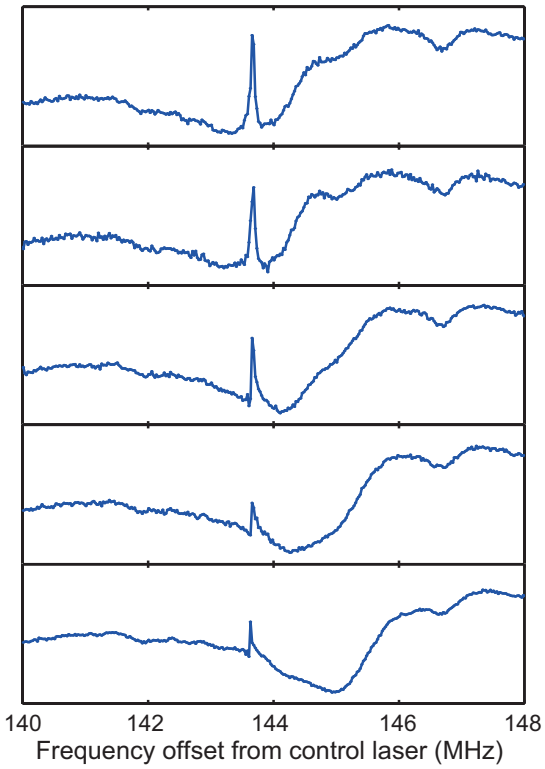

Figure 5.16: Tuning optical modes. Tuning the control laser frequency causes a relative detuning of the anti-Stokes optical mode while the transparency remains at a fixed frequency offset, Ω_B In this example, a SBS triplet with Ω_B= 143.7 MHz is used.

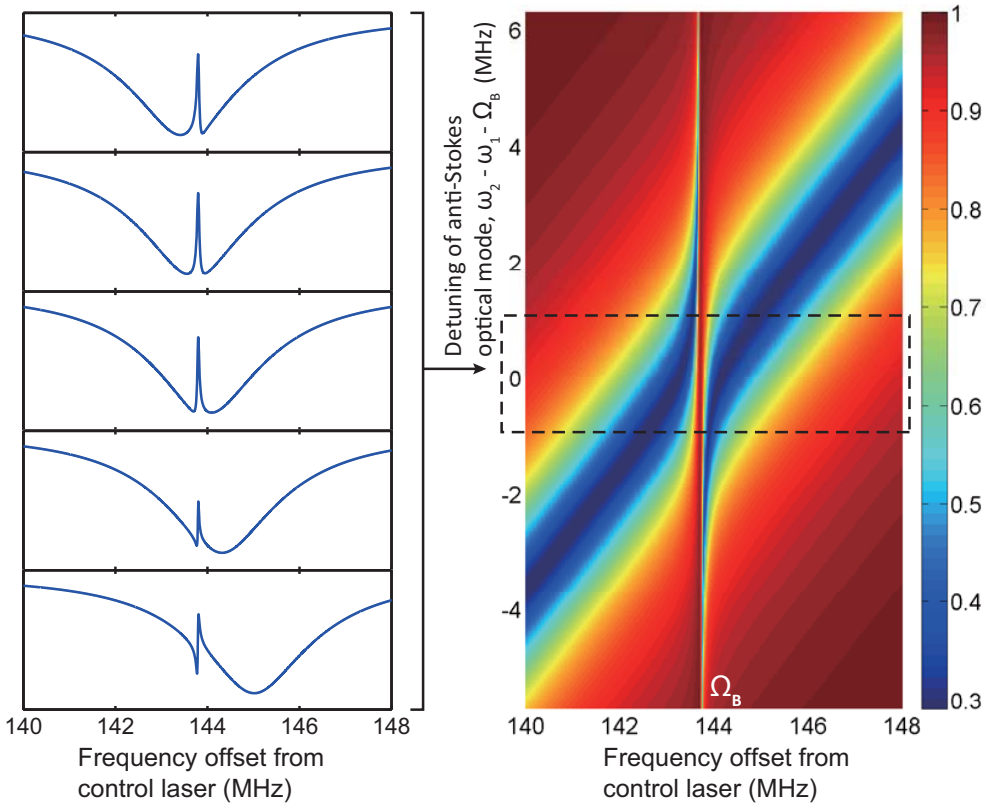

Figure 5.17: Theoretical modeling through Eq. 5.7 shows the stationary transparency at Ω_B while the anti-Stokes optical mode is tuned through the control laser frequency. This is consistent with experimental result from Fig. 5.16.

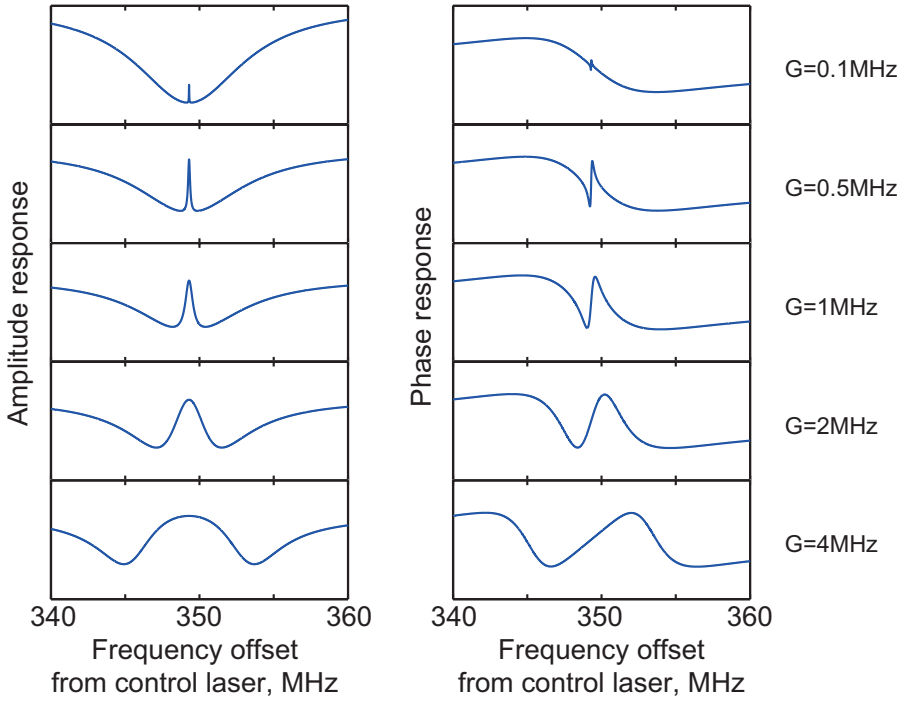

Figure 5.18: (Left) Increasing the control laser power increases the coupling rate, $G = |\beta||a_1|$, and the coupling rate increases the amplitude of the transparency peak. Past the strong coupling regime, the mode splitting occurs. (Right) The corresponding phase response is shown.

CHAPTER 6

CONTROLLING VELOCITY OF LIGHT USING BRILLOUIN SCATTERING INDUCED TRANSPARENCY

6.1 Introduction

Shortly after the first demonstration of electromagnetically induced transparency (EIT) [19], it was quickly realized that the induced transparency systems can slow down the speed of light and that it has anomalous dispersion. And in 1995, the slow light was experimentally demonstrated using EIT for the first time which showed 165-fold speed reduction compared to the speed in vacuum [181]. Today, the state of the art slow light systems utilize Bose-Einstein condensates which was first used in slow light application by Hau in 1999 to demonstrate the speed of light reduction down to 17 m/s [20]. Since then, much effort has been put in for further reduction of speed of light, longer light storage time, and higher fidelity of restored light [203].

The ability to control the velocity of light is a powerful technology because of its potential for significantly increasing performances of optical devices. The slow light technique is often implemented in applications where the interaction length or time is directly related to the device performance such as an optical gyrocope [189, 204, 205] or an interferometer [206, 207]. Furthermore, the control over the speed of light is useful in several optical signal processing applications including optical buffering [208] and optical data storage [209]. For instance, the optical buffer is an essential component in an optical fiber network for separating pulses or packets of data which can only be processed one at a time. In this case, the optical buffer slows down a pulse in order to prevent any unwanted merging or cross-talking of the optical

Work presented in this chapter has been published in: "Non-reciprocal Brillouin scattering induced transparency", Nature Physics, vol. 11, p. 275, 2015.

data. The optical signal processing and optical data storage are also attracting more interests since the optical transistor has been demonstrated [210] and the research on optical computing is starting to emerge.

In this chapter, we show that Brillouin scattering induced transparency (BSIT) also exhibits the distinct dispersion feature found in EIT for showing the slow and fast light. The slow light and time delay can be inferred from BSIT probe response (Fig. 5.14) and, as one might expect, fast light from Brillouin scattering induced absorption result (Fig. 5.15). In addition to the large time delay achievable, BSIT distinguishes itself with its compact size, light weight, low power consumption (SWaP), and ease of preparation without a need for reaching cryogenic temperatures.

6.2 Group velocity and group index

Before explaining how the velocity of light can be controlled, let us clarify what we can and cannot control. The velocity of light that we are familiar with, commonly expressed as c = 3×10^8 m/s in vacuum, is the velocity of phase front. The electromagnetic wave propagating in z direction with a constant phase $\phi = kz - \omega t$ has a phase velocity defined as

$$v_p = \frac{dz}{dt} = \frac{\omega}{k} = \frac{c}{n_\phi} \tag{6.1}$$

where the propagation vector and refractive index are functions of frequency, $k = k(\omega)$ and $n_\phi = n_\phi(\omega)$. The phase velocity v_p defined here is the universal speed of light that cannot be controlled unless the light is propagating through a medium with different refractive index. Also, this is the speed of light appearing in Einstein's special relativity.

When we claim "we generate the slow light", we do not control the speed at which the photon is propagating, but rather we are controlling the "group velocity" of light pulse such that it travels at the slower rate compared to the phase velocity. The group velocity v_g is expressed as

$$v_g = \frac{d\omega}{dk} = \frac{c}{n_\phi + \omega\frac{dn_\phi}{d\omega}} = \frac{c}{n_g} \tag{6.2}$$

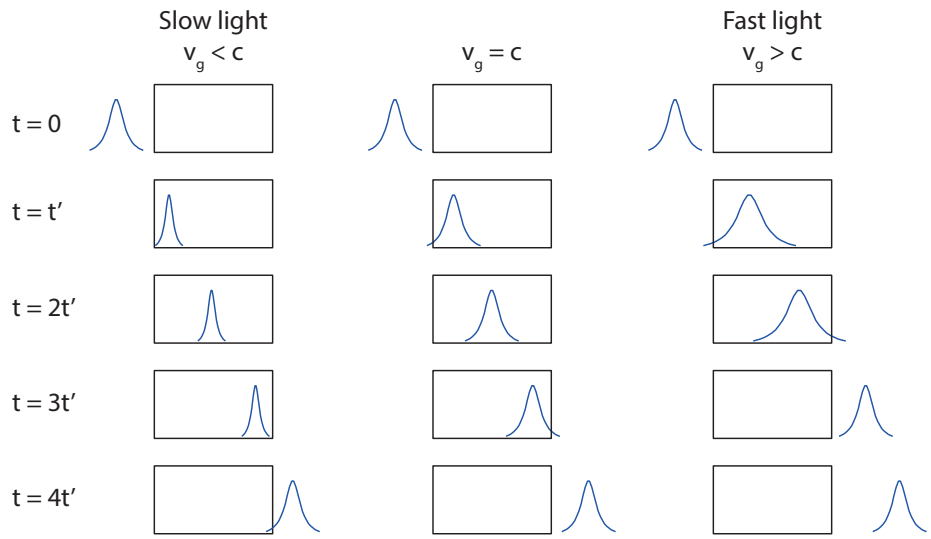

Figure 6.1: An illustration of light pulse traveling through slow light, ordinary, and fast light medium. Figure is recreated from [211]

where n_g is the group index[1]. Thus, we modify the group index n_g to achieve the slow and fast light, and the pulse propagation speed is modified accordingly. Also, in slow (fast) light medium, the effective index is high (low) leading to compression (rarefraction) of the light pulse (Fig. 6.1).

6.3 Kramers-Kronig relations

There are several different methods that can be used to create the requisite disturbances in the optical dispersion and to observe the slow and fast light. EIT and other induced transparency analogues are popular methods for generating the slow and fast light [103, 182]. Also, spectral hole burning effect through coherent parametric oscillations creates a narrow window of increased transmission which results in the generation of slow light [212, 213]. Others have used metamaterials to engineer refractive indices [214]. All of the methods mentioned above creates a response spectrum that resembles a resonance as shown in Fig. 6.2a. In fact, this is a necessary condition for the observation of slow and fast light as governed by Kramers-Kronig relations.

The Kramers-Kronig relation describes a transformation (Hilbert transform) of real to imaginary parts and vice versa of a complex function under

[1]The group index can be derived by solving the group velocity formula $\frac{d\omega}{dk}$ with the propagation vector defined as $k = \frac{\omega n(\omega)}{c}$.

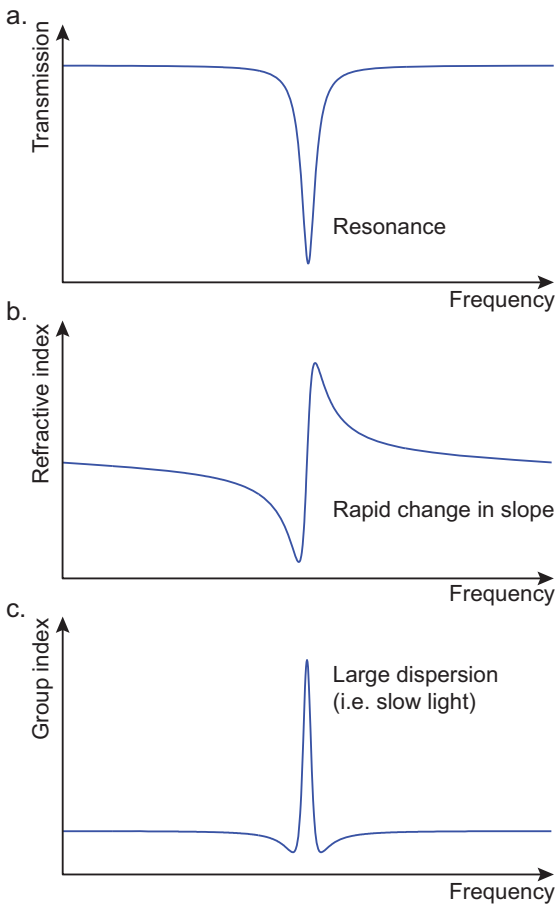

Figure 6.2: **a.** An example transmission signal with resonance dip. **b.** The refractive index calculated using the Hilbert transform of the transmission signal. **c.** The slope of the refractive index, i.e. dispersion. The positive value of group index indicates the generation of slow light.

the assumption of causality [215]. The concept of causality will be explain later in Ch. 6.4.3, but simply, all physical systems are believed to be causal[2]. For instance, light entering a medium interacts with the atoms and re-emit radiation. Causality requires that the radiation from the atom to emit only after the incident light excites the atoms first. Thus, the refractive index or optical dispersion under hilbert transformation gives the material absorption and vice versa as it obeys causality. In fact, for any variable in general defined as a complex function $Z(\omega) = A(\omega) + iB(\omega)$, the Hilbert transform, H, relates the real and imaginary parts as

[2]Causality violation is an important topic of research relevant in quantum mechanics and relativity theory [216].

$$A(\omega) = H(B(\Omega)) = \frac{1}{\pi}\int_{-\infty}^{\infty}\frac{B(\Omega)}{\omega-\Omega}d\Omega$$
$$B(\omega) = -H(A(\Omega)) = -\frac{1}{\pi}\int_{-\infty}^{\infty}\frac{A(\Omega)}{\omega-\Omega}d\Omega \tag{6.3}$$

The resonance feature in the frequency spectrum (Fig. 6.2a) shows a dip in transmission with a narrow linewidth which is necessary to acquire a rapidly changing dispersion $|dn/d\omega|$ and to increase the time delay. Although we experimentally measure the probe phase response as shown in the previous chapter, we can theoretically estimate the optical dispersion and time delay from the transmission spectrum alone using the Kramers-Kronig relations (Fig. 6.2).

6.4 Translating phase dispersion to time delay

According to the Kramers-Kronig relations, the extremely sharp transparency window presented earlier (Fig. 5.14) is accompanied by a rapidly changing phase dispersion and slow light. To translate how much time delay we can expect, we estimate the group delay τ_g using the equation

$$\tau_g = \frac{d\phi}{d\omega} \tag{6.4}$$

where ϕ is phase response and ω is frequency. The group delay equation is derived from the group velocity equation (Eq. 6.2) assuming a weak probe [217]. Using this relationship, the probe phase response from the induced transparency and absorption experiments can be further analyzed in terms of slow and fast light.

6.4.1 Slow light

Once again we recall Brillouin scattering induced transparency result from Fig. 5.14. Particularly, the probe phase response reveals rapidly changing dispersion within the transparency window. In the group delay equation (Eq. 6.4), the positive τ_g represents an optical delay and a negative value represents an optical advancement. Hence, we interpret the result as the slow light with a very low group velocity for the optical probe propagation [103,

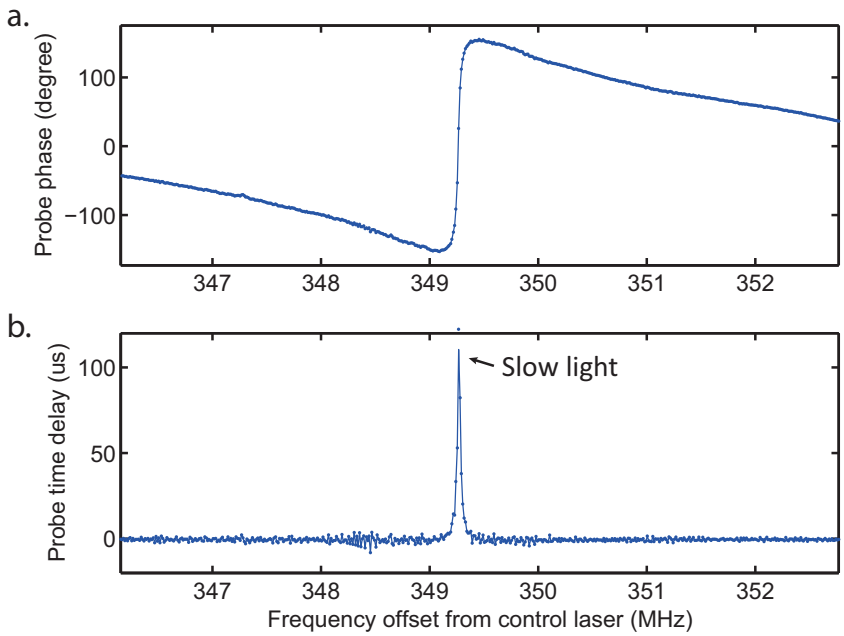

Figure 6.3: **a.** Probe phase response from induced transparency is shown. **b.** Additional probe group delay is generated compared to the transmission time without BSIT. 1 μW of laser power is used to generate time delay of 110 μs.

211]. Taking a derivative of phase with respect to the frequency, the time delay of 110 μs is estimated as shown in Fig. 6.3.

6.4.2 Fast light

As oppose to Brillouin scattering induced transparency, the induced absorption result shows the probe phase response with a negative slope corresponding to the fast light dispersion feature. When we exammine the probe phase response from Fig. 5.15, the slope is an opposite sign which we interpret as the superluminal optical propagation with 35 μs advancement as shown in Fig. 6.4.

6.4.3 Causality in fast light system

Among many different values that the group velocity can take, the group velocity that is faster than the speed of light ($c = 3\times10^8$ m/s) requires an additional consideration regarding the causality. We briefly mentioned earlier

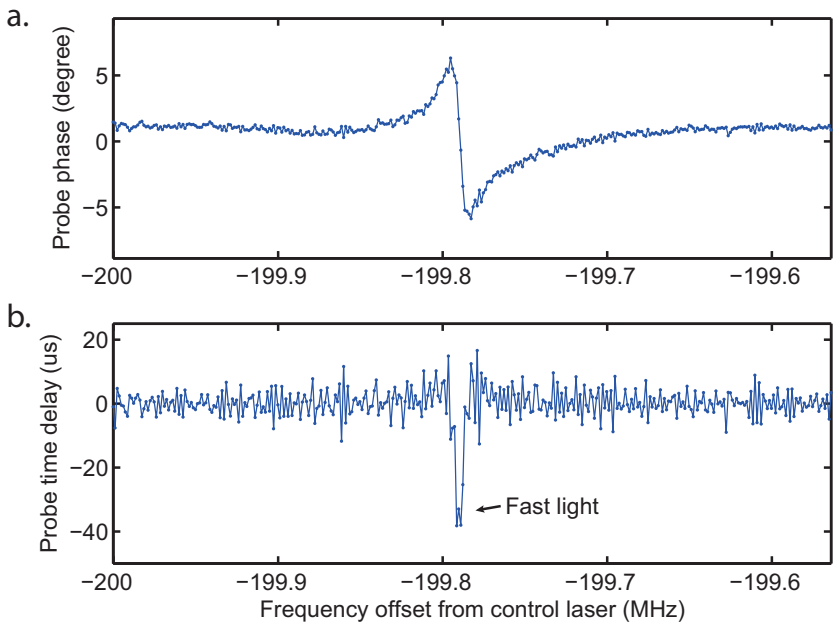

Figure 6.4: **a.** Probe phase response from induced opacity is shown. **b.** Probe time advancement is shown compared to the transmission time without Brillouin scattering induced opacity. Time advancement of 35 μs is demonstrated using 380 nW of control laser power.

that all physical systems must satisfy the Kramers-Kronig relations due to the causality constraints. The fast light system is no exception to those rules.

Einstein conjectured in the theory of special relativity that a signal cannot transfer information faster than the speed of light. Thus in 1914, Brillouin and Sommerfeld conducted a thought experiment to answer how causality is broken or sustained in a slow light system [211, 218, 219, 220, 221]. Their argument came in two parts. First was that the leading edge of any signal with finite length cannot travel faster than the speed of light c and that the peak cannot overtake the leading edge[3] (Fig. 6.5). In 1969, Icsevgi and Lamb have shown that the light pulse with group velocity exceeding the speed of light distorts in a way that the pulses pile up instead of overtaking and proved that the fast light system is causal even in nonlinear medium [211, 220]. Second, a light pulse with very long leading and trailing tails such as a Gaussian beam can in fact have a peak that travels at a rate faster than the speed of light c. Even in such cases, no information is being transferred

[3]The terminology used is "a signal with compact support cannot have a front velocity that exceeds the speed of light". Here, the compact support refers to the signal with finite length and the front velocity refers to the velocity of the leading edge.

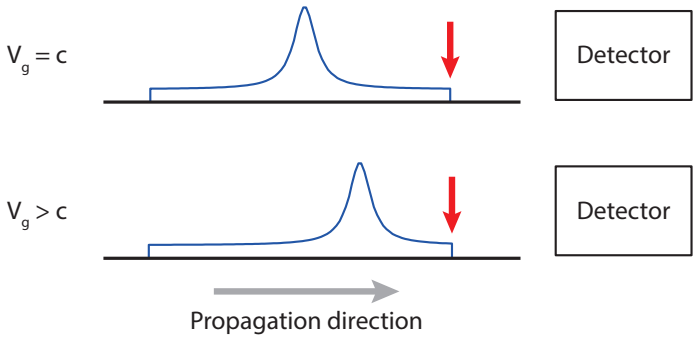

Figure 6.5: The causality in fast light system can be visualized with a pulse having an exaggerated, abrupt starting point (indicated by red arrow). Even if the pulse peak travels at the superluminal speed, the information does not transmit faster than the speed of light as the leading edge reaches the detector at the same time.

at the speed faster than the speed of light as any part of the Gaussian-like pulse shape theoretically carries the identical information and the entire pulse shape can be reconstructed [211, 221]. Therefore, the causality is maintained in the fast light system.

6.5 Comparison of BSIT based slow light with previous demonstrations

The figure of merit typically reported in slow and fast light systems is the group delay and bandwidth product. However, the delay-bandwidth product in SBS systems can be arbitrarily increased within technical limits by increasing the control laser power and waveguide length [222, 223, 224, 225]. Also, it is noted that both the laser power and device size are engineering-related constraints that must be budgeted wisely. This is critically important in on-chip devices where the laser power budgets are extremely small and kilometer-long waveguides (as in fiber SBS systems) are simply impractical.

Thus, in order to make a fair comparison between different SBS based systems, a figure of merit that normalizes the effects of control laser power and device length is suggested as follows.

$$FoM = \frac{\tau_g \Gamma_B}{I_c L} \tag{6.5}$$

where τ_g is group delay, Γ_B is bandwidth, I_c is laser power, and L is device

length. In other words, this FoM is simply a calculation of the intrinsic Brillouin gain in the system. By performing this normalization, a measure of the efficiency of the system for obtaining a certain delay-bandwidth product is found.

BSIT experimental data is compared against previous SBS slow light reports in Table 6.1. The resonator circumference is used as the device length L to compare our system against linear systems. It is shown that BSIT system provides a $\tau_g \Gamma_B$ product that is comparable to all previous demonstrations (order-of-magnitude is 1). In terms of the new FoM, however, our system provides a $\tau_g \Gamma_B$ product with 5 orders-of-magnitude lower power $\times$ length product than the next nearest system. This enormous engineering advantage makes our system particularly well-suited for on-chip SBS slow light systems.

Table 6.1: This table compares the figures-of-merit for various SBS slow light systems. For each publication, only the results with highest figure of merit value reported are presented. Our system has delay × bandwidth product ($\tau_g\Gamma_B$) that is on par with other SBS slow light systems. However, the power- and size- normalized figure of merit (Eq. 6.5) shows that our system is 5 orders-of-magnitude more efficient, i.e. can provide comparable $\tau_g\Gamma_B$ with 10^5 times lower power and size when compared against the next nearest prior result.

Author	Highest group delay, τ_g (μs)	Bandwidth, Γ_B (MHz)	Control laser power, I_c (mW)	Device length, L (km)	Delay × Bandwidth product, $\tau_g\Gamma_B$ (μs-MHz)	Normalized FoM, $\frac{\tau_g\Gamma_B}{I_cL}$ ($W^{-1}m^{-1}$)
This work (Slow light)	110	0.018	1	4.7×10^{-7}	1.87	3.98×10^{6}
This work (Fast light)	35	0.017	0.38	4.7×10^{-7}	0.63	3.53×10^{6}
R. Pant [167]	0.023	40	300	7×10^{-5}	0.92	4.38×10^{1}
K. Y. Song [222]	0.018	13.33	0.012	6.7×10^{0}	0.24	2.99
D. Deng [226]	0.37	1	1000	1×10^{-2}	0.37	3.69×10^{-2}
H. Ju [227]	0.04	11.24	20	2×10^{0}	0.45	1.12×10^{-2}
Y. Okawachi [223]	0.02	66.67	250	5×10^{-1}	0.4	1.07×10^{-2}
Y. Ding [202]	0.024	50	16	5×10^{1}	1.2	1.5×10^{-3}
L. Yi [225]	0.0008	812.5	100	1.25×10^{1}	0.65	5.2×10^{-4}

CHAPTER 7

COMPLETE OPTICAL ISOLATION USING BRILLOUIN SCATTERING INDUCED TRANSPARENCY

7.1 Introduction

Ideal optical isolators should exhibit complete linear isolation – where completeness implies perfect transmission one way (i.e. zero forward insertion loss) and zero transmission in the opposite direction – without any mode shifts, frequency shifts, or dependence on input signal power. Unfortunately, the established magneto-optical techniques [17, 228] for achieving nonreciprocal optical transmission [229] have proven challenging to implement in chip-scale photonics due to fabrication complexity, difficulty in locally confining magnetic fields, and material losses [16, 18, 47, 230] as discussed in Ch. 2.4. In light of this challenge, several non-magnetic alternatives for breaking time-reversal symmetry [229] have been explored both theoretically [65,104,175,231,232,233] and experimentally [9,12,13,14,15,234]. However, various limitations still persist with the proposals that are compatible with chip-scale fabrication. Nonlinearity-based nonreciprocal isolators are fundamentally dependent on input field strength [12, 234] and hence do not generate linear isolation [39]. Dynamic modulation [104,231] is a powerful approach that generates linear isolation, but current chip-scale demonstrations are still constrained by extremely large forward insertion loss and low contrast [9,13]. Finally, the Brillouin acousto-optic scattering approach [174,175] is based on using stimulated intermodal scattering enabled by phonons to induce unidirectional photonic loss. This technique promises linearity and easy implementation in most optical materials but requires waveguide lengths of

Work presented in this chapter has been published in: "Complete linear optical isolation at the microscale with ultralow loss," Scientific Reports, vol. 7, no. 1, p. 1647, 2017.

several centimeters to several meters [15] for practical isolation. Recent advancements in on-chip gain [235, 236] have improved the future potential of miniaturizing this approach, but till date no microscale SBS isolator has been demonstrated. Presently, there is no experimentally demonstrated magnet-free technique that can provide linear optical isolation, with ultra-low loss, and a microscale footprint at the same time. A comparison of state-of-the-art experimental results on non-magnetic microscale isolation can be found in Table 7.1.

Recently, a fundamentally different path to obtain nonreciprocal optical transport has emerged, by exploiting opto-mechanically induced transparency [10, 11, 22]. These nonreciprocal effects are based on destructive optical interference via a non-radiative acoustic coherence within a resonator-waveguide system, and are acousto-optic analogues of electromagnetically induced transparency (EIT). To date, however, only subtle nonreciprocity has been demonstrated by these optomechanical methods, without any expression or demonstration of a path to achieving complete isolation with ultra-low forward loss, both of which are requirements for practical use. We focus our study on the nonreciprocal Brillouin scattering induced transparency (BSIT) mechanism [22], in which momentum conservation requirement between photons and phonons helps break time-reversal symmetry for light propagation. More importantly, BSIT uniquely permits two major technical results that we demonstrate in this work. We show theoretically that when operating within the strong acousto-optical coupling regime (aided by the resonant pump) the BSIT system enables theoretically lossless transmission of light in the forward direction in a waveguide, while maintaining complete absorption in the reverse direction – the condition of complete linear isolation. Second, the non-zero momentum of the traveling phonons involved in BSIT permits independent forward/reverse reconfiguration of the isolation effect, in contrast to the zero-momentum mechanical excitations in optomechanically induced transparency [11] that can couple forward and reverse propagating light. Experimentally, we demonstrate a device operating very close to the strong coupling regime and capable of generating a record-breaking 78.6 dB of isolation contrast per 1 dB of forward insertion loss within the induced transparency bandwidth. Since the underlying interaction is available in all dielectrics, this isolation effect can in principle be implemented using any waveguide and resonator materials available in photonics foundries.

7.2 Background on Faraday optical isolator

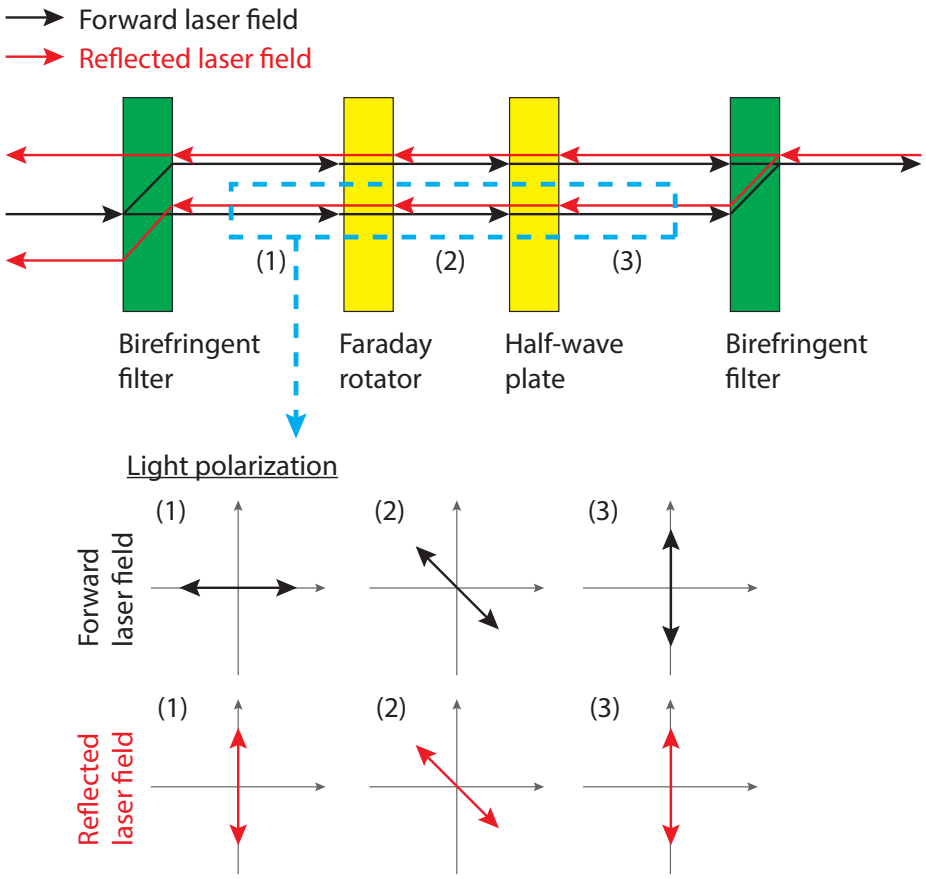

Figure 7.1: Light path and light polarization changes within an optical isolator. (Top) The reflected laser field does not travel back to the initial position of the forward propagating laser field. (Bottom) Unlike the half-wave plate, which rotates the polarization of light symmetrically, the Faraday rotator rotates the polarization non-reciprocally depending on the direction of light propagation.

The optical isolator is a directional filter that blocks light based on the propagation direction. Since there is no difference in characteristic of light traveling in the opposite direction, the polarization of light is modified based on the propagation direction first using the principle of Faraday effect. The Faraday effect describes a dielectric material's tendency to rotates the light polarization non-reciprocally given a magnetic field across the medium. In other words, two light fields traveling across the Faraday rotator in an opposite direction experience the rotation in the same direction. Therefore, if light field travels across the Faraday rotator and reflects or scatters back to its

original location, the polarization will not be identical to the initial polarization. By using two birefringent media or polarization filters before and after the Faraday rotator to refract and separate light with different polarization, the light may be allowed to travel only in one direction (Fig. 7.1).

Faraday rotator requires a biasing magnetic field to generate such an optical behavior. Therefore, an optical isolator typically houses a strong magnet. This is acceptable in many applications, but a magnet is difficult to integrate onto an optical circuit as magnet has to be bonded onto the device [237]. Therefore, a non-magnetic isolator is desirable for on-chip implementation and other applications that limits the use of magnet or magnetic field within a system.

7.3 Theoretical analysis

7.3.1 Qualitative description

Let us first qualitatively discuss how ideal optical isolation can be achieved by means of the BSIT light-sound interaction in dielectric resonators [10, 22]. We consider a whispering-gallery resonator having two optical modes (ω_1, k_1) and (ω_2, k_2) that are separated in (ω, k) space by the parameters of a high coherence traveling acoustic mode (Ω, q). This is the requisite phase matching relation for BSIT (Fig. 7.2), indicating that phonons enable coupling of the photon modes through photoelastic scattering. We stress here that the two modes should belong to different mode families of the resonator in order to ensure that scattering to other optical modes from the same phonon population is suppressed. When this system is pumped with a strong 'control' field on the lower optical resonance (ω_1, k_1), an EIT-like optomechanically induced transparency [101, 103] appears within the higher optical resonance (ω_2, k_2), due to coherent interference originating from the acousto-optical interaction [10, 22].

A description of this interference can be presented both classically [22] or through by a quantum mechanical approach [10]. Briefly, one can consider signal or 'probe' photons arriving from the waveguide at frequency ω_2 that are on-resonance and being absorbed by the resonator mode (ω_2, k_2). When the control field is present in a BSIT phase-matching situation, these probe

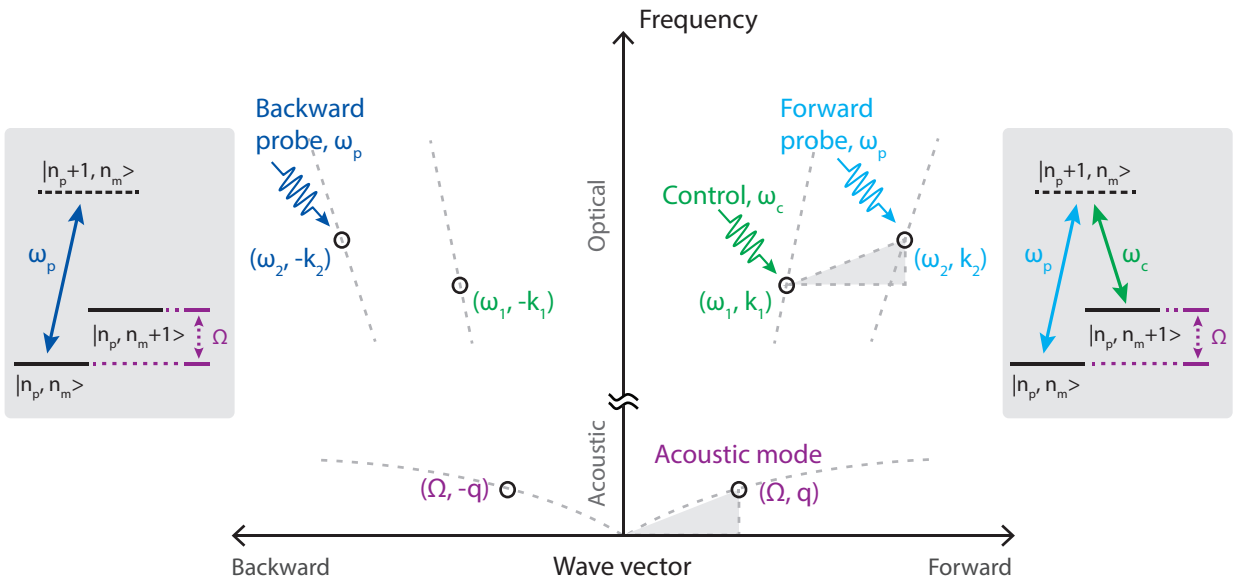

Figure 7.2: **a.** The interference of excitation pathways in the BSIT system are described through an energy-level picture (grey boxes), using probe photon number n_p and phonon number n_m. Absorption of a probe photon into the (ω_2, k_2) optical resonance is modeled as an effective transition $|n_p, n_m\rangle \rightarrow |n_p + 1, n_m\rangle$. In presence of the control field, the probe photon could scatter to the lower resonance (ω_1, k_1) while adding a mechanical excitation in (Ω, q), which is an effective transition to state $|n_p, n_m + 1\rangle$. However, the coherent anti-Stokes scattering of the control field from this mechanical excitation would generate an interfering excitation pathway for the original state $|n_p + 1, n_m\rangle$. This process is analogous to EIT and results in a window of transparency for the forward optical probe, inhibiting the original $|n_p, n_m\rangle \rightarrow |n_p + 1, n_m\rangle$ absorption transition. The necessary momentum matching requirement, not visible in the energy diagram, is represented using the dispersion relation (middle) to elucidate the breaking of time-reversal symmetry for the probe signal.

photons could scatter to (ω_1, k_1) causing a mechanical excitation of the system. However, anti-Stokes scattering of the strong control field from this mechanical excitation will generate a phase-coherent optical field that interferes destructively with the original excitation of the mode at (ω_2, k_2). The result is a pathway interference that is measured as an induced optical transparency in the waveguide, where no optical or mechanical excitation takes place, and the resonant optical absorption is inhibited (Fig. 7.3 top). The strength of this interference is set by the intensity of the control laser. The phase of the mechanically dark mode is instantaneously set by the phases of the control and probe optical fields, and does not require phase coherence between them.

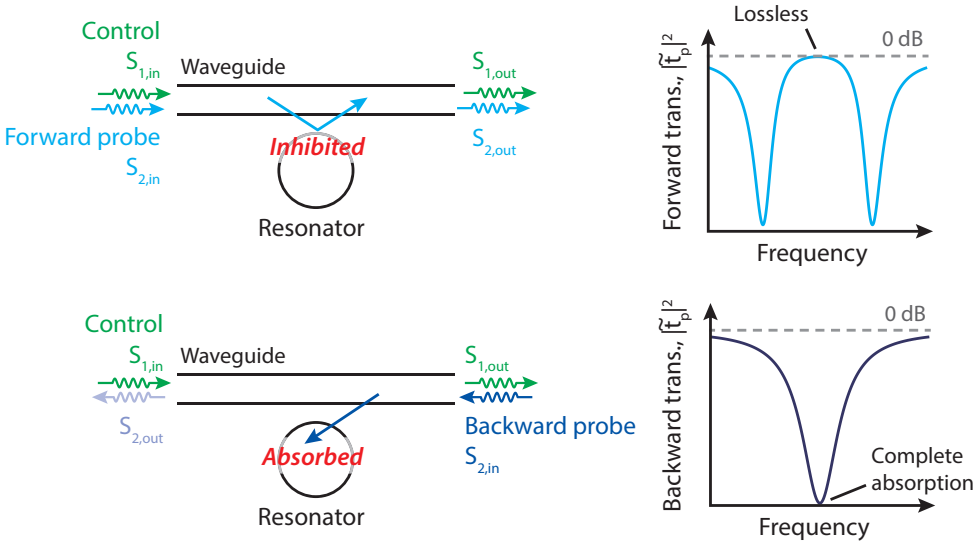

Figure 7.3: We implement this mechanism using a waveguide and a whispering gallery resonator, in which probe signals tuned to either of the (ω_2, $\pm k_2$) optical resonances are typically absorbed by the resonator under the critical coupling condition. The presence of a forward control field, however, creates the BSIT interference [22] only for forward probe signals and inhibits absorption. Under strong acousto-optical coupling, the waveguide-resonator system is rendered lossless at the original resonance.

It is crucial, however, to note that this transparency in BSIT only appears for probe signals co-propagating with the control laser. Probe light in the counter propagating i.e. time-reversed direction, on the other hand, occupies the high frequency optical mode with parameters (ω_2, -k_2). For BSIT to occur in this case, an acoustic mode having parameters (Ω, $-(k_1 + k_2)$) would be required for compensating the momentum mismatch between the forward control and backward probe optical modes. However, since such an acoustic mode is not available in the system, no interaction occurs for the counter-propagating probe and the signal is simply absorbed into the resonator (Fig. 7.3 - bottom).

7.3.2 Analytical description

The classical field equations for coupled light and sound in this waveguide-resonator system are presented in Ch. 5.3.1. The transmission coefficient $\tilde{t}_p$ of the probe laser field can be derived as

$$\tilde{t}_p \;=\; \frac{s_{2,\mathrm{out}}}{s_{2,\mathrm{in}}} \;=\; 1 - \frac{\kappa_{\mathrm{ex}}}{(\kappa_2/2 + j\Delta_2) + G^2/\left(\Gamma_B/2 + j\Delta_B\right)} \tag{7.1}$$

where $s_{i,\mathrm{in}}$ and $s_{i,\mathrm{out}}$ are the optical driving and output fields in the waveguide (Fig. 7.3) at the control (i=1) and probe (i=2) frequencies. G is the pump-enhanced Brillouin coupling rate manipulated by the control optical field $s_{1,\mathrm{in}}$ in the waveguide via the relation $G = \left|s_{1,\mathrm{in}}\,\beta\,\sqrt{\kappa_{\mathrm{ex}}}/\left(\kappa_1/2 + j\Delta_1\right)\right|$. Here β is the acousto-optic coupling rate, κ_i are the loaded optical loss rates, Γ_B is the phonon loss rate, and κ_{ex} is the coupling rate between the waveguide and resonator. The loaded optical loss rates are defined as $\kappa_i = \kappa_{i,\mathrm{o}} + \kappa_{ex}$ where $\kappa_{i,\mathrm{o}}$ is the loss rate intrinsic to the optical mode. The Δ_i parameters are the field detunings, with subscript B indicating the acoustic field. This response matches the system of optomechanically induced transparency (OMIT) [101, 103], with the exception that the pump field is also resonant and the coupling rate β is dependent on momentum matching. As we explain later, the pump resonance in BSIT significantly enhances the maximum coupling rate G achievable in contrast to single-mode OMIT systems.

Equation 7.1 is key to understanding how an ideal optical isolator can be obtained. First, we examine the case of no acousto-optic coupling $G = 0$, resulting from either modal mismatch ($\beta = 0$) or zero applied control laser power ($s_{1,\mathrm{in}} = 0$). In this case Eq. 7.1 exhibits a well-known Lorentzian shaped transmission dip implying that the probe optical field in the waveguide is simply absorbed by the resonator [95]. Critical coupling between resonator and waveguide is enabled when $\kappa_{\mathrm{ex}} = \kappa_{2,\mathrm{o}}$ and results in complete absorption of the probe light from the waveguide at resonance ($\Delta_2 = 0$). With critical coupling in place, let us now introduce the effects of the acousto-optic coupling. For very large acousto-optic interaction strength, i.e. $G \to \infty$, Eq. 7.1 indicates that we recover perfect transmission $\left|\tilde{t}_p\right|^2 = 1$ even when the waveguide and resonator are critically coupled. Forward propagating probe light in the waveguide, co-propagating with the control laser, can thus transmit perfectly with no absorption at resonance in the ideal case. At the same time, we have no Brillouin coupling ($\beta = 0$) for counter-propagating control and probe optical fields due to the momentum mismatch as indicated previously. This implies that, for a counter-propagating probe, the system remains in the critical coupling region resulting in complete absorption. Since

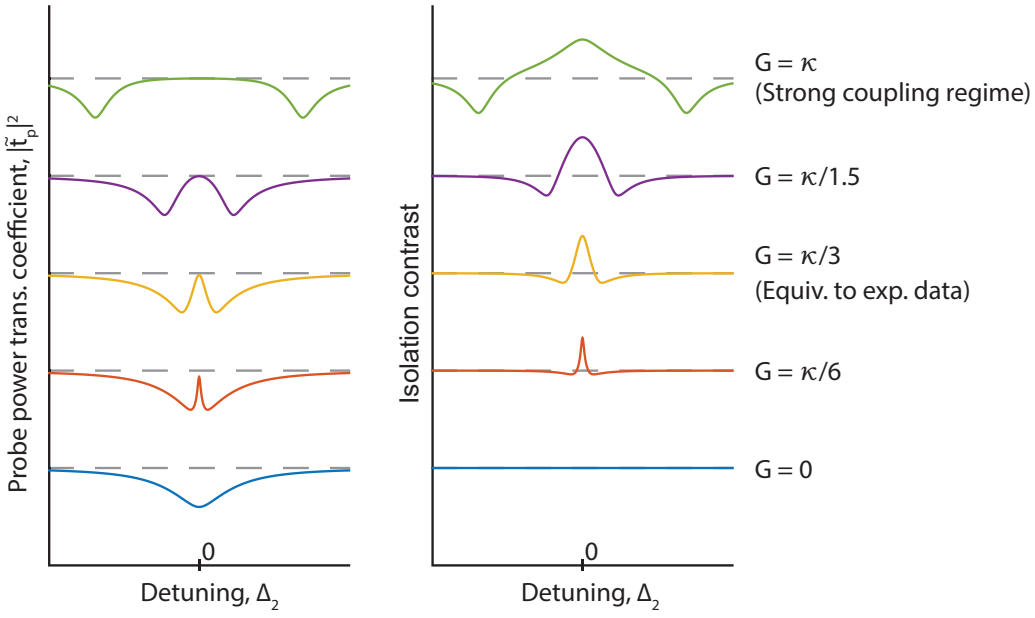

Figure 7.4: **Evolution of the transparency and isolation contrast as a function of pump-enhanced Brillouin coupling G.** In the weak coupling regime ($G \ll \kappa$), the transparency linewidth and contrast bandwidth are defined by the acoustic linewidth Γ_B [22]. As coupling G increases, the isolation contrast improves, bandwidth is expanded and the optical mode with transparency appears as a splitted mode. In the strong coupling regime, the isolation bandwidth is independent of the acoustic mode and is instead defined by optical mode linewidth κ only. The dashed lines indicate the perfect transmission baseline (left) and zero isolation contrast (right) respectively.

forward probe signals transmit with zero absorption, and backward probe signals are completely absorbed (Fig. 7.3), this system is an ideal linear isolator at the transparency resonance.

A more practically accessible case is $G \geq \kappa_2$, also known as the strong coupling regime [238], where the induced transparency grows to the width of the optical mode. Strong coupling can be reached for high coherence phonon modes (small Γ_B) with large acousto-optic coupling β and large control driving field $s_{1,\text{in}}$. The evolution of the optical transparency and isolation contrast with increasing coupling G is illustrated in Fig. 7.4. In the weak coupling regime ($G \ll \kappa_2$) the isolation contrast is defined roughly by the linewidth of the phonon mode. As G increases the transparency window broadens until eventually reaching the strong coupling regime where the isolation contrast bandwidth reaches a maximum equaling the optical loss rate κ_2, as

long as the acoustic frequency is higher than this value. Thus, the isolation bandwidth can be improved to the several GHz range if a higher frequency acoustic mode is used [200] in conjunction with a low-Q (high κ_2) optical mode, and the reduction in coupling is compensated by other means [76]. In this regime, we also achieve the desired ultra-low forward insertion loss. Such large transparency can also be interpreted as the splitting of the optical mode [239]. The absence or minimization of forward loss necessarily implies linear optical response at frequency ω_2 without any nonlinearity or mode conversion.

7.4 Methodology

7.4.1 Waveguide-resonator system

We experimentally demonstrate ultra-low loss optical isolation by probing light transmission through the waveguide in the forward and backward directions simultaneously. In our experiment, a tapered optical fiber waveguide is fabricated by linear tension drawing of SMF-28 fiber while being heated with a hydrogen flame [240], till the point that the tapered waveguide diameter is comparable to the laser wavelength and supports only a single optical mode with significant evanescent field. With adiabatic tapering [117] the loss associated with this waveguide can be made as low as 0.003 dB [241]. We employed a resonator of diameter 170 μm to guarantee the natural existence of multiple triplets of acoustic and optical modes that satisfy the phase-matching condition for BSIT, although smaller resonators may also be used. The microsphere resonator is fabricated by reflow of a single-ended optical fiber taper using an arc discharge. The fiber mode is coupled to the resonator by means of evanescent field overlap with the resonator's whispering gallery modes. The optical coupling rate is controlled using distance with a piezo-nanopositioner.

7.4.2 Experimental setup

The experimental setup used for the simultaneous forward and backward measurements is shown in Fig. 7.5. We employ a 1520-1570 nm tunable

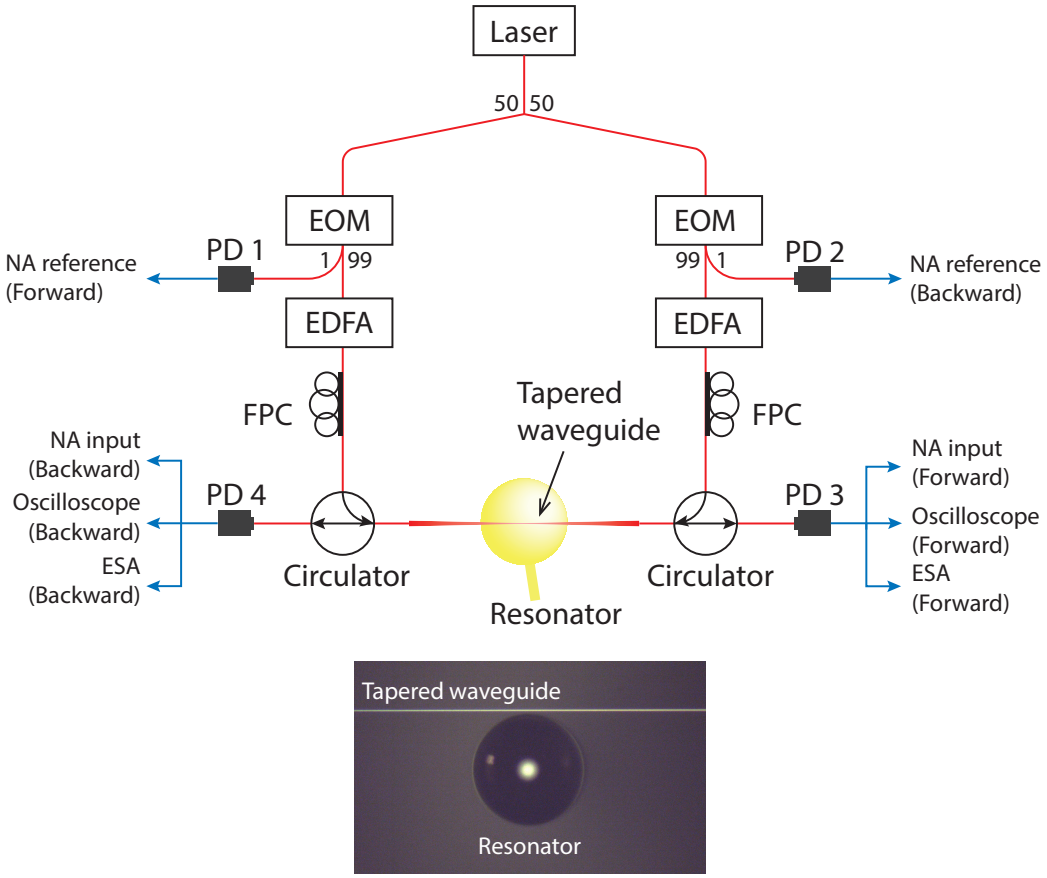

Figure 7.5: Experimental setup for simultaneous forward and backward probe transmission measurements is shown. We use a matched set of optical components including the electro-optic modulator (EOM), the erbium-doped fiber amplifier (EDFA), the fiber polarization contrller (FPC), the circulator and the photodetectors (PD) for the forward and backward measurements. Light is coupled to the resonator via tapered waveguide. An electronic network analyzer (NA) performs ratiometric measurements of NA reference and NA input signals (marked in figure) in the forward and backward directions. The electrical spectrum analyzer (ESA) is also used to observe the acoustic phonon mode by measuring the beat note generated by the control laser and Brillouin light scattering by the phonons.

external cavity diode laser (ECDL) to generate the control and probe laser fields. This laser source is first split into the forward and backward directions using a 50:50 splitter. Electro-optic modulators (EOM) are employed as variable optical attenuators in dc mode (i.e. by adjusting the bias voltage) for manipulating control laser power in either direction. The probe laser is also derived from the control laser using the same EOMs to generate two

sidebands spectrally separated from the control by the modulation frequency ω_m. The probe laser frequency $\omega_p = \omega_c + \omega_m$ can be swept using ω_m relative to the control laser ω_c. An erbium-doped fiber amplifier (EDFA) is used after each EOM to independently modify the control laser power, which in turn regulates the pump-enhanced Brillouin coupling rate G in either direction. Fiber polarization controllers (FPC) are used to match the light polarizations of the forward and backward propagating laser fields. Two circulators are placed before and after the resonator to allow simultaneous measurements of the probe transmissions in the forward and backward directions without reconfiguring the experimental setup. We use a total of four photodetectors, two for measuring the forward and backward probes which are used as references (PD1 and PD2 in Fig. 7.5) and the other two for measuring the forward and backward probe transmissions through the resonator-waveguide system (PD3 and PD4 in Fig. 7.5). The experiment is performed at room temperature and atmospheric pressure condition.

7.4.3 Determining the optical probe transmission coefficient

The probe transmission coefficient $\tilde{t}_p$ is measured with the help of a network analyzer, which performs a coherent ratiometric analysis of beat notes of the control and probe optical signals at various points in the experiment (see Fig. 3 in the Manuscript). Here, we dissect the network analyzer measurement to explain how the probe transmission coefficient is extracted from the experimental data.

The control laser with frequency ω_c is electro-optically modulated at ω_m to create two sidebands. By keeping the modulation depth low, we can ensure the sidebands are small compared to the carrier, allowing a first-order approximation of the spectrum. We can thus write the optical field within the fiber prior to the resonator as the following

$$\tilde{E}_{in} = E_c e^{-j\omega_c t}\left(1 + \frac{m}{2}e^{j\omega_m t} + \frac{m}{2}e^{-j\omega_m t}\right) + c.c. \tag{7.2}$$

where E_c is the carrier or control laser field amplitude and m is the modulation depth. The control laser frequency ω_c and modulation frequency ω_m are adjusted such that the control laser and upper sideband overlap with optical modes while the lower sideband does not couple to any of the resonator's op-

tical modes. We use the upper sideband as the optical probe to measure light transmission through the system, while the control laser parked at the lower frequency optical mode enables the Brillouin scattering interaction between the optical mode pair.

The optical field arriving at the photodetector after passing through the taper-resonator system (PD3 in the forward case, PD4 in the backward case, see Fig. 3 in the Manuscript) can then be expressed as

$$\tilde{E}_{out} = E_c e^{-j\omega_c t}\left(\tilde{t}_c + \tilde{t}_{ls}\frac{m}{2}e^{j\omega_m t} + \tilde{t}_p\frac{m}{2}e^{-j\omega_m t}\right) + c.c. \tag{7.3}$$

where $\tilde{t}_i$ are the complex valued transmission coefficients of the control, lower sideband, and probe (upper sideband) fields (i=c, ls, p respectively) through the waveguide. Since the lower sideband does not couple to the resonator, its transmission coefficient is simply $\tilde{t}_{ls} = 1$. The probe transmission coefficient $\tilde{t}_p$ measured in the forward and backward directions defines the optical isolation performance.

The optical power measured at the output detector (PD3 or PD4 depending on the probe direction) can be extracted from Eqn. 7.3 as shown below. Here we consider only the terms that fall within the detector bandwidth at frequency ω_m.

$$\begin{aligned} P_{out} \propto \left|\tilde{E}_{out}\right|^2 &= |E_c|^2 t_c \frac{m}{2}\left(e^{-j\omega_m t} + \tilde{t}_p e^{-j\omega_m t}\right) + c.c. \\ &= |E_c|^2 t_c m \left[\ \left(1 + \mathrm{Re}(\tilde{t}_p)\right)\cos\omega_m t \ + \ \mathrm{Im}(\tilde{t}_p)\sin\omega_m t\ \right] \end{aligned} \tag{7.4}$$

Without loss of generality we have set $\tilde{t}_c$ with a phase of zero, i.e. all other fields are referenced to the phase of control field. The RF (electrical) output signal from the photodetector is P_{out} multiplied by the detector gain.

The network analyzer requires a reference signal to perform the ratiometric measurement. We generate this reference by directly measuring the optical signal prior to the resonator, i.e. Eq. 7.2, at PD1 (PD2 in the backward direction, see Fig. 3 in the Manuscript). As above, this reference signal is proportional to the optical power

$$P_{ref} \ \propto \ 2\,|E_c|^2\, m\cos(\omega_m t) \tag{7.5}$$

With respect to this $\cos(\omega_m t)$ reference, the first term in the parentheses in Eq. 7.4 provides the in-phase component $\left(1 + \mathrm{Re}(\tilde{t}_p)\right)$ of the measurement, while the second term provides the quadrature component $\mathrm{Im}(\tilde{t}_p)$. The network analyzer output typically converts this measurement to the polar form

$$Ae^{j\phi} = \frac{t_c M}{2}\left(1 + \tilde{t}_p\right) \tag{7.6}$$

where A is the amplitude response, ϕ is the phase response, and M is a coefficient accounting for a fractional difference between optical powers measured at the reference photodetector and at the photodetector placed after the resonator at a decoupled state. M includes EOM output power split ratio (1:99), EDFA gain, and difference in photodetectors' sensitivities.

The frequency and power of the control laser remain unchanged during the experiment, resulting in a constant t_c that can be determined by monitoring the control laser transmission. M and t_c can also be determined together through the network analyzer response when the probe is off resonance from the anti-Stokes mode, i.e. in the case where $\tilde{t}_p = 1$. Using this information, curve fitting can be performed on the network analyzer measurement, and the complex $\tilde{t}_p$ can be separately determined as a function of offset (from the control laser) frequency ω_m. However, we note that the transmission coefficient extracted using Eq. 7.6 is not of the probe field only. We must also consider the effect of coherent light sources other than the probe for the accurate measurement of the true probe transmission coefficient. We discuss this in detail in the next section.

7.4.4 Background light in probe measurements

In ultra-high-Q resonators, coherent spontaneous light scattering from the control laser by small intrinsic defects can populate the anti-Stokes optical mode. There may also be direct injection of the control laser into the anti-Stokes optical mode. While this extra light is generally small, it does result in competition with the small amount of anti-Stokes light scattering from the acoustic mode in the structure (the phenomenon of interest) and can contaminate measurements of $\tilde{t}_p$. An exemplary measurement of this spurious light is shown in Fig. 7.6. Since both light sources are being generated from the same pump/control laser, there can be interference that complicates the

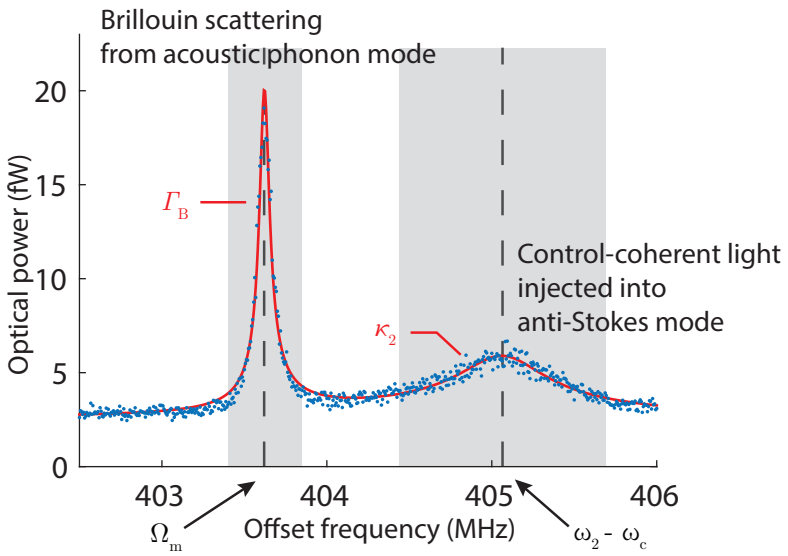

Figure 7.6: Measurement of Brillouin scattering at Ω_m and the control-coherent background light (from defect induced scattering and direct injection) shaped by the anti-Stokes optical mode at ω_2. Both sources are offset from the control laser by roughly 404 MHz. This measurement is derived from their beating with the control field on a photodetector and measured by an RF electronic spectrum analyzer. The additional background light is typically too small to be observed except when it is resonantly amplified by an ultra-high-Q resonator. The Brillouin scattering occurs at a fixed frequency defined by the phonon mode Ω_m while the background light is tunable by modifying the control laser frequency.

measurement of the probe transmission (Fig. 7.7).

We can easily observe the evidence of this additional light in the background using an electrical spectrum analyzer that monitors the RF power measurement from the photodetector. Fig. 7.6 shows the spectrum of beat notes generated from scattering by the acoustic phonon mode centered at $\Omega_m = 403.6$ MHz, and from background light within the anti-Stokes optical mode centered at $\omega_{as} = 405.1$ MHz offset from the control laser frequency. Since the resonant frequency of the phonon mode is fixed, the frequency of the beat note originating from Brillouin scattering does not change when the control laser frequency changes. However, the beat note generated from the control-coherent background light injected into the anti-Stokes optical mode can be moved in frequency space with the control laser.

Since the proposed sources of background light (defect scattering, direct injection) are proportional to the intracavity control field a_1, we can model

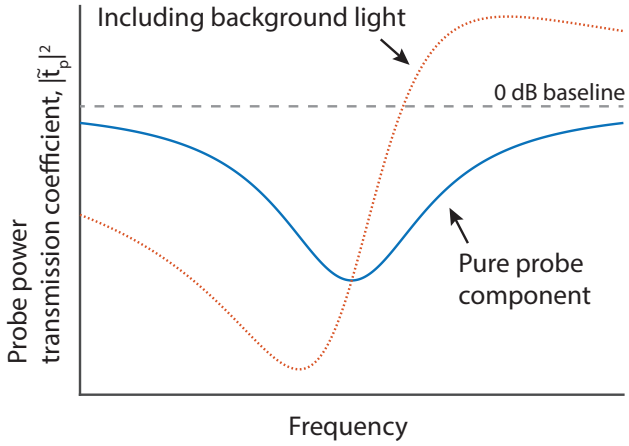

Figure 7.7: The network analyzer measurement shows an asymmetric probe power transmission coefficient $\left|\tilde{t}_p\right|^2$ (red-dotted line) in spite of the optical mode being symmetric. The distortion in the measurement originates from the background light injected to the anti-Stokes optical mode, creating difficulty in the estimation of the 0 dB transmission baseline (grey-dashed line) and optical mode center frequency. After correcting for the background light, the symmetric optical transmission is seen (blue-solid line).

them as a coherent source driving the anti-Stokes mode with coupling strength r relative to the control field. This extra source can be included in the equations describing our system as follows :

$$\begin{aligned}
\dot{a_1} &= -(\kappa_1/2 + j\Delta_1)a_1 - j\beta^* u^* a_2 + \sqrt{k_{ex}} s_{1,in} \\
\dot{a_2} &= -(\kappa_2/2 + j\Delta_2)a_2 - j\beta u a_1 + \sqrt{k_{ex}} s_{2,in} + jra_1 \\
\dot{u} &= -(\Gamma_B/2 + j\Delta_B)u - j\beta^* a_1^* a_2 + \xi \\
s_{i,out} &= s_{i,in} - \sqrt{k_{ex}}\, a_i \mid \text{where } i{=}1{,}2
\end{aligned} \tag{7.7}$$

As discussed in Ch. 5.3.1, the control field scattering $j\beta^* u^* a_2$ and thermal fluctuation ξ can be assumed to be negligible. We find the modified steady-state intracavity probe field a_2 which is composed of the unperturbed probe response and an additional background light term:

$$\begin{aligned}
a_2 &= \frac{\sqrt{k_{ex}} s_{2,in}}{\gamma_2 + G^2/\gamma_B} + \frac{jra_1}{\gamma_2 + G^2/\gamma_B} \\
\gamma_i &= \kappa_i/2 + j\Delta_i \\
\gamma_B &= \Gamma_B/2 + j\Delta_B
\end{aligned} \tag{7.8}$$

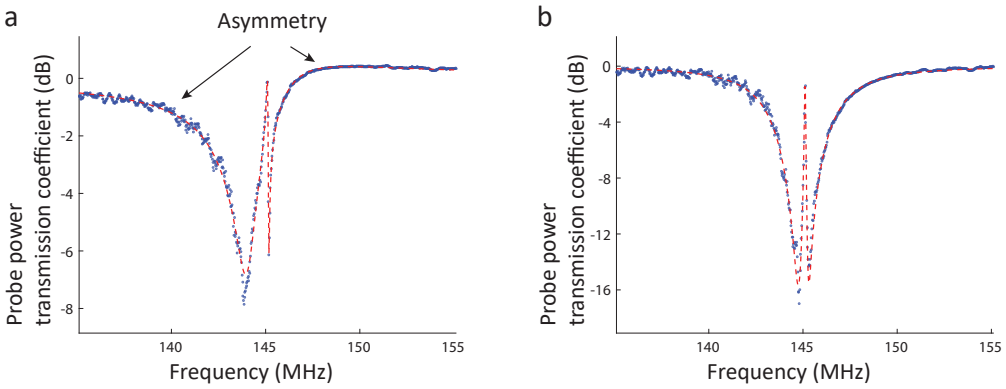

Figure 7.8: **a.** Raw amplitude response data from the network analyzer. The optical transmission measurement and the induced transparency are distorted by the additional light within the anti-Stokes optical mode. **b.** Probe optical power transmission is plotted using input-output relation after removal of the background light. Data shows transparency within the Lorentzian shaped optical mode. The red dashed line represents a fit using theoretical model for induced transparency.

where $G = |\beta a_1|$ is the pump-enhanced Brillouin coupling rate. The probe field arriving at the photodetector is then expressed as

$$\begin{aligned} s_{2,out} &= \left(1 - \frac{k_{ex}}{\gamma_2 + G^2/\gamma_B}\right) s_{2,in} - \left(\frac{jr\sqrt{k_{ex}}}{\gamma_2 + G^2/\gamma_B}\right) a_1 \\ &= \tilde{t}_{p,\text{actual}}\, s_{2,in} \;\; - \;\; \left(\frac{jr\sqrt{k_{ex}}}{\gamma_2 + G^2/\gamma_B}\right) a_1 \end{aligned} \tag{7.9}$$

implying that the measured probe transmission coefficient (by definition) will be

$$\begin{aligned} \tilde{t}_{p,\text{measured}} &= \frac{s_{2,out}}{s_{2,in}} \\ &= \tilde{t}_{p,\text{actual}} \;\; - \;\; \left(\frac{jr\sqrt{k_{ex}}}{\gamma_2 + G^2/\gamma_B}\right) \frac{a_1}{s_{2,in}} \end{aligned} \tag{7.10}$$

From Eq. 7.10, we note that we can reduce the effect of the background light by increasing the probe laser power (larger $s_{2,in}$) during the experiment such that the first term dominates. The measured transmission coefficient $\tilde{t}_{p,\text{measured}}$ acquired from Eq. 7.6 will then approach the actual transmission coefficient $\tilde{t}_{p,\text{actual}}$. More generally, however, the second interfering term results in an asymmetry (irrespective of acousto-optical coupling) in the optical

transmission through high-Q resonators measured by this pump-probe technique.

In Fig. 7.7 we plot Eq. 7.9 with acousto-optical coupling set to zero ($G = 0$). The extra light in the resonator modifies the transmission coefficient such that the high frequency side of the optical mode exceeds 0 dB baseline while the low frequency side is artificially dipped. When we exclude the background light, the plot now reveals a symmetric optical mode and a true resonance frequency. Thus, factoring out this asymmetry is critical in accurately determining the optical isolation performance. Unprocessed transmission measurement from the network analyzer (Fig. 7.8a) shows the asymmetric optical mode shape and different 0 dB baseline levels on either side of the resonance. Such a mismatch in baseline is used to estimate the degree of asymmetry and the coupling strength r. The background light can then be subtracted from the measurement to obtain $\tilde{t}_{p,actual}$ as shown in Fig. 7.8b. In the Fig. 7.8 example, a symmetric optical mode with transparency at the center of the optical mode is revealed.

7.5 Experimental result

7.5.1 Demonstration of high-contrast ultralow-loss isolation

We experimentally demonstrate ultra-low loss optical isolation (Fig. 7.9, 7.10) in the waveguide-resonator system by probing optical transmission through the waveguide in the forward and backward directions simultaneously (see Methods §7.4). A resonator of diameter 170 μm is used to guarantee the natural existence of multiple triplets of acoustic and optical modes that satisfy the phase-matching condition for BSIT.

The requisite BSIT phase-matching is first experimentally verified by strongly driving the (ω_2, k_2) optical mode and observing spontaneous and stimulated Stokes Brillouin scattering into the lower mode (ω_1, k_1) in the forward direction [200]. Subsequently, we drive the (ω_1, k_1) optical mode with a strong control laser (<1 mW) and use a weak co-propagating probe laser to measure the power transmission spectrum across the high frequency optical mode (ω_2, k_2) revealing the induced transparency window. The control laser detuning and power are adjusted in order to maximize the power transmission

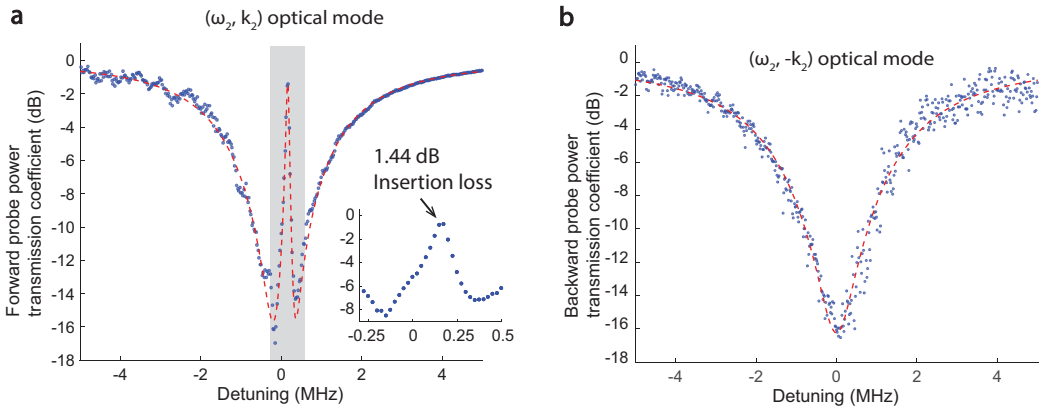

Figure 7.9: **Experimental observation of extremely low insertion loss linear optical isolation. a.** Probe power transmission coefficient $\left|\tilde{t}_p\right|^2$ is measured in the forward direction through the waveguide near the (ω_2, k_2) mode, with fixed 66 μW pump power dropped into the (ω_1, k_1) mode. The forward probe power transmission coefficient through the waveguide shows only 1.44 dB insertion loss within the transparency. The phonon mode frequency is 145 MHz. **b.** The (ω_2, -k_2) optical mode measured by the backward probe does not exhibit the induced transparency, resulting in conventional absorption of the probe signal by the resonator.

within the transparency peak. Experimental measurements of the probe power transmission $\left|\tilde{t}_p\right|^2$ in both forward and backward directions are presented in Fig. 7.9. To show optical isolation, the same measurement is taken in the forward and backward directions while the constant control driving field $s_{1,\mathrm{in}}$ is supplied in the forward direction only. In this experiment the two selected optical modes of the resonator have linewidth $\kappa_1 \approx \kappa_2 \approx 4.1$ MHz, and are spaced approximately 145 MHz apart. They are coupled by means of a 145 MHz acoustic mode of intrinsic linewidth $\Gamma_\mathrm{B} \approx 12$ kHz. Through finite element simulations, we estimate that the acoustic mode corresponds to a first order Rayleigh surface acoustic exictation having an azimuthal order of M=24. At a diameter of 170 μm, this translates to an acoustic momentum of $q = 0.28\ \mu m^{-1}$ and ensures breaking of interaction symmetry for co-propagating and counter-propagating probe fields (Fig. 7.2).

As seen in Fig. 7.9a the system exhibits very low forward insertion loss (1.44 dB) at the peak of induced transparency region for 66 μW control laser power absorbed to the resonator (power launched in fiber is 680 μW). This corresponds to an experimentally calculated pump-enhanced Brillouin coupling of $G \approx \kappa_2/12$. At this point, the acoustic mode has an effective

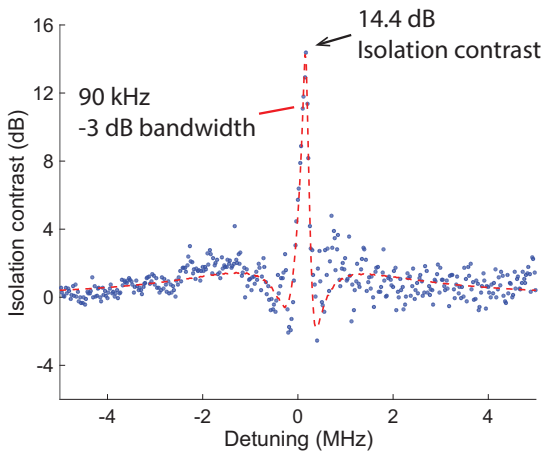

Figure 7.10: The optical isolation contrast is evaluated as the difference between forward and backward power transmission coefficients. Here we calculate 14.4 dB peak contrast with a -3 dB bandwidth of 90 kHz. Isolation exists over 470 kHz.

linewidth of 80.4 kHz due to Brillouin cooling [100]. Simultaneous measurement of backward probe power transmission (Fig. 7.9b) shows only the absorption spectrum of the unperturbed (ω_2, -k_2) optical mode, generating a power transmission loss of 15.8 dB in the waveguide. Subtraction of the forward and backward measurements provides a measure of the optical isolation contrast, which is 14.4 dB here with ∼90 kHz full width at half maximum (Fig. 7.9c).

Since the forward insertion loss is very low (zero in the ideal theoretical case), the isolation contrast is primarily determined by the proximity of the waveguide-resonator coupling to the critical coupling condition, which if achieved would yield infinite isolation contrast. Achieving critical coupling $\kappa_{ex} = \kappa_{2,o}$ in non-integrated waveguide-microsphere systems is very challenging due to multimode waveguiding in the taper, thermal drifts during the experiment, and vibrational or mechanical stability issues. Previously, up to 26 dB of signal extinction has been experimentally demonstrated in a fiber taper-microsphere system [242]. In the future, ideal isolation may be approached if the waveguide and resonator are integrated on-chip, since most mechanical issues can be eliminated and the interacting modes can be designed precisely. Alternatively, applications that require high contrast may employ multiple isolators in series with minimal penalty due to the extremely low insertion loss in this system. It is thus appropriate to compare perfor-

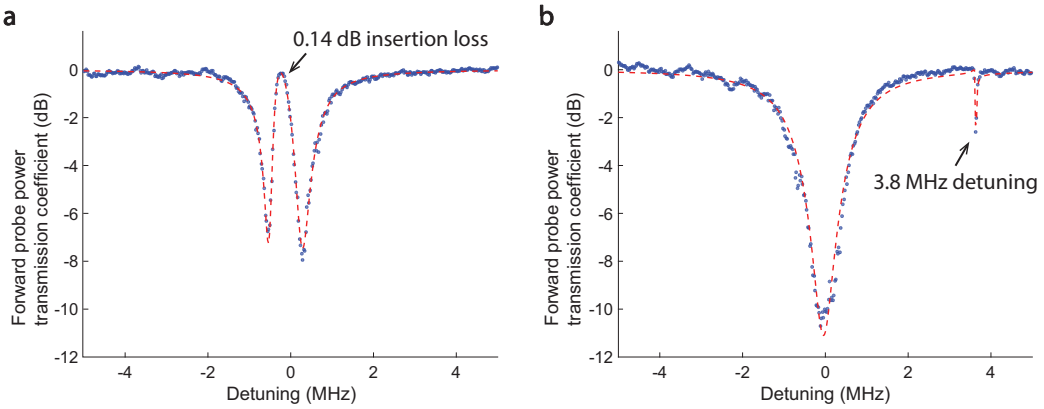

Figure 7.11: **Demonstration of ultra-low forward insertion loss with stronger coupling G. a.** Here, we use a triplet of optical and acoustic modes with an optical mode separation or acoustic frequency of 164.8 MHz. Pump-enhanced Brillouin coupling rate G is much higher due to better acousto-optic modal overlap and 235 μW power absorbed into the control mode. This results in $G \approx \kappa/3$ causing the forward insertion loss within the transparency to decrease to only 0.14 dB. The isolation bandwidth also increases to approximately 400 kHz. **b.** The transparency-free (ω_2, k_2) optical mode is observable by detuning the control laser from the (ω_1, k_1) optical mode, which also detunes the scattered light.

mance of different isolators by referencing the achieved contrast to 1 dB forward loss. The data shown in Fig. 7.9 indicates this figure of merit of approximately 10 $\mathrm{dB_{isolation}/dB_{loss}}$ (units preserved for clarity, indicating 14.4 dB constrast vs 1.44 dB forward loss).

Theory indicates that much lower forward insertion loss can be obtained if much higher coupling rate G is arranged, either by lowering the loss rates of the optical modes, or by using higher control laser power. Fortunately, a special feature of two-mode systems such as BSIT [243] is the resonant enhancement of the intracavity pump photons in mode ω_1, which enables much easier access to the strong coupling regime. Nonreciprocity based on single-mode OMIT [11] does not possess this feature and it is thus impractical to expand the isolation bandwidth and reach the ultra-low loss regime. Making use of this resonant enhancement, in Fig. 7.11a we show a system nearly reaching the strong coupling regime with $G \approx \kappa/3$, exhibiting only 0.14 dB forward insertion loss (96.8% transmission) and isolation contrast estimated at 11 dB. Here, 235 μW control power is coupled to the resonator (700 μW launched in fiber). The unmodified optical mode absorption can be easily

observed by detuning the control laser such that the interference is generated outside the optical mode (Fig. 7.11b). This result indicates that the strong coupling regime is also within the reach of this silica waveguide-resonator system [243]. The isolation figure of merit (referenced to 1 dB insertion loss) for the Fig. 7.11 result is quantified at 78.6 $dB_{isolation}/dB_{loss}$. This compares extremely well to commercial fiber-optic Faraday isolators whose figures of merit typically range between 60 - 100 $dB_{isolation}/dB_{loss}$, and far exceeds the capabilities demonstrated till date by any other non-magnetic microscale optical isolation approach. As shown in Table 7.1, our achieved contrast exceeds the next best microscale experimental result in non-magnetic optical isolation [14] by nearly 7 orders-of-magnitude (69.5 dB difference, i.e. 78.6 dB vs 9.09 dB) per 1 dB of insertion loss.

7.5.2 Independent reconfiguration of optical isolation

Finally, we also demonstrate the optical reconfigurability of the isolation direction by means of independent control lasers that propagate in opposite directions. This is demonstrated through an experiment (Fig. 7.12) where the the control laser field is sequentially provided in the forward direction only, backward direction only, and in both directions simultaneously. Since the forward and backward directions in a whispering-gallery resonator are nominally decoupled and the phonon mode also has an associated directionality (i.e. momentum), the transparency is independently observed in the directions in which a control laser field is supplied.

Fig. 7.12 shows that when no control field is provided, the anti-Stokes optical mode is a simple Lorentzian shaped dip. However, when the control laser is supplied in the forward direction, a transparency is observed by the forward probe. While this transparency is sustained in the forward direction, we can independently switch on and off the transparency in the backward direction. This is demonstrated by probing the anti-Stokes optical mode in the backward direction with and without a backward control laser, which results in an optical mode with and without transparency respectively. Such reconfigurable transparency has never previously been demonstrated in any other optical or opto-mechanical system. OMIT-based nonreciprocity [11] does not possess the capability of fully independent reconfiguration

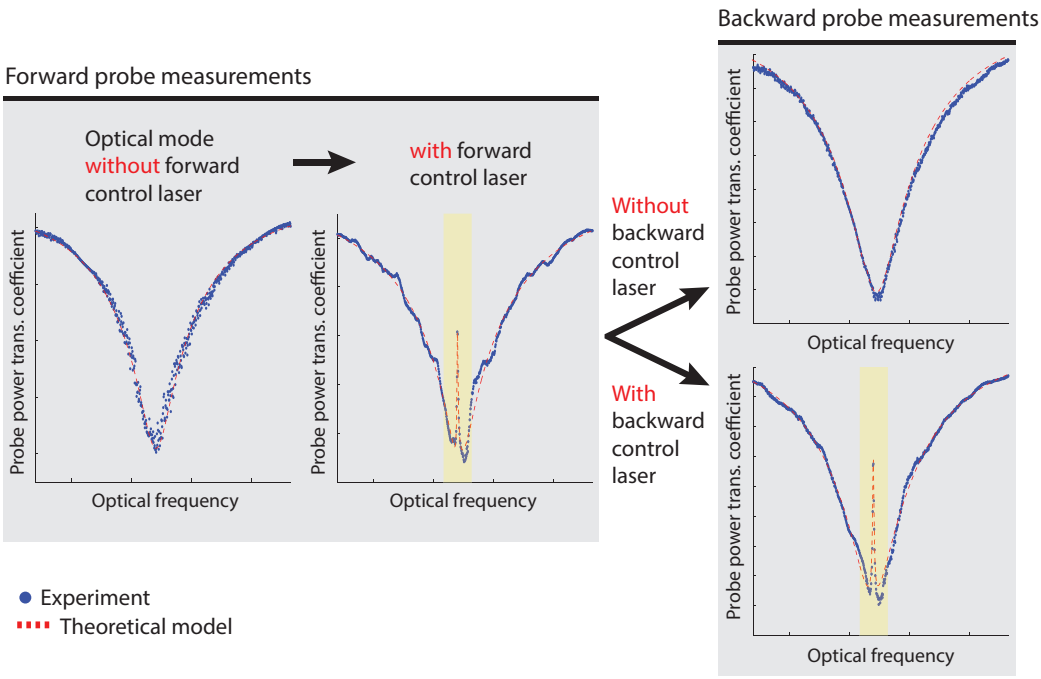

Figure 7.12: Demonstrating reconfigurable optical isolation. Increasing the control laser power in the forward direction, we observe the appearance of the acousto-optical transparency. While transparency is enabled in the forward direction, we can switch on and off the transparency in the backward direction using a separate backward propagating control laser. The red dashed line represents a fit using theoretical model for induced transparency.

since both forward and reverse optical signals interact with the same zero-momentum vibrational mode. Thus photon conversion can occur through an optomechanical dark mode [244] shared between forward and reverse pumps, i.e. forward (reverse) sources can modify light propagation in the reverse (forward) direction.

7.5.3 Comparison of isolation performance

We quantitatively compare isolation performance against previously demonstrated linear, magnet-free optical isolators in Table 7.1. Isolation contrast (extinction ratio), quantifies the ratiometric difference for the forward and reverse transmitted optical signals. Insertion loss quantifies the difference in the input and forward transmitted signals. All these approaches only operate over finite bandwidth, for which the 3 dB bandwidth quantifies the

frequency span over which the contrast is within 3 dB of its highest value. We also provide device size and the system used to assist with determining the fit for specific applications. Since isolators may also be cascaded to increase contrast, we normalize the isolation contrast for each demonstration using 1 dB of insertion loss as a reference point, and provide the figure of merit as dB of contrast per 1 dB of insertion loss.

While many previous reports show signatures of optical nonreciprocity, several do not quantify the contrast or insertion loss metrics making it difficult to have a direct comparison. Sayrin et. al. report an excellent contrast per 1 dB of insertion loss from a resonantly enhanced spin-polarized cold atom system [14]. However, the target applications are different from the other magnet-free isolation approaches reported here as this requires laser cooling of the system. Lira et. al. report an impressive bandwidth of 200 GHz, but only show 3 dB contrast and extremely high insertion loss [9].

Our result exhibits an enormous 78.6 dB contrast per 1 dB of insertion loss, which rivals the values seen on commercial magneto-optic based optical isolators. Our demonstration has 69.5 dB higher figure of merit (nearly 7 orders-of-magnitude) relative to the next best microscale isolator result [14].

7.6 Conclusion

Achieving complete linear optical isolation through opto-mechanical interactions that occur in all media, irrespective of crystallinity or amorphicity, material band structure, magnetic bias, or presence of gain, ensures that the technique could be implemented in nearly any photonic foundry process with any optical material. Example systems that could support this isolation approach are released optomechanical resonators with co-integrated waveguides such as those shown in [245]. Since the isolation bandwidth demonstrated here is relatively narrow, but is wavelength agnostic, this approach must be tailored for particular photonic device applications. However, we must emphasize that the maximum bandwidth of this isolation approach under strong acousto-optical coupling is only limited by the optical mode linewidth κ_2, allowing future improvement in isolation bandwidth to several GHz with the use of low optical Q-factor modes and higher acoustic frequencies. In contrast to all previous works, this induced transparency approach

ensures that bidirectional signals are attenuated by default, and only unidirectional transport is enabled when the control optical stimulus is applied. This scheme additionally ensures protection for the system to be isolated in case of failure of the control source, and allows the possibility of dynamic optical shuttering. The absence of magnetic or radiofrequency electromagnetic driving fields make this approach particularly useful for chip-scale cold atom microsystems technologies, for both isolation and shuttering of optical signals, and laser protection without loss.

Table 7.1: Comparison of isolation performance for experimentally demonstrated non-magnetic linear non-reciprocal systems.

Author	Technique	Isolation contrast	Insertion loss	3 dB Band-width	Device size	Contrast (dB) per 1 dB insertion loss (dB/dB)	System used
Isolation using photonic microdevice							
This work	BSIT	11 dB	0.14 dB	400 kHz	170 μm	78.6	Microsphere
H. Lira et. al. [9]	Interband scattering	3 dB	70 dB	200 GHz	110 μm	0.0429	Waveguide on-chip
J. Kim et. al. [22]	BSIT	N/A	N/A	16.9 kHz	150 μm	N/A	Microsphere
C.-H. Dong et. al. [10]	BSIT	N/A	N/A	9 kHz	196 μm	N/A	Microsphere
Z. Shen et. al. [11]	OMIT	N/A	N/A	22 kHz	36 μm	N/A	Microsphere
B. Peng et. al. [239]	PT symmetry breaking	N/A	N/A	N/A	60 $\mu m^{\dagger}$	N/A	Toroid on-chip
L. D. Tzuang et. al. [13]	Photonic Aharonov-Bohm effect	2.4 dB	N/A	N/A	325 μm	N/A	Waveguide on-chip
Isolation through atom interactions							
C. Sayrin et. al. [14]	Scattering from spin-polarized cold atoms	7.8 dB	1.08 dB	N/A	0^{*}	7.22	Atoms on tapered fiber
C. Sayrin et. al. [14]	Same as above with resonant enhancement	13 dB	1.43 dB	N/A	36 μm	9.09	Atoms on resonator
Isolation in macroscale fiber system							
M. S. Kang et. al. [15]	Stimulated Brillouin scattering	20 dB	N/A	7 MHz	15 m	N/A	Photonic crystal fiber

† Requires two resonators of size 60 um. * Size of an atom. N/A = Not available.

CHAPTER 8

INTEGRATION TO OPTICAL CIRCUIT

In many applications, miniaturization of large, macro-scale devices is of great interest as a means to improve cost-effectiveness. Fluidic experiments often requiring large channels and pumps are moving towards micro-scale lab-on-a-chip platform for the cost and time savings as the interaction time necessary for studying many physical effects reduces with a decrease in device size [246, 247, 248]. National Institute of Standards and Technology (NIST) is persuing their own verson of lab-on-a-chip which miniaturizes many of their sensors and integrates them in a single, field-deployable package [249, 250, 251]. And there is an effort to miniaturize an entire optical system including light source, waveguide, resonator, detector, and other necessary optical components into a single optical circuit [252, 253, 254]. With many advancements in lithography techniques, the size of micro-scale devices continues to decrease. However, reducing the device size and migrating to MEMS platform can be difficult especially with optical components. Therefore, we discuss designs and methods necessary for the integration of optical resonator devices on-chip.

The goal here is to explore technologies on-hand for implementing previously demonstrated BSIT optical isolator in optical circuits. Current commercial optical isolators rely on the Faraday effect and are realized in systems built with rare-earth metal iron garnets. Years of research and development in precision optics and Faraday optical isolation techniques have led to an excellent optical isolation contrast as well as low insertion loss. However, the limitations arising from the rare-earth metal iron garnets' magneto-optic coefficients are not yet overcome. Terbium gallium garnet (TGG) commonly used for the construction of Faraday optical isolators for its large magneto-optic coefficient (50 to 300 Rad/Tm at visible wavelength) still requires cm-scale device length for an optimal optical isolation. Therefore, the Faraday optical isolators with micron-scale device length suitable for microsystems

fail to reach the desired performance. In addition, the lack of deposition and etching methods for magnets and iron garnets complicates the microfabrication and truly monolithic integration of Faraday optical isolators on-chip. For this reason, the magnet-free optical isolation techniques such as BSIT optical isolator appeal as desirable alternatives for optical systems on-chip.

The construction of optical system on-chip consists of many optical devices such as lasers, couplers, waveguides and many more depending on the application. For implementation of an optical isolator into such system, we consider the design of BSIT optical isolator and how it can be modified to adapt to micro-scale optical systems better. This includes the design considerations to minimize the optical isolator's influences to the overall system. Also, we consider the compatibility of BSIT optical isolator with common optical materials found in microsystems.

8.1 Resonator and waveguide material

Before the resonator and waveguide designs are presented, we briefly comment on the material used for the fabrication of BSIT optical isolator on-chip. In the first experimental demonstration o f Brillouin scattering induced transparency (BSIT) [22], microsphere optical resonator constructed from a tapered optical fiber (Corning SMF-28e+) is used. This particular optical fiber consists of core and cladding both made from silicon dioxide (SiO_2) for its excellent optical transmission characteristic in the C-band (1530 to 1565 nm). In this wavelength, the optical loss is typically less than 0.2 dB/km. Furthermore, SiO_2 is a material with well-established fabrication processes from the semiconductor industry and is compatible with CMOS fabrication processes [136]. The challenge in using SiO_2, however, lies in the fabrication of on-chip waveguides. Similar to the optical fiber where a core is surrounded by a cladding layer, the on-chip waveguide also requires a core and a cladding. The cladding is required to have the refractive index that is lower than the refractive index of the core. This allows the light to be confined within the core by the total internal reflection. However, the material with index lower than SiO_2 (1.45) is rare besides air or vacuum, which cannot support released structures.

A good alternative to SiO_2 is silicon nitride (SiN_x). SiN_x is also CMOS fabrication compatible and is optically transparent at C-band [136,255]. But most importantly, SiN_x has a refractive index of 1.99. Therefore, SiO_2 makes a good cladding material for SiN_x core.

8.1.1 Brillouin gain

Brillouin gain is a material property which determines the degree of amplification from Brillouin scattering. In the context of BSIT and slow light, Brillouin gain also determines the group delay. Brillouin gain, g_o, is defined in Eq. 8.1.

$$g_o = \frac{\gamma_e^2 \omega^2}{nvc^3 \rho_o \Gamma_B} \tag{8.1}$$

where g_o is Brillouin gain, γ_e is electrostrictive coefficient, ω is laser frequency, n is refractive index, v is speed of sound, c is speed of light in vacuum, ρ_o is material density, and Γ_B is acoustic linewidth (or inverse of phonon lifetime $\tau = \Gamma_B^{-1}$) [171]. In Eq. 8.1, it is important to note that the Brillouin gain does not have inverse relationship to the refractive index, but instead the Brillouin gain is proportional to n^7 because the electrostrictive coefficient is proportional to n^4 [256].

Therefore, the material with different values of electrostrictive coefficient and refractive index may be explored. For instance, chalcogenide has a very high electrostrictive coefficient which will further enhance SBS effects [257]. And there are materials with negative electrostrictive coefficient [258] which may bring interesting applications in the future.

8.2 On-chip resonator designs

In the first demonstration of Brillouin scattering induced transparency (BSIT) [22], the microsphere optical resonator coupled to tapered fiber coupoler is used. Despite the ease of fabrication process, both the resonator and coupler are not compatible with chip-scale fabrication process. Typically, any 3-dimensional structure in microsystems is expensive and time-consuming. Therefore, other alternatives of sphere resonators are considered here.

Fortunately, BSIT is not bound by the resonator geometry as Brillouin

scattering is a material-level nonlinear effect. There exists several optical resonator designs that supports BSIT and were previously fabricated on-chip such as disc [75], double disc [259], ring [260], toroid [137], racetrack [261], Bragg-reflector [262], photonic crystal [263] and many more. Of such optical resonators, we have fabricated disc, toroid and ring resonators (Fig. 8.1) for further analysis.

Among the three designs, the disc resonator etched using hydrogen fluoride (Fig. 8.1a) is the most promising for integration to optical circuit. This wedged disc resonator design is shown to provide good optical mode confinement as well as high quality factor [75] whereas the ring resonator etched using dry etching technique (deep reactive ion etching) has low quality factor due to the surface roughness during the etching process (Fig. 8.1c, d). Lastly, the toroid resonator fabricated by melting the disk resonator with CO_2 laser shows good device performance (Fig. 8.1b). However, the lasing process changes the device diameter during formation of torus making the implementation of on-chip waveguide difficult.

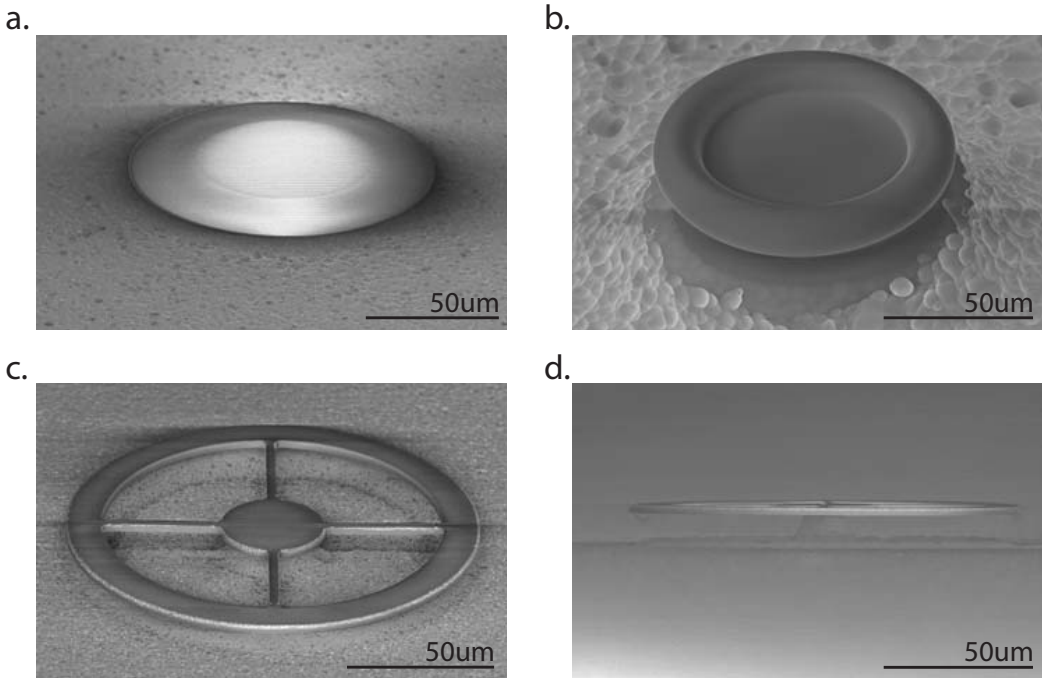

Figure 8.1: **Scanning electron microscope (SEM) images of resonators. a.** Disc resonator etched using HF. Wedge is created on the top side. **b.** Toroid resonator formed by heating disc resonator with CO_2 laser. **c.** Ring resonator etched using RIE. **d.** Side view of the ring resonator.

8.2.1 Wedged disk resonator

Among many whispering gallery resonators compatible with chip-scale process, we further investigate the wedged disk resonator offering high quality factor [75]. The fabrication procedure is a simple one-mask process as outlined in Fig. 3.18. The highest optical quality factor reported in wedged disk resonator is 875 million [75].

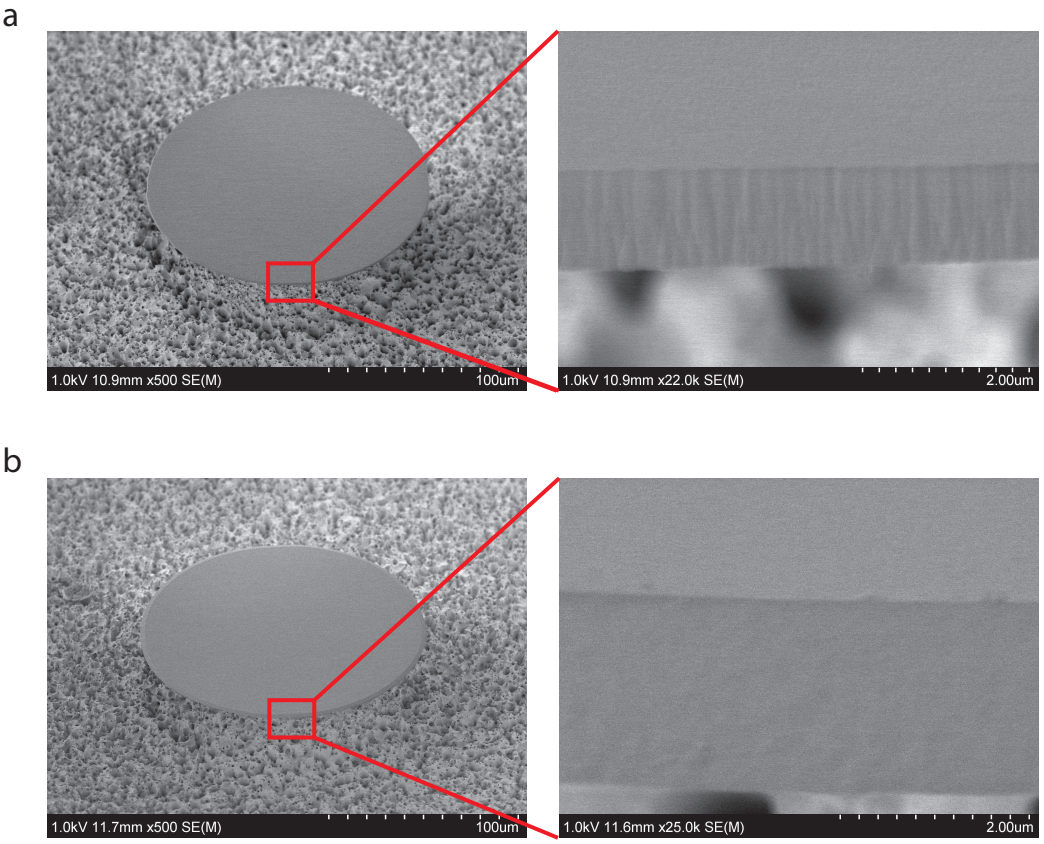

Figure 8.2: **a.** Disk resonator fabricated using deep-reactive-ion etching (DRIE) technique. As the disk is etched using DRIE, the side profile is vertical, but roughness is high. **b.** Wedged disk resonator fabricated using HF wet etching technique. As shown from profilometer measurement (Fig. 8.5), the side profile is slanted. However, wet-etching technique yields a smooth side wall.

The first on-chip whispering gallery resonator fabricated, however, was a disk resonator with a vertical sidewall as shown in Fig. 8.2a. Any anisotropic dry-etching technique can be used to create a vertical sidewall, but here, deep-reactive-ion etching (DRIE) with CF_4 and CHF_3 gases is used. The disk resonator can be integrated with the optical waveguide and coupler which are

defined simultaneously with the resonator. The optical modes within the disk resonator reside close to the outer edge making them accessible to waveguides patterned on the same layer. Due to the nature of etching process involving diffusion of etch gases, the sidewall is prone to having rough surfaces leading to lower quality factor. The surface roughness can be improved by optimizing etching parameters such as chamber pressure, gas mixture ratio, and plasma power. Others have reported smoothening of surfaces via annealing [264] and oxidation [265]. In order to enhance the surface roughness and to achieve higher quality factor, I fabricated wedged disk resonator using buffered oxide etch (BOE). Replacing dry etching with wet etching, the surface roughness is improved significantly.

As shown in Fig. 8.2b, the wedged disk resonator surface roughness can no longer be observed in scanning electron microscope (SEM). Thus, I am forced to use either transmission electron mircoscope (TEM) or atomic force microscope (AFM) which are able to achieve sub-nm level resolution. In this thesis, I used AFM surface characterization technique for its ability to output root-mean-square (RMS) roughness without relying on image analysis software and the ease of sample preparation before the surface scanning. Fig. 8.3a shows the AFM scan of wedged disk resonator surface after BOE etching. The RMS roughness of fabricated device is close to 0.1 nm well below what can be observed in the SEM images.

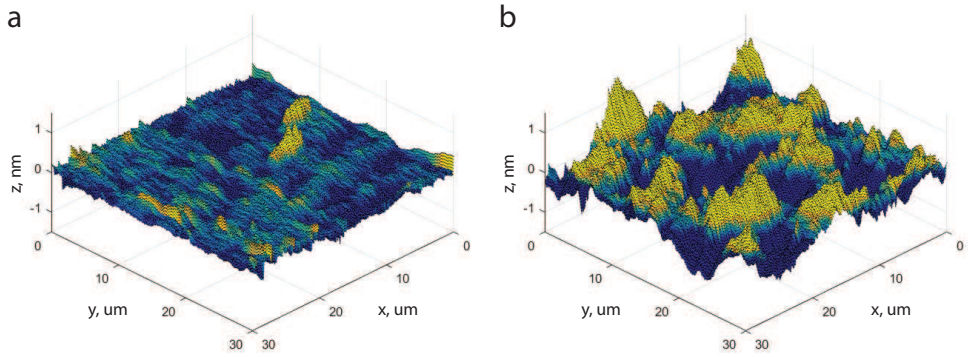

Figure 8.3: **a.** AFM scan of wedged resonator surface before releasing the disk via XeF_2 etching. The RMS roughness is 0.1001 nm. **b.** AFM scan of wedged resonator surface after releasing the disk via XeF_2 etching. The RMS roughness is now increased to 0.3357 nm.

As a result of BOE wet etching, the disk resonator has a slanted sidewell that resembles a wedge. The wet etching guarantees a smooth resonator

surface as shown in Fig. 8.2a and 8.3a. However, the wet etching results in a smaller resonator diameter compared to what was designed on the photomask which makes the on-chip waveguide implementation difficult, the problem we faced with the toroid resonator. Nevertheless, the wedge offers a profound advantage in regards to the optical confinement. As the optical mode is confined near the edge where the disk thickness reduces to a point (Fig. 8.4), we can make use of boundary effect that squeezes the optical and acoustic mode together for enhanced optomechanical coupling [76] which also leads to an increase in cooperativity [99].

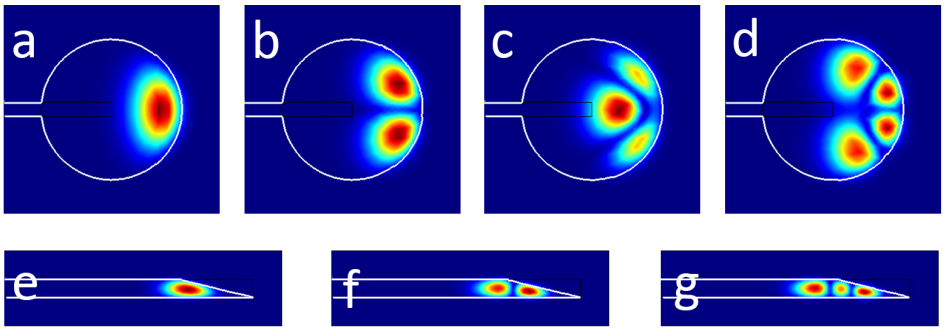

Figure 8.4: Various optical mode shapes in microtoroid and wedged disk resonators are simulated using COMSOL Multiphysics. Resonators diameter is ∼160 μm, optical wavelength is 1550 nm, and M-number (azimuthal order) is 468. **a.-d.** The optical modes within a microtoroid resonator. The modes are widely spread out across the axial direction. Torus diameter is 10 μm. Only small region near torus is shown here. **e.-g.** The optical modes within a wedged disk resonator. As the resonator thickness is less than the optical wavelength especially at the wedge, the geometry plays an important role in shaping the optical mode. Disk thickness is 1 μm.

8.3 Active optical device on-chip

In extension of on-chip resonator, active optical devices with piezo-electric interdigital transducer (IDT) are considered in this section. The goal is to deposit AlN piezo-electric film on top of SiO_2 where optical mode is confined and to pattern IDT for actuating an acoustic wave (Fig. 8.6). Such active optical device can modulate light and potentially support Brillouin scattering

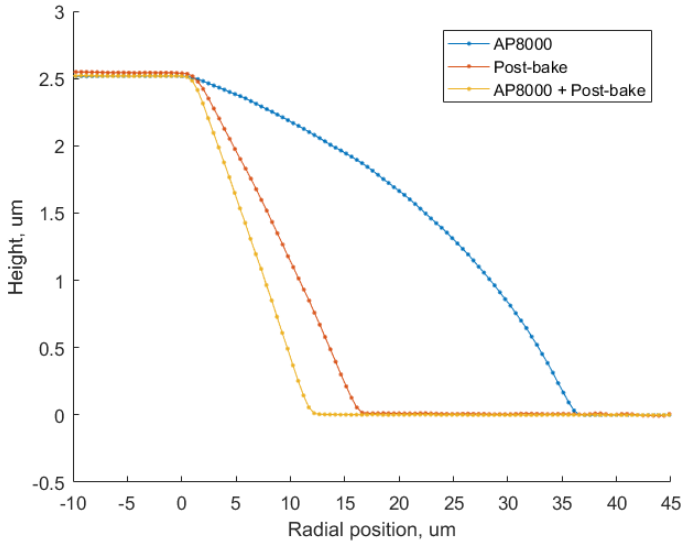

Figure 8.5: The wedge disk resonator geometry is measured using profilometer. During the fabrication, the resonator side profile is determined by the photoresist adhesion strength. Thus, enhancing the photoresist adhesion by using adhesion promoter (Dow Chemical AP8000) and post-baking process (3 min at 110 °C) helps to achieve sharper wedge angle. It is found that the post-baking contributes significantly to the adhesion of the photoresist during HF wet-etching process.

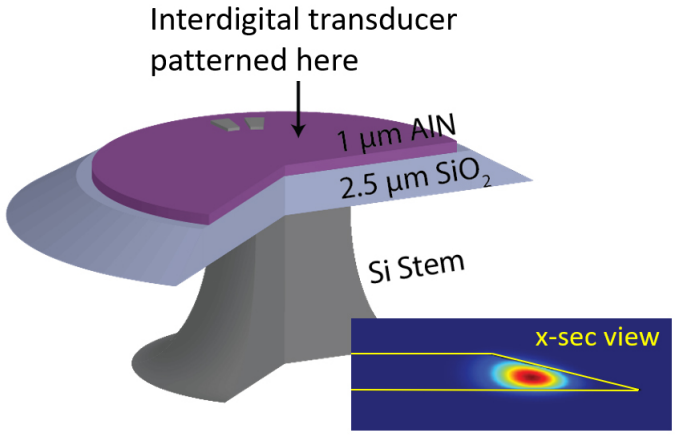

Figure 8.6: Rendered image of wedged disk resonator with piezo-electric interdigital transducer patterned on the top. (Inset) Simulation of optical mode confined within the wedge region. AlN has refractive index higher than SiO_2 and thus, must not reside near the optical mode.

with engineered optical mode pair satisfying the phase matching condition.

The fabrication process for wedged disk resonator with IDT is outlined in Fig. 8.7 (See Appendix. C for the detailed fabrication procedure). The

fabrication starts with Si wafer with thermal oxide. AlN is sputter coated. Al electrode and AlN disk layers are patterned first to reduce the chance of contaminating SiO_2 optical layer. Wedged disk resonator is patterned and etched using wet etching (buffered oxide etch). Then, Silicon substrate is etched using XeF_2 etcher to release the resonator preventing optical field leakage as Si has refractive index much higher than SiO_2. Scanning electron microscope images of fabricated device can be seen in Fig. 8.8.

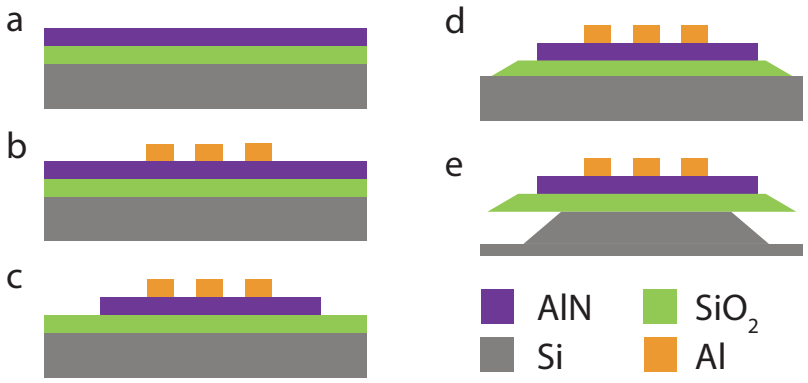

Figure 8.7: Fabrication process for wedged disk resonator with piezo-electric interdigital transducer.

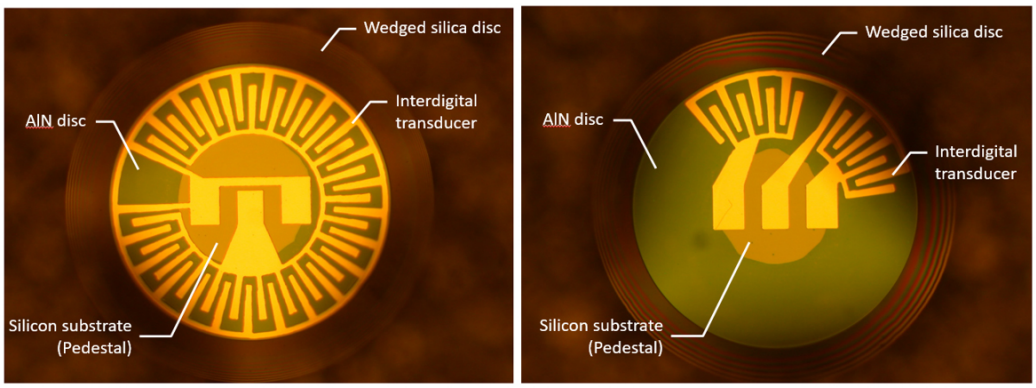

Figure 8.8: Scanning electron microscope image of fabricated devices. (Left) Resonator with IDT covering the entire disk. (Right) IDT covers only a small region on disk resonator. Also, two IDT sections are offset to create spatial phase difference and to actuate a traveling acoustic wave.

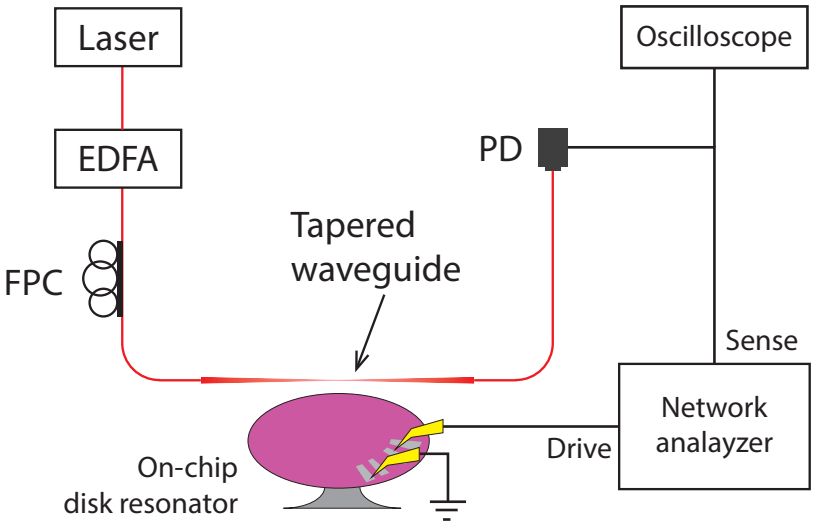

Figure 8.9: The disk resonator fabricated on-chip is tested on a probe station modified to implement tapered waveguide. The intracavity optical signal is modulated as a drive frequency is applied to the interdigital transducer actuating the acoustic wave. The photodetector (PD) then picks up the beat note between the laser input and modulated optical signals. Erbium doped fiber amplifier (EDFA) amplifies the optical signal and fiber polarization controller (FPC) prepares the polarization for efficient light coupling.

8.3.1 Characterization of on-chip disk resonator

We characterize the fabricated on-chip disk resonator to verify the feasibility for the demonstration of Brillouin scattering induced transparency in this device. For the experimental setup, we modify the commercial probe station to accept the tapered waveguide and set up the optical test bench as schematically shown in Fig. 8.9. Here, we monitor the optical transmission for characterizing the optical Quality factor and optical response to study optical modulation from interdigital transducer (IDT) using this setup.

As discussed in Ch. 7, the optical Quality factor is an important parameter that directly affects the optical isolation contrast in Brillouin scattering induced transparency system. Due to the nature of on-chip fabrication process, we fabricate tens or hundreds of resonators in a single fab-run. Thus, we first check the optical Quality factor to identify the resonators to be used in the experiment. At the two desired operating laser wavelengthes, the optical Quality factor is found to be 10^6 at 1550 nm and 5×10^5 at 780 nm as shown in Fig. 8.10. The difference in Quality factor is due to the absorption

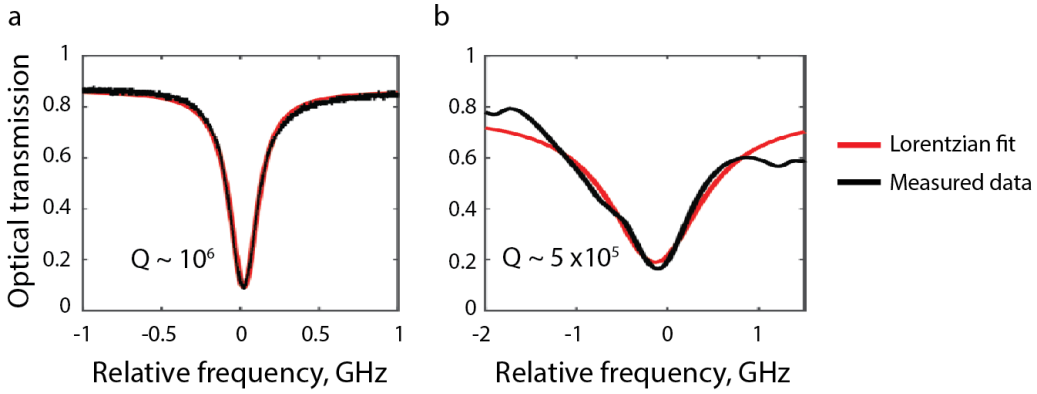

Figure 8.10: The optical quality factor of resonator fabricated on-chip is measured at **a.** 1550 nm and **b.** 780 nm laser wavelength.

coefficients at the respective laser wavelength.

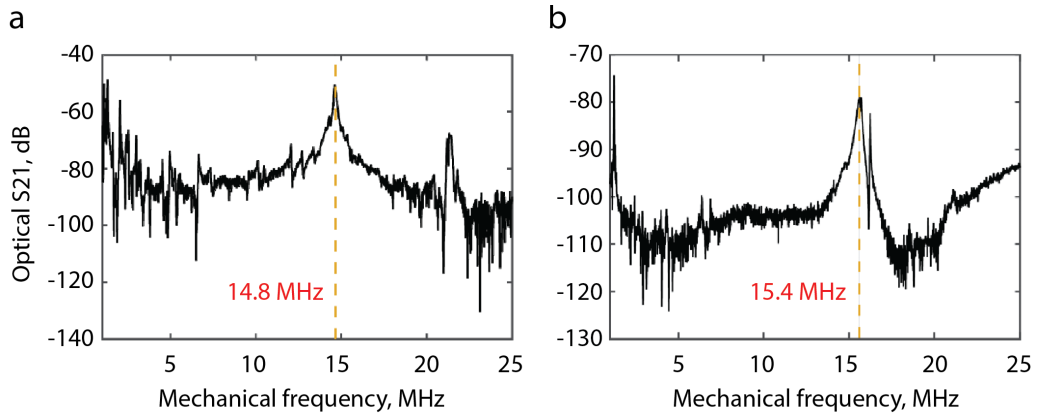

Figure 8.11: The optical response (S21) measured at **a.** 1550 nm and **b.** 780 nm laser wavelength. The mechanical spectrum can be inferred from the optical S21 as the mechanical vibration modulates the optical signal.

We then proceed to show the excitation of mechanical modes using interdigital transducer (IDT). While applying the RF stimulus to the IDT, we monitor the optical output to plot the optical S21 spectrum. The spectrum shows the device response from the electrical signal and validates that electrical to mechanical to optical transduction is taking place. The excitation of mechanical modes is an important step towards demonstration of Brillouin scattering induced transparency (BSIT) on-chip. However, we were not able to show BSIT quite yet due several factors. First of all, the optical and mechanical quality factors are not high enough to show noticeable transparency from the optical transmission. We attempted to overcome the low quality factor issue by driving the IDT with larger power, but have found that the

thin IDT strips are not able to withstand the thermal dissipation. Also, it is possible that the radiation pressure mechanical mode is being actuated instead of the necessary traveling acoustic mode.

8.4 Path to Brillouin scattering induced transparency and optical isolation on-chip

Before concluding this chapter, we shall briefly review previous demonstrations of Brillouin scattering on-chip to seek a path towards showing Brillouin scattering induced transparency (BSIT) and also, BSIT-based optical isolation technique on-chip. Brillouin scattering is of great interest especially for its capability to work as an extremely narrow linewidth optical source. Thus, many Brillouin scattering compatible micro- and nano-photonic devices were explored. Eggleton was one of the first to propose photonic circuit system entirely compatible with chip-scale process [167, 169, 176, 257]. These systems utilize high Brillouin gain material such as Chalcogenide to enhance the optical nonlinearity and device performance. This approach, however, is typically not suitable for resonator devices due to high absorption coefficients of many exotic materials.

Another approach is to engineer optical confinement and mechanical mode overlap to enhance Brillouin gain and nonlinear effects [170, 236, 266]. This method improves the optomechanical coupling and in turn, Brillouin scattering becomes more distinguished. Kittlaus et. al. demonstrated in a uniquely designed suspended waveguide structure that Brillouin gain can be significantly enhanced by modifying the device geometry [236]. Although it was demonstrated in a linear, non-resonant structure initially, we could implement this methodology in a suspended ring resonator or a racetrack resonator to attain similar benefits [267].

Separately, there are efforts to improve the quality factor and to approach the material limit set by the absorption coefficients [268, 269, 270]. With the improved etch recipe and resonator geometry, Quality factor of 800 million was demonstrated already [75]. More recently, 200 million Quality factor was demonstrated even with integrated waveguides that are fully capable of evanescent light coupling [268]. Even at this level, the improvement in Quality factor over the devices used in our earlier experiments.

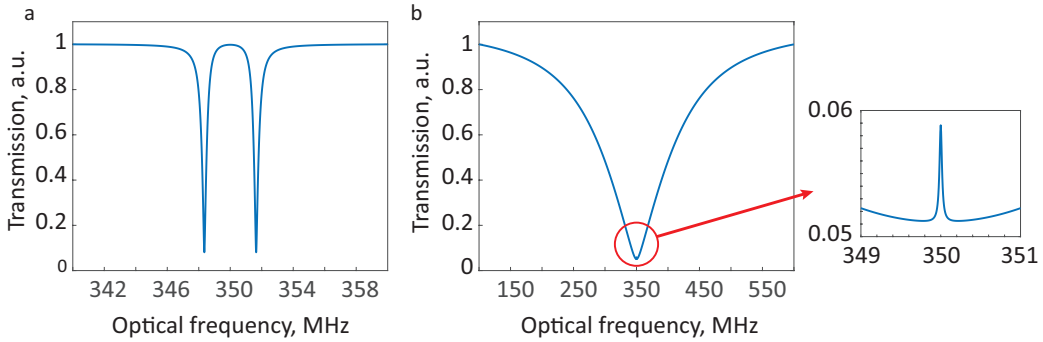

Figure 8.12: Estimated size of Brillouin scattering induced transparency (BSIT) for 200-fold difference in Quality factor **a.** BSIT with Quality factor of 200 million. **b.** BSIT with Quality factor of 1 million while the optomechanical coupling rate is kept identical. Inset shows the negligible induced transparency theoretically achievable (Note the axis range).

Recalling the Quality factor shown from the on-chip hybrid disk resonator device with integrated IDT, the difference in Quality factor from [268] is nearly $\times 200$. Such large difference in Quality factor directly affects the size of induced transparency. In essence, the induced transparency can be hidden entirely under the noise floor when the optical Quality factor is poor as shown in Fig. 8.12. Thus, we believe improving the resonator Quality factor will greatly improve the chance for observing Brillouin scattering induced transparency and optical isolation on-chip.

CHAPTER 9

CONCLUSION

In this thesis, we showed that Brillouin scattering acousto-optic interaction that is phase matched with a long-lived high-coherence phonon mode can lead to the induced transparency. The unique energy and momentum conservation (phase matching) requirement associated with Brillouin scattering and Brillouin scattering induced transparency (BSIT) process leads to the rapidly changing optical response which we interpret as the slow and fast light. From the literature survey, it is found that BSIT slow and fast light system outperforms the state-of-the-art SBS systems by five-orders of magnitude in terms of an engineering metric, delay-bandwidth per power per device size. These results prove that BSIT system is an ideal candidate for building non-reciprocal optical devices such as optical isolator and circulator especially on-chip.

There are several ways in which this work should be further pursued. First, the operating laser wavelength may be expanded. This experiment was carried out using a C-band laser (1530 to 1565 nm). However, the Brillouin scattering process is not limited to C-band nor infrared wavelength range. As there are optical applications that require operating wavelength of different wavelengths, further investigation of BSIT and optical isolation at different wavelength is planned.

Further, the operating bandwidth of the slow light and optical isolation is to be increased. The achieved bandwidth of 17 kHz has limited applications due to its inability to effectively process short pulses. To resolve this issue, several solutions are considered. Poulton et. al. demonstrated increased bandwidth in Brillouin scattering based frequency comb by engineering the dispersion line of the two optical fields to match in parallel, which theoretically allows the Brillouin phase matching to occur for all optical frequencies [175]. Also, frequency dithering of the control laser is known for increasing the bandwidth [271]. Frequency dithered input signal can excite

more than one acoustic mode at slightly different frequencies. In effect, the operating bandwidth will be increased.

Lastly, the slow and fast light and optical isolation experiment has to be further explored. The slow and fast light time is calculated based on the phase response of a probing optical signal. The experiment in which a pulse is sent and measured to show exactly how much delay can be achieved will give a concrete proof of the BSIT slow light system. Also, the optical isolation experiment where the light is sent from both direction simultaneously should be carried out. Although BSIT non-reciprocity and optical isolation is demonstrated here, an experiment where the probe is sent from both forward and backward direction may reveal if distortion or chirping can occur or not.

APPENDIX A

LORENTZ RECIPROCITY THEOREM

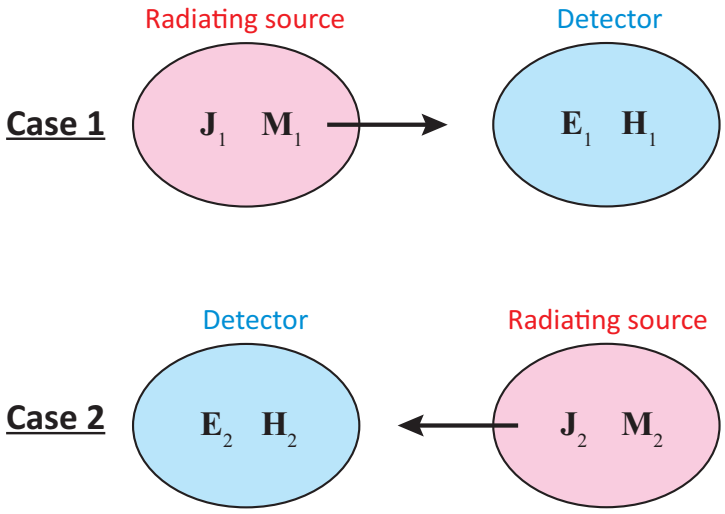

Figure A.1: Setup for Lorentz reciprocity

Here we derive Lorentz reciprocity relationship using radiating antenna example. This derivation and other reciprocity theorems can be found in [272].

Assume we have two electromagnetic radiation sources $\mathbf{J}_1$ and $\mathbf{J}_2$ with associated electric and magnetic components $\mathbf{E}_i$ and $\mathbf{H}_i$ defined as

$$\nabla \times \mathbf{E}_i = -\frac{\partial \mathbf{B}_i}{\partial t} = -j\omega\mu\mathbf{H}_i - \mathbf{M}_i \tag{A.1}$$

$$\nabla \times \mathbf{H}_i = \frac{\partial \mathbf{D}_i}{\partial t} + \mathbf{J}_i = j\omega\epsilon\mathbf{E}_i + \mathbf{J}_i \tag{A.2}$$

We then take the curl of poynting vectors to deduce the Lorentz reciprocity theorem.

$$\nabla \cdot (\mathbf{E}_1 \times \mathbf{H}_2 - \mathbf{E}_2 \times \mathbf{H}_1) \tag{A.3}$$

$$= (\nabla \times \mathbf{E}_1) \cdot \mathbf{H}_2 - \mathbf{E}_1 \cdot (\nabla \times \mathbf{H}_2) - (\nabla \times \mathbf{E}_2) \cdot \mathbf{H}_1 + \mathbf{E}_2 \cdot (\nabla \times \mathbf{H}_1) \tag{A.4}$$

$$= -\mathbf{M}_1 \cdot \mathbf{H}_2 - \mathbf{E}_1 \cdot \mathbf{J}_2 + \mathbf{M}_2 \cdot \mathbf{H}_1 + \mathbf{E}_2 \cdot \mathbf{J}_2 \tag{A.5}$$

Integrating the divergence over the volume of interest yields the most general form of Lorentz reciprocity equation

$$\oiint_S (\mathbf{E}_1 \times \mathbf{H}_2 - \mathbf{E}_2 \times \mathbf{H}_1) \cdot ds' = \iiint_V (-\mathbf{M}_1 \cdot \mathbf{H}_2 - \mathbf{E}_1 \cdot \mathbf{J}_2 + \mathbf{M}_2 \cdot \mathbf{H}_1 + \mathbf{E}_2 \cdot \mathbf{J}_1)\, dv' \tag{A.6}$$

In the antenna theory, the Poynting vector points radially outward and is normal to the sphere. Thus, we can simplify the epxression as

$$(\mathbf{E}_1 \times \mathbf{H}_2 - \mathbf{E}_2 \times \mathbf{H}_1) \cdot \hat{\mathbf{n}} dS = (\hat{\mathbf{n}} \times \mathbf{E}_1) \cdot \mathbf{H}_2 - (\hat{\mathbf{n}} \times \mathbf{E}_2) \cdot \mathbf{H}_1 \tag{A.7}$$

And since electric and magnetic fields are related through the expression $\mathbf{H} = (\hat{\mathbf{n}} \times \mathbf{E})/\eta$

$$\begin{aligned}(\mathbf{E}_1 \times \mathbf{H}_2 - \mathbf{E}_2 \times \mathbf{H}_1) \cdot \hat{\mathbf{n}} dS &= \eta \mathbf{H}_1 \cdot \mathbf{H}_2 - \eta \mathbf{H}_2 \cdot \mathbf{H}_1 \\ &= 0\end{aligned} \tag{A.8}$$

Therefore, the Lorentz reciprocity equation Eq. A.6 reduce to

$$\iiint_V (\mathbf{E}_1 \cdot \mathbf{J}_2 - \mathbf{M}_2 \cdot \mathbf{H}_1)\, dv' = \iiint_V (\mathbf{E}_2 \cdot \mathbf{J}_1 - \mathbf{M}_1 \cdot \mathbf{H}_2)\, dv' \tag{A.9}$$

In this equation, the LHS corresponds to the reaction of field $\mathbf{E}_1$ from the source $\mathbf{J}_2$ and the RHS corresponds to the reaction of field $\mathbf{E}_2$ from the source $\mathbf{J}_1$. Thus, replacing the source and detector positions does not modify the measurements.

APPENDIX B

DERIVATION OF BRILLOUIN SCATTERING INDUCED TRANSPARENCY USING HAMILTONIAN

The system of equations describing the intracavity fields in Brillouin scattering induced transparency (BSIT) can be derived classically as shown in Ch. 5.3.2. For better understanding of the system from quantum mechanical perspective, we provide the derivation using Hamiltonian of BSIT system.

The Hamiltonian for Brillouin scattering induced transparency is given by [10]

$$H = H_o + H_{int} + H_{input} \tag{B.1}$$

where H_o is the Hamiltonian for optical and acoustic modes, H_{int} is the interaction Hamiltonian, and H_{input} is the external input (source of excitation). Each Hamiltonian is expressed as

$$H_o = \omega_1 a_1^\dagger a_1 + \omega_2 a_2^\dagger a_2 + \Omega_m b^\dagger b \tag{B.2}$$

$$H_{int} = \beta a_1 a_2^\dagger b + \beta^* a_1^\dagger a_2 b^\dagger \tag{B.3}$$

$$\begin{aligned} H_{input} = {} & i\sqrt{k_{ex}}\left(a_1^\dagger S_{in,c}\exp^{-i\omega_c t} - a_1 S_{in,c}\exp^{i\omega_c t}\right) \\ & + i\sqrt{k_{ex}}\left(a_2^\dagger S_{in,p}\exp^{-i\omega_p t} - a_2 S_{in,p}\exp^{i\omega_p t}\right) \end{aligned} \tag{B.4}$$

where a ($a^\dagger$) and b ($b^\dagger$) are optical and acoustic modes bosonic annhilation (creation) operators respectively, ω is the optical mode frequency, Ω_m is the mechanical mode frequency, β is the optomechanical coupling, $k_e x$ is the waveguide-resonator coupling rate, and S_{in} is optical driving field (c = control field, p = probe field). In a frame rotating at the control laser frequency ω_c, the Hamiltonian for the Stokes mode can be written as

$$H_1 = \Delta_1 a_1^\dagger a_1 + H_{int} + \left(i\sqrt{k_{ex}} a_1^\dagger S_{in,c} + conj.\right) + \omega_2 a_2^\dagger + \Omega_k m b^\dagger b \tag{B.5}$$

Solving the above equation using the Heisenberg representation [98, 273]

$$\frac{d}{dt}A(t) = \frac{i}{\hbar}\left[H, A(t)\right] + \left(\frac{\partial A(t)}{\partial t}\right)_H \tag{B.6}$$

we can find the expression for the intracavity control field

$$\dot{a_1} = i\Delta_1 a_1 - \frac{\kappa}{2}a_1 - i\beta^* a_2 b^\dagger + \sqrt{\kappa_{ex}}S_{in,c} \tag{B.7}$$

Carrying out the same calculation for the probe and acoustic field, we can find the complete system of equation

$$\dot{a_1} = i\Delta_2 a_2 - \frac{\kappa}{2}a_2 - i\beta^* a_1 b + \sqrt{\kappa_{ex}}S_{in,p} \tag{B.8}$$

$$\dot{b} = i\Delta_B u - \frac{\Gamma_B}{2}b - i\beta^* a_1^\dagger a_2 \tag{B.9}$$

The result is identical to the classical derivation [195].

APPENDIX C

ON-CHIP RESONATOR FABRICATION PROCEDURE

All microfabricated devices presented in this thesis are fabricated using cleanroom facility at University of Illinois at Urbana-Champaign Micro and Nanotechnology Lab. Fabrication procedure presented below thus is not optimized for other cleanroom facilities and equipment. Some machine parameters may need to be modified.

C.1 On-chip silica disk fabrication procedure

1. If starting with old sample, prepare clean substrate by performing either
   - Resist stripping in PG remover >10min at 70°C
   - Piranha cleaning >10min
2. Acetone - IPA - DI - IPA - N2 dry
3. Dehydration bake 2min at 110°C
4. O2 descum 3min at 500W
5. Apply HMDS and wait >10sec then spin 30sec at 3000rpm, bake 2min at 110°C
6. Spin SPR220 30sec at 3000rpm
7. Softbake 2min at 110°C
8. Expose disc pattern
9. Post-exposure bake 1min at 110°C

10. Develop in 4:1 = DI:AZ400K solution (Note: AZ400K is not compatible with AlN)
11. Remove edge bead using a swab and acetone
12. O2 descum 1min at 250W
13. Hardbake 2min at 110°C
14. BOE etch 1hr for 2.5um silica or longer for thicker silica (∼1.6hr for 4um)
15. Examine to make sure the exposed silicon substrate is hydrophobic (repels water)
16. Resist stripping in PG remover for ¿5min
17. Acetone - IPA - DI - IPA - N2 dry
18. Dehydration bake 2min at 110°C
19. XeF2 etching (Etching 140um horizontally for 2 of 1cm x 1cm chips requires 70 cycles)

C.2 On-chip silica/AlN disk with electrode fabrication procedure

Pattern Aluminum Top Electrode

1. If starting with old sample, prepare clean substrate by performing either
    - Resist stripping in PG remover >10min at 70°C
    - Piranha cleaning >10min
2. Acetone - IPA - DI - IPA - N2 dry
3. Dehydration bake 2min at 110°C

4. O2 descum 3min at 500W
5. (Optional) Apply HMDS and wait >10sec then spin 30sec at 3000rpm, bake 2min at 110°C
6. Spin AZ1813 30sec at 3000rpm
7. Softbake 2min at 110°C
8. Expose top electrode pattern
9. Develop in 1:1 = DI:Microposit developer solution (Note: Do NOT use AZ400K)
10. O2 descum 1min at 250W
11. Sputter 50nm aluminum
12. Lift off aluminum in PG remover

Pattern AlN Layer (Option 1: By dry etching)

1. Acetone - IPA - DI - IPA - N2 dry
2. Dehydration bake 2min at 110°C
3. O2 descum 3min at 500W
4. Apply HMDS and wait >10sec then spin 30sec at 3000rpm, bake 2min at 110°C
5. Spin SPR220 30sec at 3000rpm
6. Softbake 2min at 110°C
7. Expose AlN disc pattern
8. Post-exposure bake 1min at 110°C
9. Develop in 1:1 = DI:Microposit developer solution (Note: Do NOT use AZ400K)
10. O2 descum 1min at 250W

11. Hardbake 2min at 110°C
12. Etch AlN layer in Oxford RIE
13. Resist stripping in PG remover for >5min

Pattern AlN Layer (Option 2: By wet etching)

1. Acetone - IPA - DI - IPA - N2 dry
2. Dehydration bake 2min at 110°C
3. O2 descum 3min at 500W
4. Sputter copper
5. Spin SPR220 30sec at 3000rpm
6. Softbake 2min at 110°C
7. Exposde AlN disc pattern
8. Post-exposure bake 1min at 110°C
9. Develop in 1:1 = DI:Mircoposit developer solution
10. O2 descum 1min at 250W
11. Hardbake 2min at 110°C
12. Etch copper layer in copper etchant (Need AlN- or Al-compatible copper etchant)
13. Acetone - IPA - DI - IPA - N2 dry
14. Etch AlN layer in AZ400K or other AlN etchant
15. Etch copper layer in copper etchant

Pattern Silica Layer

1. Acetone - IPA - DI - IPA - N2 dry

2. Dehydration bake 2min at 110°C
3. O2 descum 3min at 500W
4. Apply HMDS and wait >10sec then spin 30sec at 3000rpm, bake 2min at 110°C
5. Spin SPR220 30sec at 3000rpm
6. Softbake 2min at 110°C
7. Expose disc pattern
8. Post-exposure bake 1min at 110°C
9. Develop in 1:1 = DI:Microposit developer solution (Note: Do NOT use AZ400K)
10. Remove edge bead using a swab and acetone
11. O2 descum 1min at 250W
12. Hardbake 2min at 110°C
13. BOE etch 1hr for 2.5um silica or longer for thicker silica (∼1.6hr for 4um)
14. Examine to make sure the exposed silicon substrate is hydrophobic (repels water) and repeat BOE etch until silicon is exposed.
15. Resist stripping in PG remover for >5min
16. Acetone - IPA - DI - IPA - N2 dry
17. Dehydration bake 2min at 110°C
18. XeF2 etching (Etching 140um horizontally for 2 of 1cm x 1cm chips requires ∼70 cycles)

REFERENCES

[1] H. A. MacLeod, *Thin-Film Optical Filters*, 3rd ed. CRC Press, 2001.

[2] J. W. S. Baron Rayleigh, "On the intensity of light reflected from certain surfaces at nearly perpendicular incidence," *Proceedings of the Royal Society of London*, vol. 41, pp. 275–294, 1887.

[3] C. L. Hogan, "The Ferromagnetic Faraday Effect at Microwave Frequencies and its Applications," *Rev. Mod. Phys.*, vol. 25, pp. 253–262, Jan 1953.

[4] J. E. Geusic and H. E. D. Scovil, "A unidirectional traveling-wave optical maser," *The Bell System Technical Journal*, vol. 41, no. 4, pp. 1371–1397, July 1962.

[5] C. L. Hogan, "The Elements of Nonreciprocal Microwave Devices," *Proceedings of the IRE*, vol. 44, no. 10, pp. 1345–1368, Oct 1956.

[6] L. J. Aplet and J. W. Carson, "A Faraday Effect Optical Isolator," *Appl. Opt.*, vol. 3, no. 4, pp. 544–545, Apr 1964.

[7] P. C. Fletcher and D. L. Weisman, "Circulators for Optical Radar Systems," *Appl. Opt.*, vol. 4, no. 7, pp. 867–873, Jul 1965.

[8] W. B. Ribbens, "An Optical Circulator," *Appl. Opt.*, vol. 4, no. 8, pp. 1037–1038, Aug 1965.

[9] H. Lira, Z. Yu, S. Fan, and M. Lipson, "Electrically Driven Nonreciprocity Induced by Interband Photonic Transition on a Silicon Chip," *Phys. Rev. Lett.*, vol. 109, no. 3, p. 033901, July 2012.

[10] C.-H. Dong, Z. Shen, C.-L. Zou, Y.-L. Zhang, W. Fu, and G.-C. Guo, "Brillouin-scattering-induced transparency and non-reciprocal light storage," *Nature Communications*, vol. 6, p. 6193, Feb. 2015.

[11] Z. Shen, Y.-L. Zhang, Y. Chen, C.-L. Zou, Y.-F. Xiao, X.-B. Zou, F.-W. Sun, G.-C. Guo, and C.-H. Dong, "Experimental realization of optomechanically induced non-reciprocity," *Nature Photon.*, vol. 10, pp. 657–661, Aug. 2016.

[12] B. Peng, Ş. K. Özdemir, F. Lei, F. Monifi, M. Gianfreda, G. L. Long, S. Fan, F. Nori, C. M. Bender, and L. Yang, "Parity–time-symmetric whispering-gallery microcavities," *Nature Phys.*, vol. 10, no. 5, pp. 394–398, Apr. 2014.

[13] L. D. Tzuang, K. Fang, P. Nussenzveig, S. Fan, and M. Lipson, "Non-reciprocal phase shift induced by an effective magnetic flux for light," *Nature Photon.*, vol. 8, no. 9, pp. 701–705, Sep. 2014.

[14] C. Sayrin, C. Junge, R. Mitsch, B. Albrecht, D. O'Shea, P. Schneeweiss, J. Volz, and A. Rauschenbeutel, "Nanophotonic Optical Isolator Controlled by the Internal State of Cold Atoms," *Phys. Rev. X*, vol. 5, no. 4, p. 041036, Dec. 2015.

[15] M. S. Kang, A. Butsch, and P. S. J. Russell, "Reconfigurable light-driven opto-acoustic isolators in photonic crystal fibre," *Nat Photon*, vol. 5, no. 9, pp. 549–553, Sep. 2011.

[16] Y. Shoji, T. Mizumoto, H. Yokoi, I.-W. Hsieh, and R. M. Osgood, "Magneto-optical isolator with silicon waveguides fabricated by direct bonding," *Appl. Phys. Lett.*, vol. 92, no. 7, 2008.

[17] J. Ballato and E. Snitzer, "Fabrication of fibers with high rare-earth concentrations for Faraday isolator applications," *Appl. Optics*, vol. 34, no. 30, pp. 6848–6854, Oct 1995.

[18] T. Goto, M. C. Onbaşli, and C. A. Ross, "Magneto-optical properties of cerium substituted yttrium iron garnet films with reduced thermal budget for monolithic photonic integrated circuits," *Opt. Express*, vol. 20, no. 27, pp. 28 507–28 517, Dec 2012.

[19] K. J. Boller, A. Imamolu, and S. Harris, "Observation of electromagnetically induced transparency," *Phys. Rev. Lett.*, vol. 66, no. 20, pp. 2593–2596, May 1991.

[20] L. V. Hau, S. E. Harris, Z. Dutton, and C. H. Behroozi, "Light speed reduction to 17 metres per second in an ultracold atomic gas," *Nature*, vol. 397, no. 6720, pp. 594–598, 1999.

[21] M. Fleischhauer, A. Imamoglu, and J. P. Marangos, "Electromagnetically induced transparency: Optics in coherent media," *Rev. Mod. Phys.*, vol. 77, pp. 633–673, Jul 2005.

[22] J. Kim, M. C. Kuzyk, K. Han, H. Wang, and G. Bahl, "Non-reciprocal Brillouin scattering induced transparency," *Nature Physics*, vol. 11, p. 275, Jan. 2015.

[23] J. Kim, S. Kim, and G. Bahl, "Complete linear optical isolation at the microscale with ultralow loss," *Scientific Reports*, vol. 7, no. 1, p. 1647, May 2017.

[24] G. Green, *An Essay on the Mathematical Analysis of Electricity and Magnetism*. Nottingham, 1828.

[25] H. Helmholtz, "Theorie der Luftschwingungen in Röhren mit offenen Enden." *Journal für die reine und angewandte Mathematik*, no. 57, pp. 1–20, 1959.

[26] A. Clebsch, *Théorie de l'Elasticité des Corps Solides*. Leipzig, 1862.

[27] J. C. Maxwell, "On the calculation of the equilibrium and stiffness of frames," *The London, Edinburgh, and Dublin Philosophical Magazine and Journal of Science*, vol. 27, no. 182, pp. 294–299, 1864.

[28] J. W. S. Baron Rayleigh, *The theory of sound*. Macmillan, 1894.

[29] H. A. Lorentz, "het theorema van Poynting over energie in het electromagnetisch veld en een paar algemeene stellingen over de voorplanting van het licht," *Vers. Konig. Akad. Wetensch.*, vol. 4, no. 176, 1896.

[30] J. R. Carson, "A generalization of the Reciprocal Theorem," *The Bell System Technical Journal*, vol. 3, no. 3, pp. 393–399, July 1924.

[31] G. S. Smith, "A direct derivation of a single-antenna reciprocity relation for the time domain," *IEEE Transactions on Antennas and Propagation*, vol. 52, no. 6, pp. 1568–1577, June 2004.

[32] M. Faraday, *Faraday's Diary of Experimental Investigation*, T. Martin, Ed. HR Direct, 2008.

[33] P. V. Wright, "The Natural Single-Phase Unidirectional Transducer: A New Low-Loss SAW Transducer," in *IEEE 1985 Ultrasonics Symposium*, Oct 1985, pp. 58–63.

[34] S. Trillo and S. Wabnitz, "Nonlinear nonreciprocity in a coherent mismatched directional coupler," *Applied Physics Letters*, vol. 49, no. 13, pp. 752–754, 1986.

[35] S. Lepri and G. Casati, "Asymmetric Wave Propagation in Nonlinear Systems," *Phys. Rev. Lett.*, vol. 106, p. 164101, Apr 2011.

[36] A. M. Mahmoud, A. R. Davoyan, and N. Engheta, "All-passive nonreciprocal metastructure," *Nature Communications*, vol. 6, p. 8359, Sep. 2015.

[37] B. Luo, S. Gao, J. Liu, Y. Mao, Y. Li, and X. Liu, "Non-reciprocal wave propagation in one-dimensional nonlinear periodic structures," *AIP Advances*, vol. 8, no. 1, p. 015113, 2018.

[38] G. Wu, Y. Long, and J. Ren, "Asymmetric nonlinear system is not sufficient for a nonreciprocal wave diode," *Phys. Rev. B*, vol. 97, p. 205423, May 2018.

[39] Y. Shi, Z. Yu, and S. Fan, "Limitations of nonlinear optical isolators due to dynamic reciprocity," *Nature Photon.*, vol. 9, no. 6, pp. 388–392, May 2015.

[40] A. Kord, D. L. Sounas, and A. Alù, "Pseudo-Linear Time-Invariant Magnetless Circulators Based on Differential Spatiotemporal Modulation of Resonant Junctions," *IEEE Transactions on Microwave Theory and Techniques*, vol. 66, no. 6, pp. 2731–2745, June 2018.

[41] R. Fleury, D. L. Sounas, C. F. Sieck, M. R. Haberman, and A. Alù, "Sound Isolation and Giant Linear Nonreciprocity in a Compact Acoustic Circulator," *Science*, vol. 343, no. 6170, pp. 516–519, 2014.

[42] A. Maznev, A. Every, and O. Wright, "Reciprocity in reflection and transmission: What is a 'phonon diode'?" *Wave Motion*, vol. 50, no. 4, pp. 776 – 784, 2013.

[43] E. Prati, "Propagation in gyroelectromagnetic guiding systems," *Journal of Electromagnetic Waves and Applications*, vol. 17, no. 8, pp. 1177–1196, Jan. 2003.

[44] O. Slezák, R. Yasuhara, A. Lucianetti, and T. Mocek, "Temperature-wavelength dependence of terbium gallium garnet ceramics Verdet constant," *Opt. Mater. Express*, vol. 6, no. 11, pp. 3683–3691, Nov 2016.

[45] A. Miles, Y. Gai, P. Gangopadhyay, X. Wang, R. A. Norwood, and J. J. Watkins, "Improving Faraday rotation performance with block copolymer and FePt nanoparticle magneto-optical composite," *Opt. Mater. Express*, vol. 7, no. 6, pp. 2126–2140, June 2017.

[46] V. Doormann, J. Krumme, and H. Lenz, "Optical and magneto-optical tensor spectra of bismuth-substituted yttrium-iron-garnet films," *Journal of Applied Physics*, vol. 68, no. 7, pp. 3544–3553, 1990.

[47] L. Bi, J. Hu, P. Jiang, D. H. Kim, G. F. Dionne, L. C. Kimerling, and C. A. Ross, "On-chip optical isolation in monolithically integrated non-reciprocal optical resonators," *Nature Photon.*, vol. 5, no. 12, pp. 758–762, Dec. 2011.

[48] M. Levy, "The on-chip integration of magnetooptic waveguide isolators," *IEEE Journal of Selected Topics in Quantum Electronics*, vol. 8, no. 6, pp. 1300–1306, Nov 2002.

[49] S. Ghosh, S. Keyvavinia, W. Van Roy, T. Mizumoto, G. Roelkens, and R. Baets, "Ce:YIG/Silicon-on-Insulator waveguide optical isolator realized by adhesive bonding," *Opt. Express*, vol. 20, no. 2, pp. 1839–1848, Jan. 2012.

[50] B. M. Garraway and H. Perrin, "Recent developments in trapping and manipulation of atoms with adiabatic potentials," *Journal of Physics B: Atomic, Molecular and Optical Physics*, vol. 49, no. 17, p. 172001, Aug. 2016.

[51] D. Sarkisyan, A. Papoyan, T. S. Varzhapetyan, K. Blush, and M. Auzinsh, "Zeeman effect on the hyperfine structure of the D1 line of a submicron layer of 87Rb vapor," *Optics and Spectroscopy*, vol. 96, pp. 328–334, May 2004.

[52] A. N. Oraevsky, "Whispering-gallery waves," *Quantum Electronics*, vol. 32, no. 5, p. 377, 2002.

[53] A. Khelif, A. Choujaa, S. Benchabane, B. Djafari-Rouhani, and V. Laude, "Guiding and bending of acoustic waves in highly confined phononic crystal waveguides," *Applied Physics Letters*, vol. 84, no. 22, pp. 4400–4402, 2004.

[54] S. Yang, J. H. Page, Z. Liu, M. L. Cowan, C. T. Chan, and P. Sheng, "Focusing of Sound in a 3D Phononic Crystal," *Phys. Rev. Lett.*, vol. 93, p. 024301, Jul 2004.

[55] R. H. Olsson III and I. El-Kady, "Microfabricated phononic crystal devices and applications," *Measurement Science and Technology*, vol. 20, no. 1, p. 012002, Nov. 2008.

[56] J. Li and C. T. Chan, "Double-negative acoustic metamaterial," *Phys. Rev. E*, vol. 70, p. 055602, Nov 2004.

[57] Z. Yang, J. Mei, M. Yang, N. H. Chan, and P. Sheng, "Membrane-Type Acoustic Metamaterial with Negative Dynamic Mass," *Phys. Rev. Lett.*, vol. 101, p. 204301, Nov 2008.

[58] T. Brunet, A. Merlin, B. Mascaro, K. Zimny, J. Leng, O. Poncelet, C. Aristégui, and O. Mondain-Monval, "Soft 3D acoustic metamaterial with negative index," *Nature Materials*, vol. 14, p. 384, Dec. 2014.

[59] N. Kaina, F. Lemoult, M. Fink, and G. Lerosey, "Negative refractive index and acoustic superlens from multiple scattering in single negative metamaterials," *Nature*, vol. 525, p. 77, Sep. 2015.

[60] Y. Ohmachi and J. Noda, "LiNbO3TE-TM mode converter using collinear acoustooptic interaction," *IEEE Journal of Quantum Electronics*, vol. 13, no. 2, pp. 43–46, Feb. 1977.

[61] V. Tournat, V. E. Gusev, V. Y. Zaitsev, and B. Castagnède, "Acoustic second-harmonic generation with shear to longitudinal mode conversion in granular media," *Europhysics Letters (EPL)*, vol. 66, no. 6, pp. 798–804, June 2004.

[62] Y. Cheng, F. Yang, J. Y. Xu, and X. J. Liu, "A multilayer structured acoustic cloak with homogeneous isotropic materials," *Applied Physics Letters*, vol. 92, no. 15, p. 151913, 2008.

[63] M. Farhat, S. Enoch, S. Guenneau, and A. B. Movchan, "Broadband Cylindrical Acoustic Cloak for Linear Surface Waves in a Fluid," *Phys. Rev. Lett.*, vol. 101, p. 134501, Sep 2008.

[64] S. Zhang, C. Xia, and N. Fang, "Broadband Acoustic Cloak for Ultrasound Waves," *Phys. Rev. Lett.*, vol. 106, p. 024301, Jan 2011.

[65] D. L. Sounas and A. Alu, "Angular-Momentum-Biased Nanorings To Realize Magnetic-Free Integrated Optical Isolation," *ACS Photonics*, vol. 1, no. 3, pp. 198–204, Mar. 2014.

[66] R. P. kenny, T. A. Birks, and K. P. Oakley, "Control of optical fibre taper shape," *Electronics Letters*, vol. 27, no. 18, pp. 1654–1656, 1991.

[67] J. Zhu, J. Christensen, J. Jung, L. Martin-Moreno, X. Yin, L. Fok, X. Zhang, and F. J. Garcia-Vidal, "A holey-structured metamaterial for acoustic deep-subwavelength imaging," *Nature Physics*, vol. 7, p. 52, Nov. 2010.

[68] L. V. Wang and S. Hu, "Photoacoustic Tomography: In Vivo Imaging from Organelles to Organs," *Science*, vol. 335, no. 6075, pp. 1458–1462, 2012.

[69] K. Pu, A. J. Shuhendler, J. V. Jokerst, J. Mei, S. S. Gambhir, Z. Bao, and J. Rao, "Semiconducting polymer nanoparticles as photoacoustic molecular imaging probes in living mice," *Nature Nanotechnology*, vol. 9, p. 233, Jan. 2014.

[70] T. O. Rocheleau, T. L. Naing, Z. Ren, and C. T. . Nguyen, "Acoustic whispering gallery mode resonator with Q > 109,000 at 515MHz," in *2012 IEEE 25th International Conference on Micro Electro Mechanical Systems (MEMS)*, Jan 2012, pp. 672–675.

[71] S. Mezil, K. Fujita, P. H. Otsuka, M. Tomoda, M. Clark, O. B. Wright, and O. Matsuda, "Active chiral control of GHz acoustic whispering-gallery modes," *Applied Physics Letters*, vol. 111, no. 14, p. 144103, 2017.

[72] J. Su, "Label-Free Biological and Chemical Sensing Using Whispering Gallery Mode Optical Resonators: Past, Present, and Future," *Sensors*, vol. 17, no. 3, 2017.

[73] F. Li, M. Xuan, Y. Wu, and F. Bastien, "Acoustic whispering gallery mode coupling with Lamb waves in liquid," *Sensors and Actuators A: Physical*, vol. 189, pp. 335–338, Jan. 2013.

[74] Y. Wu and F. Vollmer, *Whispering Gallery Mode Biomolecular Sensors*, 1st ed., G. Gagliardi and H.-P. Loock, Eds. Springer-Verlag Berlin Heidelberg, 2014.

[75] H. Lee, T. Chen, J. Li, K. Y. Yang, S. Jeon, O. Painter, and K. J. Vahala, "Chemically etched ultrahigh-Q wedge-resonator on a silicon chip," *Nat. Photon.*, vol. 6, no. 6, pp. 369–373, June 2012.

[76] N. Dostart, S. Kim, and G. Bahl, "Giant gain enhancement in surface-confined resonant stimulated Brillouin scattering," *Laser Photonics Rev.*, vol. 9, no. 6, pp. 689–705, 2015.

[77] K. Han, K. Zhu, and G. Bahl, "Opto-mechano-fluidic viscometer," *Applied Physics Letters*, vol. 105, no. 1, p. 014103, 2014.

[78] K. Han, J. Kim, and G. Bahl, "High-throughput sensing of freely flowing particles with optomechanofluidics," *Optica*, vol. 3, no. 6, pp. 585–591, June 2016.

[79] L. E. Kinsler, A. R. Frey, A. B. Coppens, and J. V. Sanders, *Fundamentals of Acoustics*. John Wiley & Sons, 2000.

[80] C. V. Raman and G. A. Sutherland, "On the Whispering-Gallery phenomenon," *Proceedings of the Royal Society of London. Series A, Containing Papers of a Mathematical and Physical Character*, vol. 100, no. 705, pp. 424–428, Apr. 1922.

[81] N. Konishi, T. Suzuki, Y. Taira, H. Kato, and T. Kasuya, "High precision wavelength meter with Fabry-Perot optics," *Applied Physics*, vol. 25, no. 3, pp. 311–316, Jul 1981.

[82] R. . Yan, R. J. Simes, and L. A. Coldren, "Analysis and design of surface-normal Fabry-Perot electrooptic modulators," *IEEE Journal of Quantum Electronics*, vol. 25, no. 11, pp. 2272–2280, Nov 1989.

[83] M. Y. Liu and S. Y. Chou, "High-modulation-depth and short-cavity-length silicon Fabry–Perot modulator with two grating Bragg reflectors," *Applied Physics Letters*, vol. 68, no. 2, pp. 170–172, 1996.

[84] A. Spisser, R. Ledantec, C. Seassal, J. L. Leclercq, T. Benyattou, D. Rondi, R. Blondeau, G. Guillot, and P. Viktorovitch, "Highly selective and widely tunable 1.55-um InP/air-gap micromachined Fabry-Perot filter for optical communications," *IEEE Photonics Technology Letters*, vol. 10, no. 9, pp. 1259–1261, 1988.

[85] J. S. Patel, M. A. Saifi, D. W. Berreman, C. Lin, N. Andreadakis, and S. D. Lee, "Electrically tunable optical filter for infrared wavelength using liquid crystals in a Fabry–Perot étalon," *Applied Physics Letters*, vol. 57, no. 17, pp. 1718–1720, 1990.

[86] A. D. Kersey, T. A. Berkoff, and W. W. Morey, "Multiplexed fiber Bragg grating strain-sensor system with a fiber Fabry-Perot wavelength filter," *Opt. Lett.*, vol. 18, no. 16, pp. 1370–1372, Aug. 1993.

[87] A. Mazzei, S. Götzinger, L. de S. Menezes, G. Zumofen, O. Benson, and V. Sandoghdar, "Controlled Coupling of Counterpropagating Whispering-Gallery Modes by a Single Rayleigh Scatterer: A Classical Problem in a Quantum Optical Light," *Phys. Rev. Lett.*, vol. 99, p. 173603, Oct 2007.

[88] D. V. Strekalov, C. Marquardt, A. B. Matsko, H. G. L. Schwefel, and G. Leuchs, "Nonlinear and quantum optics with whispering gallery resonators," *Journal of Optics*, vol. 18, no. 12, p. 123002, Nov. 2016.

[89] W. von Klitzing, R. Long, V. S. Ilchenko, J. Hare, and V. Lefèvre-Seguin, "Frequency tuning of the whispering-gallery modes of silica microspheres for cavity quantum electrodynamics and spectroscopy," *Opt. Lett.*, vol. 26, no. 3, pp. 166–168, Feb. 2001.

[90] H. Mabuchi and A. C. Doherty, "Cavity Quantum Electrodynamics: Coherence in Context," *Science*, vol. 298, no. 5597, pp. 1372–1377, 2002.

[91] S. M. Spillane, T. J. Kippenberg, K. J. Vahala, K. W. Goh, E. Wilcut, and H. J. Kimble, "Ultrahigh-Q toroidal microresonators for cavity quantum electrodynamics," *Phys. Rev. A*, vol. 71, p. 013817, Jan. 2005.

[92] F. Liu and M. Hossein-Zadeh, "Mass Sensing With Optomechanical Oscillation," *Sensors Journal, IEEE*, vol. 13, no. 1, pp. 146–147, 2013.

[93] J. Suh, K. Han, C. W. Peterson, and G. Bahl, "Real-time sensing of flowing nanoparticles with electro-opto-mechanics," *APL Photonics*, vol. 2, no. 1, p. 010801, Oct. 2018.

[94] J. Niehusmann, A. Vörckel, P. H. Bolivar, T. Wahlbrink, W. Henschel, and H. Kurz, "Ultrahigh-quality-factor silicon-on-insulator microring resonator," *Opt. Lett.*, vol. 29, no. 24, pp. 2861–2863, Dec 2004.

[95] M. Gorodetsky and V. S. Ilchenko, "Optical microsphere resonators: optimal coupling to high-Q whispering-gallery modes," *Journal of the Optical Society of America B*, vol. 16, no. 1, pp. 147–154, 1999.

[96] R. Kitamura, L. Pilon, and M. Jonasz, "Optical constants of silica glass from extreme ultraviolet to far infrared at near room temperature," *Appl. Opt.*, vol. 46, no. 33, pp. 8118–8133, Nov. 2007.

[97] M. L. Gorodetsky, A. A. Savchenkov, and V. S. Ilchenko, "Ultimate Q of optical microsphere resonators," *Opt. Lett.*, vol. 21, no. 7, pp. 453–455, Apr. 1996.

[98] D. F. Walls and G. J. Milburn, *Quantum Optics*, 2nd ed. Springer, 2008.

[99] M. Aspelmeyer, T. J. Kippenberg, and F. Marquardt, *Cavity Optomechanics*. Springer, 2014.

[100] G. Bahl, M. Tomes, F. Marquardt, and T. Carmon, "Observation of spontaneous Brillouin cooling," *Nature Physics*, vol. 8, no. 3, pp. 203–207, Mar. 2012.

[101] S. Weis, R. Rivière, S. Deléglise, E. Gavartin, O. Arcizet, A. Schliesser, and T. J. Kippenberg, "Optomechanically induced transparency." *Science*, vol. 330, no. 6010, pp. 1520–1523, Dec. 2010.

[102] C.-H. Dong, V. Fiore, M. C. Kuzyk, and H. Wang, "Transient optomechanically induced transparency in a silica microsphere," *Physical Review A*, vol. 87, no. 5, p. 055802, May 2013.

[103] A. H. Safavi-Naeini, T. P. M. Alegre, J. Chan, M. Eichenfield, M. Winger, Q. Lin, J. T. Hill, D. E. Chang, and O. Painter, "Electromagnetically induced transparency and slow light with optomechanics," *Nature*, vol. 472, no. 7341, pp. 69–73, Apr. 2011.

[104] Z. Yu and S. Fan, "Complete optical isolation created by indirect interband photonic transitions," *Nature Photon.*, vol. 3, no. 2, pp. 91–94, Feb. 2009.

[105] K. Han, J. H. Kim, and G. Bahl, "Radiation-driven optomechanical pressure sensor," in *Frontiers in Optics 2013 / Laser Science XXIX*, Oct. 2013.

[106] A. Savchenkov, A. Matsko, V. Ilchenko, D. Seidel, and L. Maleki, "Surface acoustic wave opto-mechanical oscillator and frequency comb generator," *Optics Letters*, vol. 36, no. 17, pp. 3338–3340, 2011.

[107] I. S. Grudinin, N. Yu, and L. Maleki, "Generation of optical frequency combs with a CaF2 resonator," *Opt. Lett.*, vol. 34, no. 7, pp. 878–880, Apr. 2009.

[108] T. J. Kippenberg, R. Holzwarth, and S. A. Diddams, "Microresonator-Based Optical Frequency Combs," *Science*, vol. 332, no. 6029, p. 555, Apr. 2011.

[109] P. Del'Haye, A. Schliesser, O. Arcizet, T. Wilken, R. Holzwarth, and T. J. Kippenberg, "Optical frequency comb generation from a monolithic microresonator," *Nature*, vol. 450, p. 1214, Dec. 2007.

[110] Y. Liu, H. Miao, V. Aksyuk, and K. Srinivasan, "Wide cantilever stiffness range cavity optomechanical sensors for atomic force microscopy," *Opt. Express*, vol. 20, no. 16, pp. 18 268–18 280, July 2012.

[111] K. Srinivasan, H. Miao, M. T. Rakher, M. Davanco, and V. Aksyuk, "Optomechanical Transduction of an Integrated Silicon Cantilever Probe Using a Microdisk Resonator," *Nano Lett.*, vol. 11, no. 2, pp. 791–797, Feb. 2011.

[112] S. Harlepp, J. Robert, N. C. Darnton, and D. Chatenay, "Subnanometric measurements of evanescent wave penetration depth using total internal reflection microscopy combined with fluorescent correlation spectroscopy," *Applied Physics Letters*, vol. 85, no. 17, pp. 3917–3919, 2004.

[113] S. L. Chuang, *Physics of Photonic Devices*, 2nd ed. Wiley, 2009.

[114] J. Knight, G. Cheung, F. Jacques, and T. Birks, "Phase-matched excitation of whispering-gallery-mode resonances by a fiber taper," *Optics Letters*, vol. 22, no. 15, pp. 1129–1131, 1997.

[115] H. Onodera, I. Awai, and J. ichi Ikenoue, "Refractive-index measurement of bulk materials: prism coupling method," *Appl. Opt.*, vol. 22, no. 8, pp. 1194–1197, Apr 1983.

[116] H. Li, Z. Cao, H. Lu, and Q. Shen, "Free-space coupling of a light beam into a symmetrical metal-cladding optical waveguide," *Applied Physics Letters*, vol. 83, no. 14, pp. 2757–2759, 2003.

[117] T. A. Birks and Y. W. Li, "The shape of fiber tapers," *J. Lightwave Technol.*, vol. 10, no. 4, pp. 432–438, Apr 1992.

[118] S. W. Harun, K. S. Lim, C. K. Tio, K. Dimyati, and H. Ahmad, "Theoretical analysis and fabrication of tapered fiber," *Optik - International Journal for Light and Electron Optics*, vol. 124, no. 6, pp. 538–543, Mar. 2013.

[119] J. E. Hoffman, S. Ravets, J. A. Grover, P. Solano, P. R. Kordell, J. D. Wong-Campos, L. A. Orozco, and S. L. Rolston, "Ultrahigh transmission optical nanofibers," *AIP Advances*, vol. 4, no. 6, p. 067124, Oct. 2018.

[120] J. Petersen, J. Volz, and A. Rauschenbeutel, "Chiral nanophotonic waveguide interface based on spin-orbit interaction of light," *Science*, vol. 346, no. 6205, p. 67, Oct. 2014.

[121] C.-L. Zou, F.-J. Shu, F.-W. Sun, Z.-J. Gong, Z.-F. Han, and G.-C. Guo, "Theory of free space coupling to high-Q whispering gallery modes," *Opt. Express*, vol. 21, no. 8, pp. 9982–9995, Apr. 2013.

[122] R. Dahan, L. L. Martin, and T. Carmon, "Droplet optomechanics," *Optica*, vol. 3, no. 2, pp. 175–178, Feb. 2016.

[123] L. Labrador-Páez, K. Soler-Carracedo, M. Hernández-Rodríguez, I. R. Martín, T. Carmon, and L. L. Martin, "Liquid whispering-gallery-mode resonator as a humidity sensor," *Opt. Express*, vol. 25, no. 2, pp. 1165–1172, Jan. 2017.

[124] B. E. Deal and A. S. Grove, "General Relationship for the Thermal Oxidation of Silicon," *Journal of Applied Physics*, vol. 36, no. 12, pp. 3770–3778, 1965.

[125] A. Gondarenko, J. S. Levy, and M. Lipson, "High confinement micron-scale silicon nitride high Q ring resonator," *Opt. Express*, vol. 17, no. 14, pp. 11 366–11 370, July 2009.

[126] E. S. Hosseini, S. Yegnanarayanan, A. H. Atabaki, M. Soltani, and A. Adibi, "High Quality Planar Silicon Nitride Microdisk Resonators for Integrated Photonics in the Visible Wavelength Range," *Opt. Express*, vol. 17, no. 17, pp. 14 543–14 551, Aug. 2009.

[127] J. S. Levy, M. A. Foster, A. L. Gaeta, and M. Lipson, "Harmonic generation in silicon nitride ring resonators," *Opt. Express*, vol. 19, no. 12, pp. 11 415–11 421, June 2011.

[128] B. Thubthimthong, T. Sasaki, and K. Hane, "Asymmetrically and Vertically Coupled Hybrid Si/GaN Microring Resonators for On-Chip Optical Interconnects," *IEEE Photonics Journal*, vol. 7, no. 4, pp. 1–11, Aug 2015.

[129] T.-J. Wang, C.-H. Chu, and C.-Y. Lin, "Electro-optically tunable microring resonators on lithium niobate," *Opt. Lett.*, vol. 32, no. 19, pp. 2777–2779, Oct. 2007.

[130] A. Guarino, G. Poberaj, D. Rezzonico, R. Degl'Innocenti, and P. Günter, "Electro-optically tunable microring resonators in lithium niobate," *Nature Photonics*, vol. 1, p. 407, July 2007.

[131] Q. Xu and M. Lipson, "All-optical logic based on silicon micro-ring resonators," *Opt. Express*, vol. 15, no. 3, pp. 924–929, Feb. 2007.

[132] Q. Xu, D. Fattal, and R. G. Beausoleil, "Silicon microring resonators with 1.5-um radius," *Opt. Express*, vol. 16, no. 6, pp. 4309–4315, Mar. 2008.

[133] R. Kant, N. Ferralis, J. Provine, R. Maboudian, and R. T. Howe, "Experimental Investigation of Silicon Surface Migration in Low Pressure Nonreducing Gas Environments," *Electrochemical and Solid-State Letters*, vol. 12, no. 12, pp. H437–H440, 2009.

[134] T. Nagourney, J. Y. Cho, A. Darvishian, B. Shiari, and K. Najafi, "Effect of metal annealing on the Q-factor of metal- coated fused silica micro shell resonators," in *2015 IEEE International Symposium on Inertial Sensors and Systems (ISISS) Proceedings*, March 2015, pp. 1–5.

[135] C. Y. J. Ying, C. L. Sones, A. C. Peacock, F. Johann, E. Soergel, R. W. Eason, M. N. Zervas, and S. Mailis, "Ultra-smooth lithium niobate photonic micro-structures by surface tension reshaping," *Opt. Express*, vol. 18, no. 11, pp. 11 508–11 513, May 2010.

[136] K. Williams and R. Muller, "Etch rates for micromachining processing," *Journal of Microelectromechanical Systems*, vol. 5, no. 4, pp. 256–269, Dec 1996.

[137] D. Armani, T. Kippenberg, S. Spillane, and K. Vahala, "Ultra-high-Q toroid microcavity on a chip," *Nature*, vol. 421, no. 6926, pp. 925–928, Feb 2003, 10.1038/nature01371.

[138] X. Zhang and A. M. Armani, "Silica microtoroid resonator sensor with monolithically integrated waveguides," *Opt. Express*, vol. 21, no. 20, pp. 23 592–23 603, Oct. 2013.

[139] I. S. Grudinin and L. Maleki, "Ultralow-threshold Raman lasing with CaF2 resonators," *Opt. Lett.*, vol. 32, no. 2, pp. 166–168, Jan. 2007.

[140] S. Maayani, L. L. Martin, S. Kaminski, and T. Carmon, "Cavity optocapillaries," *Optica*, vol. 3, no. 5, pp. 552–555, May 2016.

[141] I. S. Grudinin, A. B. Matsko, and L. Maleki, "Brillouin Lasing with a CaF_2 Whispering Gallery Mode Resonator," *Phys. Rev. Lett.*, vol. 102, no. 4, p. 043902, Jan. 2009.

[142] A. Giorgini, S. Avino, P. Malara, P. De Natale, M. Yannai, T. Carmon, and G. Gagliardi, "Stimulated Brillouin Cavity Optomechanics in Liquid Droplets," *Phys. Rev. Lett.*, vol. 120, p. 073902, Feb 2018.

[143] F.-Q. Zhao and H. Hiroyasu, "The applications of laser Rayleigh scattering to combustion diagnostics," *Progress in Energy and Combustion Science*, vol. 19, no. 6, pp. 447–485, Jan. 1993.

[144] D. C. Fourguette, R. M. Zurni, and M. B. Long, "Two-Dimensional Rayleigh Thermometry in a Turbulent Nonpremixed Methane-Hydrogen Flame," *Combustion Science and Technology*, vol. 44, no. 5-6, pp. 307–317, Jan. 1986.

[145] R. J. Adrian, "Scattering particle characteristics and their effect on pulsed laser measurements of fluid flow: speckle velocimetry vs particle image velocimetry," *Appl. Opt.*, vol. 23, no. 11, pp. 1690–1691, June 1984.

[146] C. V. Raman, "A new radiation," *Indian Journal of Physics*, vol. 2, pp. 387–398, 1928.

[147] Y. R. Shen and N. Bloembergen, "Theory of Stimulated Brillouin and Raman Scattering," *Phys. Rev.*, vol. 137, no. 6A, pp. A1787–A1805, Mar 1965.

[148] C. V. Raman, "A new radiation [Reproduced from Indian J. Phys., 1928, 2, 387-398]," *Current Science*, vol. 74, no. 4, pp. 382–386, 1998.

[149] D. H. Andrews, "The Relation Between the Raman Spectra and the Structure of Organic Molecules," *Phys. Rev.*, vol. 36, pp. 544–554, Aug 1930.

[150] S. Coen, A. H. L. Chau, R. Leonhardt, J. D. Harvey, J. C. Knight, W. J. Wadsworth, and P. S. J. Russell, "Supercontinuum generation by stimulated Raman scattering and parametric four-wave mixing in photonic crystal fibers," *J. Opt. Soc. Am. B*, vol. 19, no. 4, pp. 753–764, Apr. 2002.

[151] R. Y. Chiao, C. H. Townes, and B. P. Stoicheff, "Stimulated Brillouin Scattering and Coherent Generation of Intense Hypersonic Waves," *Phys. Rev. Lett.*, vol. 12, no. 21, pp. 592–595, May 1964.

[152] L. Brillouin, "Diffusion de la lumière et des rayons X par un corps transparent homogène - Influence de l'agitation thermique," *Ann. Phys.*, vol. 9, no. 17, pp. 88–122, 1922.

[153] L. I. Mandelstam, "Light Scattering by Inhomogeneous Media," *Zh. Russ. Fiz-Khim. Ova*, vol. 58, no. 381, 1926.

[154] Y. Aoki, K. Tajima, and I. Mito, "Input power limits of single-mode optical fibers due to stimulated Brillouin scattering in optical communication systems," *Journal of Lightwave Technology*, vol. 6, no. 5, pp. 710–719, 1988.

[155] E. P. Ippen and R. H. Stolen, "Stimulated Brillouin scattering in optical fibers," *Appl. Phys. Lett.*, vol. 21, no. 11, pp. 539–541, Jan. 2019.

[156] R. G. Smith, "Optical Power Handling Capacity of Low Loss Optical Fibers as Determined by Stimulated Raman and Brillouin Scattering," *Appl. Opt.*, vol. 11, no. 11, pp. 2489–2494, Nov. 1972.

[157] X. Bao, D. J. Webb, and D. A. Jackson, "32-km distributed temperature sensor based on Brillouin loss in an optical fiber," *Opt. Lett.*, vol. 18, no. 18, pp. 1561–1563, Sep. 1993.

[158] M. DeMerchant, A. Brown, X. Bao, and T. Bremner, "Structural monitoring by use of a Brillouin distributed sensor," *Appl. Opt.*, vol. 38, no. 13, pp. 2755–2759, May 1999.

[159] D. Inaudi and B. Glisic, "Long-Range Pipeline Monitoring by Distributed Fiber Optic Sensing," *Journal of Pressure Vessel Technology*, vol. 132, no. 1, pp. 011 701–011 701–9, Dec. 2009.

[160] G. Bahl, K. H. Kim, W. Lee, J. Liu, X. Fan, and T. Carmon, "Brillouin cavity optomechanics with microfluidic devices," *Nature Communications*, vol. 4, p. 2994, June 2013.

[161] T. Tanemura, Y. Takushima, and K. Kikuchi, "Narrowband optical filter, with a variable transmission spectrum, using stimulated Brillouin scattering in optical fiber," *Opt. Lett.*, vol. 27, no. 17, pp. 1552–1554, Sep. 2002.

[162] B. Vidal, M. A. Piqueras, and J. Martí, "Tunable and reconfigurable photonic microwave filter based on stimulated Brillouin scattering," *Opt. Lett.*, vol. 32, no. 1, pp. 23–25, Jan. 2007.

[163] W. Zhang and R. A. Minasian, "Widely Tunable Single-Passband Microwave Photonic Filter Based on Stimulated Brillouin Scattering," *IEEE Photonics Technology Letters*, vol. 23, no. 23, pp. 1775–1777, 2011.

[164] D. Marpaung, B. Morrison, M. Pagani, R. Pant, D.-Y. Choi, B. Luther-Davies, S. J. Madden, and B. J. Eggleton, "Low-power, chip-based stimulated Brillouin scattering microwave photonic filter with ultrahigh selectivity," *Optica*, vol. 2, no. 2, pp. 76–83, Feb. 2015.

[165] O. Terra, G. Grosche, and H. Schnatz, "Brillouin amplification in phase coherent transfer of optical frequencies over 480 km fiber," *Opt. Express*, vol. 18, no. 15, pp. 16 102–16 111, July 2010.

[166] A. Ghosh, D. Venkitesh, and R. Vijaya, "Study of Brillouin amplifier characteristics toward optimized conditions for slow light generation," *Appl. Opt.*, vol. 48, no. 31, pp. G48–G52, Nov. 2009.

[167] R. Pant, A. Byrnes, C. G. Poulton, E. Li, D.-Y. Choi, S. Madden, B. Luther-Davies, and B. J. Eggleton, "Photonic-chip-based tunable slow and fast light via stimulated Brillouin scattering," *Opt. Lett.*, vol. 37, no. 5, pp. 969–971, Mar 2012.

[168] I. S. Grudinin, A. B. Matsko, and L. Maleki, "Brillouin Lasing with a CaF_2 Whispering Gallery Mode Resonator," *Phys. Rev. Lett.*, vol. 102, p. 043902, Jan 2009.

[169] I. V. Kabakova, R. Pant, D.-Y. Choi, S. Debbarma, B. Luther-Davies, S. J. Madden, and B. J. Eggleton, "Narrow linewidth Brillouin laser based on chalcogenide photonic chip," *Opt. Lett.*, vol. 38, no. 17, pp. 3208–3211, Sep. 2013.

[170] N. T. Otterstrom, R. O. Behunin, E. A. Kittlaus, Z. Wang, and P. T. Rakich, "A silicon Brillouin laser," *Science*, vol. 360, no. 6393, pp. 1113–1116, 2018.

[171] R. W. Boyd, *Nonlinear Optics*, 3rd ed. Elsevier, 2008, Chapter 9.

[172] I. L. Fabelinskii, *Molecular Scattering of Light*. Plenum Press, 1968.

[173] N. Kitamura, K. Fukumi, J. Nishii, and N. Ohno, "Relationship between refractive index and density of synthetic silica glasses," *Journal of Applied Physics*, vol. 101, no. 12, p. 123533, 2007.

[174] X. Huang and S. Fan, "Complete All-Optical Silica Fiber Isolator via Stimulated Brillouin Scattering," *Lightwave Technology, Journal of*, vol. 29, no. 15, pp. 2267–2275, Aug 2011.

[175] C. G. Poulton, R. Pant, A. Byrnes, S. Fan, M. J. Steel, and B. J. Eggleton, "Design for broadband on-chip isolator using stimulated Brillouin scattering in dispersion-engineered chalcogenide waveguides," *Opt. Express*, vol. 20, no. 19, pp. 21 235–21 246, Sep 2012.

[176] B. J. Eggleton, C. G. Poulton, and R. Pant, "Inducing and harnessing stimulated Brillouin scattering in photonic integrated circuits," *Adv. Opt. Photon.*, vol. 5, no. 4, pp. 536–587, Dec. 2013.

[177] S. Y. Elnaggar and G. N. Milford, "Controlling Nonreciprocity Using Enhanced Brillouin Scattering," *IEEE Transactions on Antennas and Propagation*, vol. 66, no. 7, pp. 3500–3511, 2018.

[178] M. Hafezi and P. Rabl, "Optomechanically induced non-reciprocity in microring resonators," *Opt. Express*, vol. 20, no. 7, pp. 7672–7684, Mar. 2012.

[179] A. Imamoğlu and S. E. Harris, "Lasers without inversion: interference of dressed lifetime-broadened states," *Opt. Lett.*, vol. 14, no. 24, pp. 1344–1346, Dec. 1989.

[180] S. E. Harris, J. E. Field, and A. Imamoğlu, "Nonlinear optical processes using electromagnetically induced transparency," *Phys. Rev. Lett.*, vol. 64, pp. 1107–1110, Mar 1990.

[181] A. Kasapi, M. Jain, G. Y. Yin, and S. E. Harris, "Electromagnetically Induced Transparency: Propagation Dynamics," *Phys. Rev. Lett.*, vol. 74, pp. 2447–2450, Mar 1995.

[182] M. D. Lukin and A. Imamoglu, "Controlling photons using electromagnetically induced transparency," *Nature*, vol. 413, no. 6853, pp. 273–276, Sep. 2001.

[183] P. Arve, P. Jänes, and L. Thylén, "Propagation of two-dimensional pulses in electromagnetically induced transparency media," *Phys. Rev. A*, vol. 69, p. 063809, Jun 2004.

[184] C. L. Garrido Alzar, M. A. G. Martinez, and P. Nussenzveig, "Classical analog of electromagnetically induced transparency," *American Journal of Physics*, vol. 70, no. 1, pp. 37–41, Jan. 2002.

[185] D. Smith, H. Chang, K. Fuller, A. Rosenberger, and R. Boyd, "Coupled-resonator-induced transparency," *Physical Review A*, vol. 69, no. 6, p. 063804, June 2004.

[186] S. Zhang, D. A. Genov, Y. Wang, M. Liu, and X. Zhang, "Plasmon-Induced Transparency in Metamaterials," *Phys. Rev. Lett.*, vol. 101, p. 047401, Jul 2008.

[187] N. Liu, L. Langguth, T. Weiss, J. Kästel, M. Fleischhauer, T. Pfau, and H. Giessen, "Plasmonic analogue of electromagneticallyinduced transparency at the Drude damping limit," *Nature Materials*, vol. 8, no. 9, pp. 758–762, July 2009.

[188] J. J. Longdell, E. Fraval, M. J. Sellars, and N. B. Manson, "Stopped Light with Storage Times Greater than One Second Using Electromagnetically Induced Transparency in a Solid," *Physical Review Letters*, vol. 95, no. 6, p. 063601, Aug. 2005.

[189] Y. Zhang, N. Wang, H. Tian, H. Wang, W. Qiu, J. Wang, and P. Yuan, "A high sensitivity optical gyroscope based on slow light in coupled-resonator-induced transparency," *Physics Letters A*, vol. 372, no. 36, pp. 5848–5852, Sep. 2008.

[190] F. B. M. dos Santos and J. W. R. Tabosa, "Application of electromagnetically induced transparency for cold-atom velocimetry," *Phys. Rev. A*, vol. 73, p. 023422, Feb 2006.

[191] H. Y. Ling, Y.-Q. Li, and M. Xiao, "Electromagnetically induced grating: Homogeneously broadened medium," *Phys. Rev. A*, vol. 57, pp. 1338–1344, Feb 1998.

[192] H. Schmidt and A. Imamoglu, "Giant Kerr nonlinearities obtained by electromagnetically induced transparency," *Opt. Lett.*, vol. 21, no. 23, pp. 1936–1938, Dec. 1996.

[193] M. Jain, H. Xia, G. Y. Yin, A. J. Merriam, and S. E. Harris, "Efficient Nonlinear Frequency Conversion with Maximal Atomic Coherence," *Phys. Rev. Lett.*, vol. 77, pp. 4326–4329, Nov 1996.

[194] Y. Liu, M. Davanço, V. Aksyuk, and K. Srinivasan, "Electromagnetically Induced Transparency and Wideband Wavelength Conversion in Silicon Nitride Microdisk Optomechanical Resonators," *Phys. Rev. Lett.*, vol. 110, p. 223603, May 2013.

[195] G. S. Agarwal and S. S. Jha, "Multimode phonon cooling via three-wave parametric interactions with optical fields," *Phys. Rev. A*, vol. 88, p. 013815, Jul 2013.

[196] A. Yariv, "Quantum theory for parametric interactions of light and hypersound," *Quantum Electronics, IEEE Journal of*, vol. 1, no. 1, pp. 28–36, 1965.

[197] G. Bahl, X. Fan, and T. Carmon, "Acoustic whispering-gallery modes in optomechanical shells," *New Journal of Physics*, vol. 14, p. 115026, November 2012.

[198] M. Tomes and T. Carmon, "Photonic Micro-Electromechanical Systems Vibrating at X-band (11-GHz) Rates," *Phys. Rev. Lett.*, vol. 102, no. 11, p. 113601, March 2009.

[199] R. W. Boyd and D. J. Gauthier, "Controlling the velocity of light pulses," *Science*, vol. 326, no. 5956, pp. 1074–1077, 2009.

[200] G. Bahl, J. Zehnpfennig, M. Tomes, and T. Carmon, "Stimulated optomechanical excitation of surface acoustic waves in a microdevice," *Nature Communications*, vol. 2, p. 403, July 2011.

[201] T. J. Kippenberg, H. Rokhsari, T. Carmon, A. Scherer, and K. J. Vahala, "Analysis of Radiation-Pressure Induced Mechanical Oscillation of an Optical Microcavity," *Phys. Rev. Lett.*, vol. 95, no. 3, p. 033901, Jul 2005.

[202] Y. Ding, L. Chen, and S. Shen, "Slow and fast light based on SBS with the spectrum tailoring," *Optik - International Journal for Light and Electron Optics*, vol. 125, no. 9, pp. 2181–2184, Jan. 2014.

[203] R. Zhang, S. R. Garner, and L. V. Hau, "Creation of Long-Term Coherent Optical Memory via Controlled Nonlinear Interactions in Bose-Einstein Condensates," *Phys. Rev. Lett.*, vol. 103, p. 233602, Dec 2009.

[204] U. Leonhardt and P. Piwnicki, "Ultrahigh sensitivity of slow-light gyroscope," *Phys. Rev. A*, vol. 62, p. 055801, Oct. 2000.

[205] C. Peng, Z. Li, and A. Xu, "Rotation sensing based on a slow-light resonating structure with high group dispersion," *Appl. Opt.*, vol. 46, no. 19, pp. 4125–4131, July 2007.

[206] Z. Shi, R. W. Boyd, R. M. Camacho, P. K. Vudyasetu, and J. C. Howell, "Slow-Light Fourier Transform Interferometer," *Phys. Rev. Lett.*, vol. 99, p. 240801, Dec. 2007.

[207] Z. Shi and R. W. Boyd, "Slow-light interferometry: practical limitations to spectroscopic performance," *J. Opt. Soc. Am. B*, vol. 25, no. 12, pp. C136–C143, Dec. 2008.

[208] R. W. Boyd, D. J. Gauthier, and A. L. Gaeta, "Applications of Slow Light in Telecommunications," *Opt. Photon. News*, vol. 17, no. 4, pp. 18–23, Apr. 2006.

[209] E. Parra and J. R. Lowell, "Toward Applications of Slow Light Technology," *Opt. Photon. News*, vol. 18, no. 11, pp. 40–45, Nov. 2007.

[210] W. Chen, K. M. Beck, R. Bucker, M. Gullans, M. D. Lukin, H. Tanji-Suzuki, and V. Vuletic, "All-Optical Switch and Transistor Gated by One Stored Photon," *Science*, vol. 341, no. 6147, pp. 768–770, 2013.

[211] R. W. Boyd and D. J. Gauthier, ""Slow" and "fast" light," *Progress in Optics*, vol. 43, pp. 497–530, 2002.

[212] A. V. Turukhin, V. S. Sudarshanam, M. S. Shahriar, J. A. Musser, B. S. Ham, and P. R. Hemmer, "Observation of Ultraslow and Stored Light Pulses in a Solid," *Phys. Rev. Lett.*, vol. 88, p. 023602, Dec 2001.

[213] M. Bigelow, N. Lepeshkin, and R. Boyd, "Observation of Ultraslow Light Propagation in a Ruby Crystal at Room Temperature," *Physical Review Letters*, vol. 90, no. 11, p. 113903, Mar. 2003.

[214] K. L. Tsakmakidis, A. D. Boardman, and O. Hess, "'Trapped rainbow' storage of light in metamaterials," *Nature*, vol. 450, no. 7168, pp. 397–401, Nov. 2007.

[215] R. D. L. Kronig, "On the Theory of Dispersion of X-rays," *J. Opt. Soc. Am.*, vol. 12, no. 6, pp. 547–556, Jun 1926.

[216] F. J. Tipler, "Singularities and causality violation," *Annals of Physics*, vol. 108, no. 1, pp. 1–36, Sep. 1977.

[217] E. L. Bolda, R. Y. Chiao, and J. C. Garrison, "Two theorems for the group velocity in dispersive media," *Phys. Rev. A*, vol. 48, pp. 3890–3894, Nov 1993.

[218] L. Brillouin, "Über die Fortpflanzung des Lichtes in dispergierenden Medien," *Ann. Phys.*, vol. 349, no. 10, pp. 203–240, 1914.

[219] A. Sommerfeld, "Über die Fortpflanzung des Lichtes in dispergierenden Medien," *Ann. Phys.*, vol. 349, no. 10, pp. 177–202, 1914.

[220] A. Icsevgi and W. E. Lamb, "Propagation of Light Pulses in a Laser Amplifier," *Phys. Rev.*, vol. 185, pp. 517–545, Sep 1969.

[221] P. W. Milonni, *Fast Light, Slow Light and Left-Handed Light*. CRC Press, 2004.

[222] K. Y. Song, M. G. Herráez, and L. Thévenaz, "Observation of pulse delaying and advancement in optical fibers using stimulated Brillouin scattering," *Opt. Express*, vol. 13, no. 1, pp. 82–88, 2005.

[223] Y. Okawachi, M. Bigelow, J. Sharping, Z. Zhu, A. Schweinsberg, D. Gauthier, R. Boyd, and A. Gaeta, "Tunable All-Optical Delays via Brillouin Slow Light in an Optical Fiber," *Physical Review Letters*, vol. 94, no. 15, p. 153902, Apr. 2005.

[224] L. Thévenaz, "Slow and fast light in optical fibres," *Nature Photonics*, vol. 2, no. 8, pp. 474–481, 2008.

[225] L. Yi, L. Zhan, W. Hu, and Y. Xia, "Delay of Broadband Signals Using Slow Light in Stimulated Brillouin Scattering With Phase-Modulated Pump," *IEEE Photonics Technology Letters*, vol. 19, no. 8, pp. 619–621, Apr. 2007.

[226] D. Deng, W. Gao, M. Liao, Z. Duan, T. Cheng, T. Suzuki, and Y. Ohishi, "Superluminal propagation in a highly nonlinear fiber embedded in a Brillouin laser ring cavity," *Proc. SPIE*, vol. 8982, p. 89821J, 2014.

[227] H. Ju, L. Ren, X. Lin, J. Liang, and C. Ma, "Wide-Range Continuously-Tunable Slow-Light Delay Line Based on Stimulated Brillouin Scattering," *IEEE Photonics Technology Letters*, vol. 25, no. 19, pp. 1920–1923, Oct. 2013.

[228] R. Wolfe, J. F. Dillon, R. A. Lieberman, and V. J. Fratello, "Broadband magneto-optic waveguide isolator," *Appl. Phys. Lett.*, vol. 57, no. 10, pp. 960–962, 1990.

[229] D. Jalas, A. Petrov, M. Eich, W. Freude, S. Fan, Z. Yu, R. Baets, M. Popovic, A. Melloni, J. D. Joannopoulos, M. Vanwolleghem, C. R. Doerr, and H. Renner, "What is and what is not an optical isolator," *Nature Photon.*, vol. 7, no. 8, pp. 579–582, Aug. 2013.

[230] M.-C. Tien, T. Mizumoto, P. Pintus, H. Kromer, and J. E. Bowers, "Silicon ring isolators with bonded nonreciprocal magneto-optic garnets," *Opt. Express*, vol. 19, no. 12, pp. 11 740–11 745, June 2011.

[231] K. Fang, Z. Yu, and S. Fan, "Photonic Aharonov-Bohm Effect Based on Dynamic Modulation," *Phys. Rev. Lett.*, vol. 108, no. 15, p. 153901, Apr. 2012.

[232] X. Zhu, L. Feng, P. Zhang, X. Yin, and X. Zhang, "One-way invisible cloak using parity-time symmetric transformation optics," *Opt. Lett.*, vol. 38, no. 15, pp. 2821–2824, 2013.

[233] D. L. Sounas, C. Caloz, and A. Alu, "Giant non-reciprocity at the subwavelength scale using angular momentum-biased metamaterials," *Nature Commun.*, vol. 4, Sep. 2013.

[234] L. Fan, J. Wang, L. T. Varghese, H. Shen, B. Niu, Y. Xuan, A. M. Weiner, and M. Qi, "An All-Silicon Passive Optical Diode," *Science*, vol. 335, no. 6067, pp. 447–450, Jan. 2012.

[235] R. Van Laer, B. Kuyken, D. Van Thourhout, and R. Baets, "Interaction between light and highly confined hypersound in a silicon photonic nanowire," *Nature Photon.*, vol. 9, pp. 199–203, Mar. 2015.

[236] E. A. Kittlaus, H. Shin, and P. T. Rakich, "Large Brillouin amplification in silicon," *Nature Photon.*, vol. 10, pp. 463–468, June 2016.

[237] Y. Shoji, M. Ito, Y. Shirato, and T. Mizumoto, "MZI optical isolator with Si-wire waveguides by surface-activated direct bonding," *Opt. Express*, vol. 20, no. 16, pp. 18 440–18 448, July 2012.

[238] S. Groblacher, K. Hammerer, M. R. Vanner, and M. Aspelmeyer, "Observation of strong coupling between a micromechanical resonator and an optical cavity field," *Nature*, vol. 460, no. 7256, pp. 724–727, Aug. 2009.

[239] B. Peng, Ş. K. Özdemir, W. Chen, F. Nori, and L. Yang, "What is and what is not electromagnetically induced transparency in whispering-gallery microcavities," *Nature Commun.*, vol. 5, Oct. 2014.

[240] J. M. Ward, A. Maimaiti, V. H. Le, and S. N. Chormaic, "Contributed Review: Optical micro- and nanofiber pulling rig," *Rev. Sci. Instrum.*, vol. 85, no. 11, 2014.

[241] S. Kato and T. Aoki, "Strong Coupling between a Trapped Single Atom and an All-Fiber Cavity," *Phys. Rev. Lett.*, vol. 115, p. 093603, Aug 2015.

[242] M. Cai, O. Painter, and K. J. Vahala, "Observation of Critical Coupling in a Fiber Taper to a Silica-Microsphere Whispering-Gallery Mode System," *Phys. Rev. Lett.*, vol. 85, pp. 74–77, Jul 2000.

[243] S. Kim and G. Bahl, "Role of optical density of states in Brillouin optomechanical cooling," *Opt. Express*, vol. 25, no. 2, pp. 776–784, Jan. 2017.

[244] C.-H. Dong, V. Fiore, M. C. Kuzyk, and H. Wang, "Optomechanical dark mode." *Science*, vol. 338, no. 6114, pp. 1609–1613, Dec. 2012.

[245] G. S. Wiederhecker, L. Chen, A. Gondarenko, and M. Lipson, "Controlling photonic structures using optical forces," *Nature*, vol. 462, no. 7273, pp. 633–636, Dec. 2009.

[246] H. A. Stone, A. D. Stroock, and A. Ajdari, "Engineering Flows in Small Devices: Microfluidics Toward a Lab-on-a-Chip," *Annu. Rev. Fluid Mech.*, vol. 36, no. 1, pp. 381–411, 2004.

[247] R. Daw and J. Finkelstein, "Lab on a chip," *Nature*, vol. 442, no. 7101, pp. 367–367, July 2006.

[248] D. Mark, S. Haeberle, G. Roth, F. Von Stetten, and R. Zengerle, *Microfluidic Lab-on-a-Chip Platforms: Requirements, Characteristics and Applications*, S. Kakaç, B. Kosoy, D. Li, and A. Pramuanjaroenkij, Eds. Springer, 2010.

[249] S. Knappe, P. D. D. Schwindt, V. Shah, L. Hollberg, J. Kitching, L. Liew, and J. Moreland, "A chip-scale atomic clock based on ^{87}Rb with improved frequency stability," *Opt. Express*, vol. 13, no. 4, pp. 1249–1253, Feb. 2005.

[250] A. Brannon, M. Jankovic, J. Breitbarth, Z. Popovic, V. Gerginov, V. Shah, S. Knappe, L. Hollberg, and J. Kitching, "A Local Oscillator for Chip-Scale Atomic Clocks at NIST," in *2006 IEEE International Frequency Control Symposium and Exposition*, 2006, pp. 443–447.

[251] J. Kitching, E. A. Donley, S. Knappe, M. Hummon, A. T. Dellis, J. Sherman, K. Srinivasan, V. A. Aksyuk, Q. Li, D. Westly, B. Roxworthy, and A. Lal, "NIST on a Chip: Realizing SI units with microfabricated alkali vapour cells," *Journal of Physics: Conference Series*, vol. 723, p. 012056, June 2016.

[252] S. D. Smith, I. Janossy, H. A. MacKenzie, J. G. Mathew, J. J. Reid, M. R. Taghizadeh, F. A. Tooley, and A. C. Walker, "Nonlinear Optical Circuit Elements As Logic Gates For Optical Computers: The First Digital Optical Circuits," *Optical Engineering*, vol. 24, no. 4, pp. 569–574, 1985.

[253] S. J. McNab, N. Moll, and Y. A. Vlasov, "Ultra-low loss photonic integrated circuit with membrane-type photonic crystal waveguides," *Opt. Express*, vol. 11, no. 22, pp. 2927–2939, Nov. 2003.

[254] K. J. Barker, A. Benner, R. Hoare, A. Hoisie, A. K. Jones, D. K. Kerbyson, D. Li, R. Melhem, R. Rajamony, E. Schenfeld, S. Shao, C. Stunkel, and P. Walker, "On the Feasibility of Optical Circuit Switching for High Performance Computing Systems," in *SC '05: Proceedings of the 2005 ACM/IEEE Conference on Supercomputing*, 2005, p. 16.

[255] H. R. Philipp, "Optical Properties of Silicon Nitride," *Journal of The Electrochemical Society*, vol. 120, no. 2, pp. 295–300, 1973.

[256] W. Qiu, P. T. Rakich, H. Shin, H. Dong, M. Soljačić, and Z. Wang, "Stimulated Brillouin scattering in nanoscale silicon step-index waveguides: a general framework of selection rules and calculating SBS gain," *Opt. Express*, vol. 21, no. 25, pp. 31 402–31 419, Dec. 2013.

[257] R. Pant, C. G. Poulton, D.-Y. Choi, H. Mcfarlane, S. Hile, E. Li, L. Thévenaz, B. Luther-Davies, S. J. Madden, and B. J. Eggleton, "On-chip stimulated Brillouin scattering," *Optics Express*, vol. 19, no. 9, pp. 8285–8290, 2011.

[258] A. Turik, A. Yesis, and L. Reznitchenko, "Negative longitudinal electrostriction in polycrystalline ferroelectrics: a nonlinear approach," *Journal of Physics: Condensed Matter*, vol. 18, no. 20, p. 4839, 2006.

[259] K. H. Nygaard, C. Grinde, and T. A. Fjeldly, "Stacked Coupled-Disk MEMS RResonator for RF Applications," in *Technical Proceedings of the 2008 NSTI Nanotechnology Conference and Trade Show*, vol. 3, 2008, pp. 478–480.

[260] S. Tallur and S. A. Bhave, "Simultaneous radiation pressure induced heating and cooling of an opto-mechanical resonator," *Applied Physics Letters*, vol. 100, no. 11, 2012.

[261] V. T. K. Sauer, Z. Diao, M. R. Freeman, and W. K. Hiebert, "Optical racetrack resonator transduction of nanomechanical cantilevers," *Nanotechnology*, vol. 25, no. 5, p. 055202, 2014.

[262] J.-M. Le Floch, M. Tobar, D. Cros, and J. Krupka, "High q-factor distributed bragg reflector resonators with reflectors of arbitrary thickness," *Ultrasonics, Ferroelectrics and Frequency Control, IEEE Transactions on*, vol. 54, no. 12, pp. 2689–2695, Dec. 2007.

[263] H. Altug and J. Vuckovic, "Two-dimensional coupled photonic crystal resonator arrays," in *Conference on Lasers and Electro-Optics/International Quantum Electronics Conference and Photonic Applications Systems Technologies*. Optical Society of America, 2004. p. IThI2.

[264] R. Kant, N. Ferralis, J. Provine, R. Maboudian, and R. T. Howe, "Experimental Investigation of Silicon Surface Migration in Low Pressure Nonreducing Gas Environments," *Electrochemical and Solid-State Letters*, vol. 12, no. 12, pp. H437–H440, 2009.

[265] S. Azimi, Z. Y. Dang, and M. B. H. Breese, "Oxidation smoothening of silicon machined micro- and nano-scale structures," *Microelectronic Engineering*, vol. 121, pp. 156–161, June 2014.

[266] H. Shin, W. Qiu, R. Jarecki, J. A. Cox, R. H. Olsson, III, A. Starbuck, Z. Wang, and P. T. Rakich, "Tailorable stimulated Brillouin scattering in nanoscale silicon waveguides," *Nature Communications*, vol. 4, 2013.

[267] D. B. Sohn, J. Kim, and G. Bahl, "Ultrahigh-Q silica-ALN hybrid disk optomechanical modulator," in *2017 IEEE 30th International Conference on Micro Electro Mechanical Systems (MEMS)*, 2017, pp. 301–303.

[268] K. Y. Yang, D. Y. Oh, S. H. Lee, Q.-F. Yang, X. Yi, B. Shen, H. Wang, and K. Vahala, "Bridging ultrahigh-Q devices and photonic circuits," *Nature Photonics*, vol. 12, no. 5, pp. 297–302, May 2018.

[269] K. Vahala, K. . Yang, D. . Oh, S. . Lee, Q. . Yang, X. Yi, B. Shen, and H. Wang, "Silicon-Chip-Based Brillouin Lasers and Soliton Microcombs using an Integrated Ultra-High-Q Silica Resonator," in *2019 Optical Fiber Communications Conference and Exhibition (OFC)*, Mar. 2019, pp. 1–2.

[270] S. Gundavarapu, G. M. Brodnik, M. Puckett, T. Huffman, D. Bose, R. Behunin, J. Wu, T. Qiu, C. Pinho, N. Chauhan, J. Nohava, P. T. Rakich, K. D. Nelson, M. Salit, and D. J. Blumenthal, "Sub-hertz fundamental linewidth photonic integrated Brillouin laser," *Nature Photonics*, vol. 13, no. 1, pp. 60–67, Jan. 2019.

[271] M. G. Herráez, K. Y. Song, and L. Thévenaz, "Arbitrary-bandwidth Brillouin slow light in optical fibers," *Opt. Express*, vol. 14, no. 4, pp. 1395–1400, Feb 2006.

[272] C. Altman and K. Suchy, *Reciprocity, Spatial Mapping and Time Reversal in Electromagnetics*, 2nd ed. Springer, 2011.

[273] W. P. Bowen and G. J. Milburn, *Quantum Optomechanics*, 1st ed. CRC Press, 2015.